Florida International University

FIU Digital Commons

FIU Electronic Theses and Dissertations | University Graduate School

6-26-2020

Multifunctional Nanopipette for Single Nanoparticles and Proteins Analysis

Popular Pandey
FIU, ppand009@fiu.edu

Follow this and additional works at: https://digitalcommons.fiu.edu/etd

 Part of the Biological and Chemical Physics Commons, and the Condensed Matter Physics Commons

Recommended Citation

Pandey, Popular, "Multifunctional Nanopipette for Single Nanoparticles and Proteins Analysis" (2020). *FIU Electronic Theses and Dissertations*. 4496.
https://digitalcommons.fiu.edu/etd/4496

This work is brought to you for free and open access by the University Graduate School at FIU Digital Commons. It has been accepted for inclusion in FIU Electronic Theses and Dissertations by an authorized administrator of FIU Digital Commons. For more information, please contact dcc@fiu.edu.

FLORIDA INTERNATIONAL UNIVERSITY

Miami, Florida

MULTIFUNCTIONAL NANOPIPETTE FOR SINGLE NANOPARTICLES AND PROTEINS ANALYSIS

A dissertation submitted in partial fulfillment of

the requirements for the degree of

DOCTOR OF PHILOSOPHY

in

PHYSICS

by

Popular Pandey

2020

To: Dean Michael R. Heithaus
College of Arts, Sciences and Education

This dissertation, written by Popular Pandey, and entitled Multifunctional Nanopipette for Single Nanoparticles and Proteins Analysis, having been approved in respect to style and intellectual content, is referred to you for judgment.

We have read this dissertation and recommend that it be approved.

_____
Chunlei Wang

_____
Xuewen Wang

_____
Prem P Chapagain

_____
Jin He, Major Professor

Date of Defense: June 26, 2020

The dissertation of Popular Pandey is approved.

_____
Dean Michael R. Heithaus
College of Arts, Sciences and Education

_____
Andrés G. Gil
Vice President for Research and Economic Development
and Dean of the University Graduate School

Florida International University, 2020

© Copyright 2020 by Popular Pandey

All rights reserved.

DEDICATION

I dedicate this dissertation to my parents.

ACKNOWLEDGMENTS

The outcome of this dissertation required a lot of guidance, support, encouragement, and assistance from many people and I am extremely fortunate to have got this all along with the completion of my dissertation. Thus, I do not want to miss this opportunity to express my sincere gratitude to all who deserve it. First, I take this opportunity to express my profound gratitude and deep regard to my supervisor Prof. Jin He for his exemplary guidance, patience, mentoring and encouragement throughout my graduate studies. His mentoring has provided me essential training especially in instrumentation, critical thinking, problem-solving, scientific writing and reasoning, professional presentation, and all these trainings will carry me a long way in the journey of life on which I am about to embark. His mentorship motivated me throughout my graduate career and provided an excellent platform to build new skillsets. His valuable input, management, investment of time, scientific knowledge and ideas and funding sources have made my graduate study very fruitful and enjoyable for which I am highly indebted to him.

I would like to express my sincere gratitude to Prof. Xuewen Wang who was always ready to answer my questions despite his busy schedule as my mentor. His valuable suggestions in our weekly group meetings have helped me a lot in the theoretical understanding of my research. His expertise in the theoretical condensed matter physics and analysis of experimental results and expert suggestions have helped me a lot to move forward in my research. Besides, I am very much grateful to my committee members, Prof. Prem Chapagain and Prof. Chunlei Wang, for their valuable suggestions and comments towards the successful completion of this dissertation. I am fortunate to have them not only

as committee members but also as collaborators during this dissertation research. I would also like to express my sincere thanks to Dr. Ajeet Kaushik, Dr Lidia Kos, Dr. Fenfei Leng and Dr. Jarka Miksovska for providing me an excellent environment for the collaboration projects. Their innovative idea, valuable suggestions, and expertise in biophysics have always helped me to design, troubleshoot the experiment and interpret the results.

I would like to express my sincere thanks and love to my sister Dr. Namuna Pandey for her continuous guidance and suggestions in research projects, numerical simulation, and providing training in instrumentation, data management, and analysis. Also, I would like to thank Dr. Shuai Chang and Dr. Qiang Fu for their help in the data analysis as well as teaching me LabVIEW. I would like to thank FIU AMERI staff, Patrick, Alex, and Yusuf for their training in nanofabrication and sample characterization. Besides, my special thanks go to past group members Dr. Jie Pan, Dr. Purushottam Tiwari and Dr. Gongming Qian, Dr. Feng Chen for providing valuable suggestions on my research projects.

It is impossible to list here the name of all friends who have given me help, encouragement, and advice during the time of work and thus I apologize. However, I wish to express my sincere thanks to my all colleagues including former and present lab members. I am obliged to my lab members Dr. Alberto Sassena Rubifiaro, Jing Guo, and Govinda Ghimire, Navin Jung Prajapati, Jonathan Tabares, and Jianghao Zhou, Mingzhu Huang and Qiushuang Ai for their kind support and assistance and helpful discussions in research and other normal lab activities. I greatly appreciate and would like to thank Javier Garcia for his help on experiments and data analysis during my dissertation years.

I would like to offer special thanks to mechanical engineer Zahid from the FIU machine shop and electrical engineer Norman from the FIU electronic shop. Both of them were kind and helpful should I have any problem with research instrumentation. I would also like to thank the whole physics department family along with all the professors and department staff (especially Liz, Omar, and Peggy) for their administrative help and support.

I would like to acknowledge the NSF (CMMI 1334417, CBET 1454544) and NSF Cooperative Agreement No. EEC-1647837 support for my Research Assistantship and FIU physics department for providing continuous support *via* Teaching Assistantship. I would like to thank FIU UGS and FIU CASE Dean's office for providing travel awards to attend several scientific conferences throughout my graduate studies. Importantly, I am very much thankful to FIU UGS for providing me the Dissertation Year Fellowship (DYF) Award which helped me a lot in completing my research projects and dissertation writing.

Last but not the least important, I would like to express my sincere and deepest appreciation for the marvelous support and the boundless love from my parents. I owe many thanks to my family members, relatives and friends for their constant encouragement and care. My special thanks go to my beloved wife for her love and support in every step of my life and providing valuable input in the research project as a collaborator. Without their support, it would be impossible for me to finish my journey of Ph.D. degree seamlessly.

ABSTRACT OF THE DISSERTATION

MULTIFUNCTIONAL NANOPIPETTE FOR SINGLE NANOPARTICLES AND PROTEINS ANALYSIS

by

POPULAR PANDEY

Florida International University, 2020

Miami, Florida

Professor Jin He, Major Professor

The structure, composition and dynamics of the nanoscale biomolecules determine their biological function. A slight alteration of which can lead to the malfunction of the protein: key to various diseases including cancer. The single-molecule measurement approach is therefore essential to characterize both the average properties and the rare and dynamic changes of these nanoscale entities. This dissertation focused on the development of a facile single-entity detection method by fabricating nanopore and nanoelectrode integrated multifunctional nanopipette for multi-mode electroanalytical detection of individual nanoparticles (NPs) and biomolecules.

First, polystyrene (PS) NPs was studied as it mimics the dielectric nature of the biomolecules. Hybrid dielectrophoretic (DEP) method was developed to efficiently preconcentrate the PS NPs to form large assemblies outside the nanopipette tip, for high-throughput single-NP detection and analysis. Second, a highly effective and facile electroanalytical method was developed to differentiate metallic NPs and dielectric NPs in

solution through their polarizability by implementing single-NP collision events at the nanoelectrode ('nanoimpact'). Third, the multifunctional nanopipette was used to probe magneto-electric NPs (MENPs) composed of a piezoelectric shell and a ferromagnetic core. For the first time, the nanopipette based electrochemical single-entity approach was used to probe AC B-field induced strain mediated surface potential enhancement on a MENP surface *via* "nanoimpact.' The results confirmed that the AC B-field stimulation caused localized surface potential enhancement of MENP but not of magnetic NPs which lacks the piezoelectric shell. Finally, we demonstrated a facile yet highly sensitive 'nanoimpact' based potentiometric method of detecting electrochemically inactive bio-macromolecules, by sensing open circuit potential (OCP) change when they approach towards and/or collides with and/or scatter away from the nanoelectrode of the nanopipette.

In summary, my dissertation presents the fabrication, development, and optimization of multifunctional nanopipette based electroanalytical biosensing platform. With both experimental and simulation results, my dissertation announces a facile, cost-effective, versatile, sensitive, easy integration with scanning probe technique, robust and label-free electroanalytical sensing method to study individual NPs including biomolecules *via* a charge sensing mechanism. The developed method has great potential to be used as a smart sensor for various biomedical applications, health monitoring, quality control, and environmental sensing.

TABLE OF CONTENTS

CHAPTER PAGES

LIST OF TABLES

TABLES PAGES

LIST OF FIGURES

FIGURES PAGES

CHAPTER 1: INTRODUCTION

1.1: Motivation and Background to Study the Single Entities

In recent years, the approach of biomolecular study is experiencing a transition from the traditional ensemble average methods to the single-entity studies.[1] Single cells, nucleic acid molecules, proteins, and synthetic and biological nanoparticles are collectively referred to as single entities. The most beautiful aspect of the single entity measurement is that it can probe energetically metastable, heterogeneous states one entity at a time, which is impossible *via* ensemble average methods. Single-entity approach to biomolecule investigation offers huge benefits, not only as biological research tools to examine heterogeneities among individual entities within the population but also as biosensing tools for medical diagnostics.

The study of the single entities involves the measurement of nanoscale entities that have dimensions ranging from 1-100 nm. It is the most important dimension range where complex biological processes occur. Additionally, the biological functions of the nanoscale biological entities are directly related to their structure, composition, and dynamics. A slight alteration of which can have a tremendous effect on their functions. Therefore, it is critically important to have a facile, cost-effective, and highly sensitive electroanalytical biosensing platform to precisely characterize the ensemble as well as rare dynamic events of these nanoscale entities. Commonly used existing single-molecule approaches include; optical methods (e.g., confocal microscopy,[2] flow cytometry,[3] fluorescence microscopy,[4, 5] Surface Plasmon Resonance imaging),[6] magnetic/optical tweezers,[7] Atomic Force Microscopy (AFM)[8], microfluidics[9] methods. Usually, these methods are highly intricate in terms of experimental design, require large sample volume, and

highly skilled professionals to work with and are expensive. The electrochemical method, on the other hand, that uses nanopore and an ultra-small nanoelectrode has drawn tremendous attention because of the sensitive label-free approach, cost-effective, facile fabrication and modification and miniature size.[10-14] However, limited information regarding a single entity can be achieved by using nanopores and nanoelectrodes alone. To enhance the sensitivity and selectivity of the nanopore devices and to add new functionality, in recent years, the multi-mode detection method has gained enormous popularity. The advantage of the multi-mode detection approach is that, it provides a variety of ways to control, manipulate and detect the single entities concurrently. By integrating two independent sensing approach in one make them complementary to each other which provide new insight in the single entity measurement with higher confidence and reliability.[15-19]

The primary goal of my dissertation work is to develop novel, highly sensitive and selective multi-mode electrochemical biosensing platform which can detect a single biomolecule. To achieve my goal, we integrate two highly emerging electrochemical detection platform, nanopore, and nanoelectrode, to one nanopipette apex. The integrated nanopipette is called multi-functional nanopipette. Previously reported electrochemical methods such as “nanoimpact” [20-22] which is simple and promising for insulating NPs detection, uses faradic current, however, it requires NPs to be redox-active and suitable for larger (>100 nm) NPs detection. In contrast, the nanopore-nanoelectrode nanopipette which relies on the particle’s charge for sensing does not require NPs to be fluorescent and redox-active. As compared to other multimode techniques, the nanopore-nanoelectrode

multimode detection is advantageous for these reasons: (a) It is a label-free detection approach, which allows us to analyze the single entities in their native environment. (b) The CNE-nanopore probe is mechanically robust and has sensitivity in the presence of a large number of contaminants for a long time. (c) Facile fabrication and modification and cost-effective. (d) Miniature size allows it to be integrated into the chip for the development of handheld smart biosensors.

To understand the multi-mode sensing capability of the nanopore-nanoelectrode nanopipette (single-entity detection platform), we first tested various model nanoparticles such as gold nanoparticles (GNPs), polystyrene nanoparticles (PS NPs), and magnetic nanoparticles (MNPs) and magnetoelectric nanoparticles (MENPs). We demonstrated that our detection method is sensitive to metallic and insulating nanoparticles. Besides, we showed for the first time that the single-entity approach can detect the surface charge enhancement of a single magnetoelectric nanoparticle under AC B-filed stimulation. The presence of the nanoelectrode near the nanopore provides us additional information about nanoparticle cluster formation and their dynamics in the aqueous solution and their motion behavior under various forces involved during the measurements. Furthermore, we also used a finite element numerical simulation as well as molecular dynamics simulations to understand the NP-CNE collision process. Finally, I detect and analyze the various biomolecules such as proteins, DNA, and virus-like NPs using multi-mode multifunctional nanopipette. The following sections in this chapter present an overview of the available single entity detection toolbox.

1.2: Toolbox for Single Entities Detection

There are several single-molecule detection methods available to date including optical methods (e.g., confocal microscopy, fluorescence microscopy, Surface Plasmon Resonance (SPR) imaging, magnetic/optical tweezers, Raman spectroscopy), scanning probe methods (e.g., atomic force microscopy, scanning ion conductance microscopy), microfluidics and electrochemical methods (e.g., nanopore, nanoelectrode). The following sections in this chapter present an overview of the single entity detection methods which are implemented to finish my dissertation project with more focus on the nanopipette electrical sensing platform and optical methods such as darkfield microscopy and confocal fluorescence microscopy.

1.2.1: Electrical Methods

1.2.1.1: Nanopores

Transportation of ions, DNA, RNA, peptide molecules, and various other biomolecules via nanoscale biological pore is a fundamental process in living beings which have inspired the development of nanopores for biosensing applications. A pore having nanoscale dimension (~1-100 nm in diameter) is defined as a nanopore. The nanopore-based single entity detection platform has gained remarkable attention as a result of the high sensitivity, versatility, label-free, amplification free electrical detection method which monitors the ionic flux blockade as a single entity traverse through it.[23-25] For example, protein molecules have typical dimensions of ~2-10 nm. When the cross-section of the protein and the nanopore are comparable, ionic flux blockade is larger because proteins block the majority of the ionic flow through the nanopore. In contrast, translocation of the same protein through larger nanopore resulting in small ionic flow blockade. Since the

revolutionary demonstration of nucleotide detection using α-Hemolysin nanopore[26], varieties of nanopores have been extensively used for biosensing,[14, 19, 27-29] energy conversion,[30-32] filtration,[33, 34] environmental monitoring[35] including genome sequencing.[36-39] Nanopore sensing is a label-free single-molecule recognition method which requires low sample volumes and can detect single entities even in the presence of contaminants. The nanopores used for sensing applications have synthetic (e.g., graphene nanopore) or biological (e.g., protein nanopore) or hybrid (synthetic and biological mixed) origin. The mechanism of nanopore-based sensing is presented in the following section.

1.2.1.1.1: Principle of Nanopore Detection

The schematic of nanopore detection using a conical glass nanopore is presented in Figure 1.1a. The nanopore sensing follows the working principle of the classical resistive-pulse method.[40] A nanopore sensor consists of a nanometer-sized hole in a biological/synthetic membrane that separates the two reservoirs filled with conducting buffer solutions. Both reservoirs have a separate reference electrode connected *via* an electrical circuit as shown in Figure 1.1a. Upon application of DC bias across the reference electrodes, a steady-state ion current is established as a result of ionic flow across the membrane *via* nanopore. Steady-state ion current serves as a baseline current signal for that specific bias. The magnitude of the ion current generated is in the pico-Ampere (pA) scale, which is measured ultra-sensitive electronics, housed inside a Faraday cage. Without single entities in the bath solution, the current signal is featureless. However, when charged single nano entities are present in the bath solution, they are electrophoretically driven through the nanometer-sized aperture as shown in Figure 1.1a. The entry and exit of these nano entities (e.g., NPs) *via* nanopore exhibit transient ionic current blockade signals as shown in Figure 1.1b. The

analysis of current amplitude (Δi), the dwell time duration of the entities in the pore (t_d) and the inter-event time duration (δt) of these transient current spikes provides information in single molecular level such as size, shape, charge, concentration and surface interactions between pore and analytes themselves as shown in Figure 1.1c.

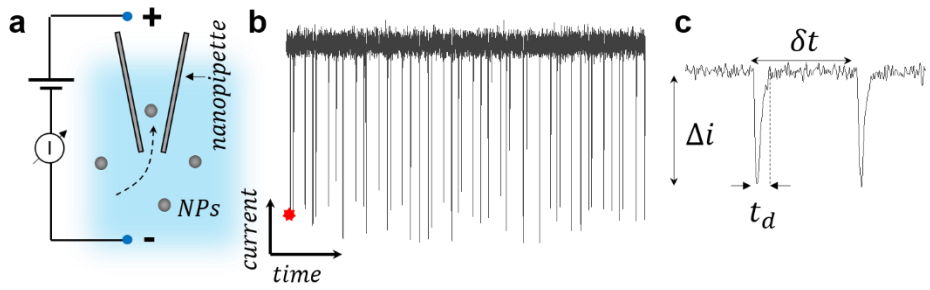

Figure 1. 1: (a) Schematic of the nanopore ionic current detection of single entities (not to scale) using glass nanopore. (b) The passage of a single nanoparticle (NP) results in a transient blockade in the ionic current through the nanopore which is observed in *i-t* time trace. (c) The zoom-in of *i-t* time trace shown in red during single NP passage via the nanopore. The Δi, t_d, and δt denote ionic current amplitude, blockade duration, and inter-event duration respectively.

1.2.1.1.2: Forces Controlling Single-entity Dynamics in Nanopore Experiments

The ion current produced during voltage-driven single entity entry and exit through the nanopore is the result of the interplay between diffusion, electrophoresis, and electroosmosis.[41] Diffusion is the result of the concentration gradient (∇C_j) of the charged entities. The charged species diffuse from high to low concentration regions creating a diffusive flux. The diffusive flux of charged species with diffusion constant (D_j) is given by Fick's law;

$$J_j = -D_j \nabla C_j \tag{1.1}$$

Electrophoresis is the migration of the charged entities (ions, particles, molecules, etc..) under an electric field (E). When positive nanopore bias (V_{pore}) is applied at the electrode

inside the nanopore, the negatively charged entities experience a force that drives them into the nanopore as shown in Figure 1.2. Under applied nanopore bias, the electrophoretic mobility μ_{EP} $(m^2V^{-1}s^{-1})$ of the charged entity (q) of radius r in an electrolyte of dynamic viscosity η is given as;

$$\mu_{EP} = \frac{q}{6\pi\eta r} \tag{1.2}$$

Small molecules and ions can be treated as point charges as they cannot support enough counterions to form a continuous double layer. However, we need to consider the double layer (DL) for larger (~ >30 nm) particles. The electrophoretic mobilities for small and large particles can be respectively approximated using Huckel-limit and Einstein-Smoluchowski limit and are defined by equations (1.3) and (1.4) below;

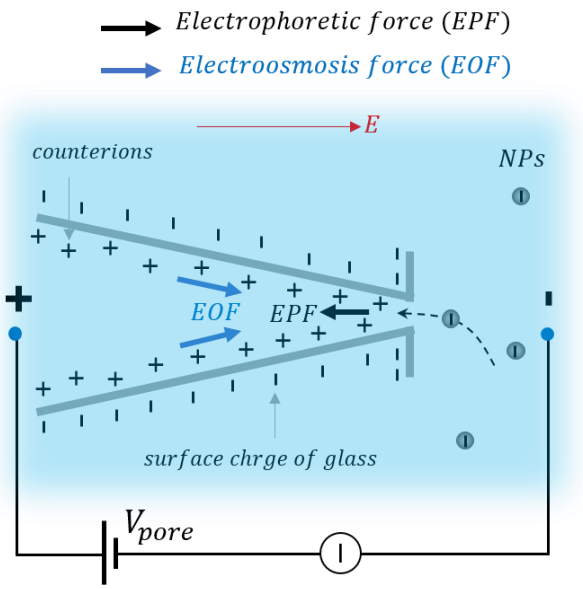

Figure 1. 2: (a) Major driving forces acting on the NPs in voltage-driven nanopore experiments. The applied positive nanopore bias V_{pore} creates an EPF that helps the negatively charged NPs to get inside of the nanopore. The movement of the mobile counterions generates the EOF opposite to the EPF. The red arrow denotes the electric field direction.

$$\mu_{EP} = \frac{2\varepsilon_r \varepsilon_0 \zeta}{3\eta} \tag{1.3}$$

$$\mu_{EP} = \frac{\varepsilon_r \varepsilon_0 \zeta}{\eta} \tag{1.4}$$

Typical values for the electrophoretic mobilities for small ions and molecules in water are $5 \times 10^{-8} m^2 V^{-1} s^{-1}$ and $0.1 - 1 \times 10^{-8} m^2 V^{-1} s^{-1}$ respectively. The electrophoretic flux of charged species is given as;

$$J_j = -\frac{z_j F}{RT} D_j C_j \nabla \boldsymbol{\phi} \tag{1.5}$$

Where J_j , D_j , C_j , $\boldsymbol{\phi}$, F, R, T and z_j are, respectively, the ionic flux, diffusion constant, concentration, local electric potential, Faraday's constant, gas constant, absolute temperature and charge of the species j.

Electroosmosis is the movement of electrolyte solution relative to the NPs under applied bias. The movement of fluid under applied bias is also called convective flow. Electroosmosis is prominent in nanoscale channels such as flow-through CNT, and nanopores.[42-44] For a micro/nanoscale channel, solving the Naiver-stokes equation and Poisson equation the ionic flux as a result of electroosmotic force is $C_j \boldsymbol{v}$. Where $\boldsymbol{v}$ is the fluid velocity and is given as;

$$v_{EO} = -\frac{\varepsilon E \zeta}{\eta} \tag{1.6}$$

Combining the electrophoretic and electroosmotic velocity we get effective velocity as;

$$v_{eff} = \frac{\varepsilon E(\zeta_p - \zeta_{pore})}{\eta} \tag{1.7}$$

The relative magnitude of the zeta potential of pore (ζ_{pore}) and particle (ζ_p) electroosmosis may enhance or suppress the electrophoresis.[41] In addition to these forces, Coulomb attractive /repulsive forces between charged entities itself and between negatively charged quartz nanopore surface and the charged entities also affect the NPs dynamics in the conical nanopore. Note that the quartz nanopore acquires a net negative charge in water as a consequence of the dissociation of the Silanol (Si-OH) group. Thus, the single entities experience attractive or repulsive Coulomb forces according to their charge states.

Contributions from diffusion, migration, and convection, the net flux of ionic species is given by

$$\boldsymbol{J_j}(x) = -D_j \nabla C_j - \frac{z_j F}{RT} D_j C_j \nabla \boldsymbol{\phi} + C_j \boldsymbol{v} \tag{1.8}$$

is called the Nernst-Plank equation. Where

$$\nabla^2 \emptyset = -\frac{F}{\varepsilon} \sum_j z_j C_j \tag{1.9}$$

is called the Poisson equation. The coupled Poisson-Nernst-Plank (PNP) equation describes the flux of charged species in the nanochannel.[45, 46] The ionic current caused by the ionic fluxes through nanochannel can be calculated by integration of the ionic flux density along the nanochannel cross-section area (S) using equation 1.10.

$$I = -\mathrm{F} \int [J(K+) - J(Cl-)].\boldsymbol{n}\, dS \tag{1.10}$$

1.2.1.1.3: Types of Nanopore

Nanopores are broadly divided into two types namely biological nanopores and solid-state/synthetic nanopores. A brief description of each type and their suitability for the applications follows below.

1.2.1.2.2.1: Biological Nanopore

Biological nanopores are ubiquitous and play a critical role in various biological functions and processes by facilitating the translocation of ions, peptides, proteins, DNA, RNA, and other macromolecules across the cell membrane or between cells. The beautiful aspect of the use of biological nanopores for sensing application is mainly as a result of atomic-precision structural reproducibility, pore size comparable to the biological entities of interest and the precise pore modification for various sensing purposes. Figure 1.3a shows a cartoon picture of an α-Hemolysin and MspA nanopore with their dimensions. Biological nanopore α-Hemolysin was first used to demonstrate the single-stranded RNA and DNA detection.[47] Since then a variety of biological nanopores have been developed and tested for various biosensing applications including proteins,[48, 49] small molecules,[50, 51] nucleotides[52-54] and metal ions[55] sensing, etc.. Recently, proteins pores such as MspA, ClyA, AeL, OmpG, aerolysin, FraC and, Nfp have been used for various sensing applications.[23, 24, 56] However, there are some limitations of biological nanopore sensing. The pore size of these pores cannot be altered, they are not robust and stable under variation of temperature, applied potential, mechanical pressure, pH, and concentration of electrolyte solution. Solid state nanopores are therefore introduced to overcome these limitations.

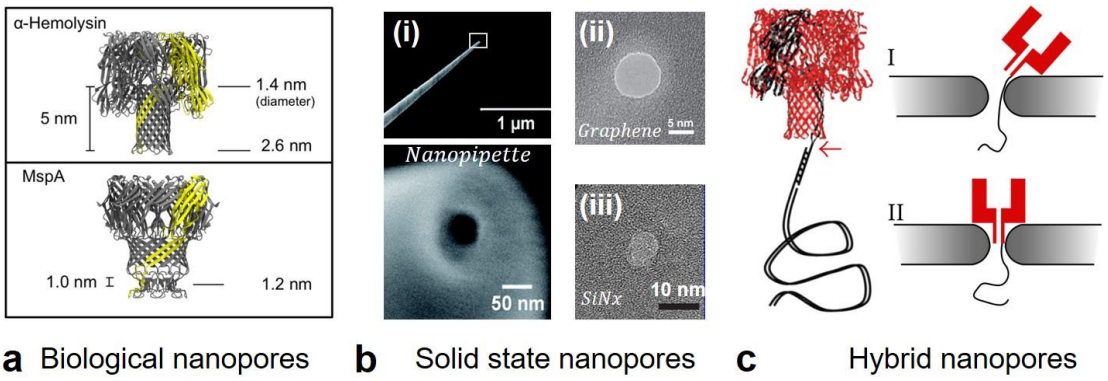

Figure 1. 3: Examples of nanopore-based biosensing platforms. (a) Biological nanopores: α-Hemolysin and MspA ([57], copyright 2015, nature publishing group). (b) Solid-state nanopores: (i) SEM image of a glass nanopipette with nanopore at the apex ([58], copyright 2014, royal society of chemistry). The apex is shown in zoom in below. (ii) TEM image of a graphene nanopore ([59], copyright 2013, nature publishing group). (iii) TEM image of a SiNx nanopore ([60], copyright 2018, nature publishing group). (c) Schematic of hybrid a nanopore ([61], copyright 2010, nature publishing group).

1.2.1.2.2.2: Solid State Nanopore

Mechanically robust, excellent thermal and chemical stability over varied pH, concentration, bias, and temperature, tunable nanopore shape, and size with sub-nanometer resolution, facile surface functionalization, integration compatibility with sophisticated electronics, and optical readout systems are the key advantages of the solid-state nanopores.[23, 24] Figure 1.3b shows examples of solid-state nanopores. These nanopores are fabricated using controlled dielectric breakdown, ion beam sculpting, electron-beam drilling, and by laser-assisted pulling of glass or quartz microcapillaries.[62] Two-dimensional (2D) solid-state nanopores such as graphene nanopores, boron nitride (BN), silicon nitride (SiN_x), molybdenum sulfide (MoS_2), and hafnium oxide (HfO_2) nanopores have been extensively used for numerous biosensing applications as for proteins, lipids, and nucleic acids.[23, 59, 62] The advantage of the glass/quartz nanopore over 2D nanopore and its implementation for biosensing is discussed in section 1.4. Solid-state

nanopores also have limitations such as variations of pore size, shape, and charge, unlike their biological counterpart which is atomically identical and highly reproducible. Besides, solid-state nanopores suffer from site-specific chemical modification which can be done with ease in the biological nanopores. To incorporate the merits from both types of nanopore platform, recently, great efforts have been made to develop hybrid nanopores for sensing applications.

1.2.1.2.2.3: Hybrid Nanopore

The hybrid nanopore utilizes both biological and solid-state nanopores. Hybrid nanopore platforms combine the advantages of site-specific chemical modification and atomically precise pore structure from protein nanopores and robustness and stability from solid-state nanopores. Figure 1.3c shows the insertion of α-Hemolysin pore into solid-state nanopore. The protein-conjugated α-Hemolysin nanopore is electrophoretically translocated through the solid-state nanopore to form hybrid nanopore.[61] Other types of hybrid nanopore platforms include CNTs embedded lipid bilayer/cell membrane for ssDNA sensing.[63] An alpha-hemolysin nanopore inserted glass micropipette tip based surface scanner has been also reported.[64] Furthermore, the Kyser group successfully used a SiN_x assisted DNA origami hybrid nanopore for dsDNA translocation.[65] Deoxyribonucleic acid (DNA) origami is a highly stable and versatile chemical building block. Using DNA origami for synthetic membrane porin constructions provides superior stability and versatility in nanopore structures and opens up numerous exciting opportunities in biosensing.

1.2.1.2: Micro/Nanoelectrodes

Micro/Nanoelectrode is another emerging electrochemical platform for single entity detection and analysis.[66-69] Microelectrodes/ultramicroelectrodes have dimensions of tens of micrometers/submicrometer range while electrodes with size below 100 nm are usually referred to as nanoelectrodes. Recently, nanoelectrodes have emerged as a promising electrochemical tool to study electrochemical processes at the nanoscale. Preference of micro/nanoelectrodes over traditional macro electrodes is that it has nanoscale geometry and can be used for noninvasive localized measurements in biological samples, efficient mass transport, thin double layers, the small potential drop across electrodes and low background capacitive signals.[70] As a result of these characteristics, micro/nanoelectrodes are extremely suitable for characterization of single nanoparticles/molecules,[71, 72] acquiring high resolved electrochemical imaging after integration with scanning probe methods,[73, 74] acquiring electrochemical measurements in highly resistive media such as water and localized and noninvasive local electrochemical measurements in biological samples.[75, 76]

To date, various nanoelectrodes geometries have been fabricated and implemented for various sensing applications. Planer, disk, sphere, hemisphere, circular, conical, etc. are the commonly reported nanoscale geometries. Usually, these nanoelectrodes are fabricated using nanofabrication methods, etc.hing metal wires such as Pt, Au, disposition od conductive layer (metal or carbon) on the porous materials, or inside of the nanopipette and laser-assisted wire pulling.[77] Nanoelelctrode geometry determines its mass transport properties and thus its electrochemical performance. Owing to the small geometry of the

nanoelectrode, radial diffusion becomes dominant. The general expression for diffusion-limited current (i_d) at the nanoelectrode is given by the Cotrell-equation;

$$i_d = mnFADC\left[\frac{1}{\sqrt{\pi Dt}} + \frac{1}{R_{NE}}\right] \dots\dots\dots\dots\dots\dots\dots\dots\dots\dots\dots\dots\dots\dots\dots\dots\dots\dots\dots\dots\dots\dots (1.11)$$

Which describes redox reactions occurring at the nanoelectrode interface. Where m, n, F, A, D, C, and R_{NE}, respectively denote the geometry factor ($m = 1$ for hemisphere and $m = \sqrt{2}$ for the sphere and value of m slightly changes for other geometry), the number of electrons transferred in the reaction, Faraday constant, area of the electrode geometry, diffusion constant of redox molecule, the concentration of redox molecule, and radius of the nanoelectrode. The first time-dependent term is caused by planer diffusion and the second term is the result of radial diffusion. Under the steady-state condition, only the second term contributes. The steady-state diffusion-limited current for disk, sphere, and hemisphere can be approximated respectively as;

$$i_d^{disk} = \pi mnFDCR;\ i_d^{sphere} = 4\pi mnFDCR\ and\ i_d^{hemisphere} = mnFDC\sqrt{2\pi A} \dots (1.12)$$

From the diffusion-limited current, the size of the nanoelectrode can be readily estimated. See Chapter 2 method section 2.1 for more detail. Owing to nanoscale geometry, nanoelectrodes have a thin double layer and extremely small double-layer capacitance (C) which makes the time constant ($\tau = RC; R = resistance$) of the nanoelectrodes very small making them ideal for measuring transient electrochemical reactions.[78]

1.2.1.3: Single Particle Collision Electrochemistry

In recent years, single particle collision electrochemistry or nanoimpact method has grown in popularity as one of the most attractive electrochemical sensing methods at the

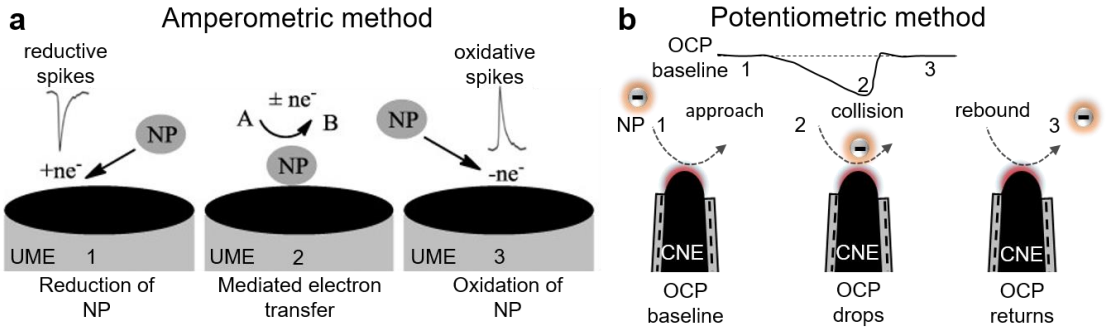

Figure 1. 4: (a) Schematic of amperometric single nanoparticle collision "nanoimpact" method ([79], copyright 2014, Elsevier publishing group). An ultramicroelectrode (UME) is used for electrochemical detection of NPs. During the reduction of NP at UME (scheme 1), reductive downward current spikes appear as UME gains extra electrons during nanoimpact. In scheme 2, nanoimpact event appears as a result of the mediated electron transfer at the UME. The nature of the current spikes may be upward or downward depending on the nature of the electrochemical process. Upward current spikes, as a result of loss of electrons at UME, appears in scheme 3. (b) A schematic of potentiometric nanoimpact method using hemispherical carbon nanoelectrode (CNE) fabricated in the quartz nanopipette. The interaction (approach, collision, and rebound) of a negatively charged NP and CNE modulates the open circuit potential (OCP) of the CNE creating a characteristic potential dip shown as the black solid trace.

single-particle level because of simplicity, sensitivity, cost-effectiveness, miniature dimension, and rapid sensing ability.[68] An electrochemical sensing platform converts the interaction between a single entity of interest and target (micro/nanoelectrode) to an electric current or potential. The electrochemical nanoimpact method which quantifies the single entity fluctuations in solution through current/potential is respectively referred to as amperometric/potentiometric nanoimpact methods. Owing to the convenient and rapid sensing method, single-particle collision nanoelelctrochemistry has become a powerful analytical tool especially for studying properties single NPs such as size, charge,

concentration, aggregation and catalytic reactivity.[80-87] Besides, nanoimpact studies find a plethora of applications in biosensing, bioelectrochemistry, and electrocatalysis.[66, 79, 88, 89]

the NP concentration and diffusion coefficient. The steady-state diffusion-controlled flux of the NPs at the nanoelectrode is given by,[68]

$$f_{diff} = 4D_{NP}C_{NP}R_{NE}N_A \ldots\ldots\ldots\ldots\ldots\ldots\ldots\ldots (1.13)$$

Where $D_{NP}$the diffusion coefficient of the NPs is, C_{NP} is the bulk concentration of the NP in particles/m^3, R_{NE} is the nanoelectrode radius and N_A is Avogadro's number. The Stokes-Einstein relationship is defined below.

$$D = \frac{k_B T}{6\pi\eta r}, \ldots\ldots\ldots\ldots\ldots\ldots\ldots\ldots (1.14)$$

Equation 1.14 estimates the diffusion coefficient D_{NP} of a spherical particle of radius r in a fluid of dynamic viscosity η at absolute temperature T (K). Where, $k_B(= 1.3803 \times 10^{-23}$ J K^{-1}) is the Boltzmann's constant and $\eta(= 1.0 \times 10^{-3} Kg/ms)$ is the dynamic viscosity of the water.

Figure 1.4a shows three different nanoimpact processes at the micro/nanoelectrode. Process 1, 2, and 3 respectively denote the electrochemical reduction of NP, mediated electronic transfer, and oxidation of NP during nanoimpact events.[79] Since the electrochemical current is monitored during nanoimpact, it is referred to as an amperometric method. The amperometric nanoimpact method is a facile electroanalytical

tool that can provide rich and quantitative information such as size, concentration, aggregation, and catalytic reactivity about the colliding nanoparticles.[66, 70, 90]

In potentiometric nanoimpact measurements, the nanoelectrode is immersed in the electrolyte. Initially, the nanoelectrode has a non-zero negative open circuit potential (OCP) as a result of the electrochemical difference between nanoelectrode and reference Ag/AgCl electrode. After the addition of NP, the OCP becomes stable at slightly different OCP values. When a single NP collides at the nanoelectrode, the charged interaction between nanoelectrode and NP modulates the OCP baseline creating a small potential dip referred to as a single nanoimpact event as shown in Figure 1.4b. The potentiometric nanoimpact method depends upon the direct potential or charge sensing mechanism: the presence of a charged NP alters the local potential of a nanoelectrode. For a multi-functional nanopipette, the potential detection is the combined effect of direct charge sensing (short-range) and voltage divider (long-range) mechanism.[19, 91]

To date, most single-NP collision experiments are measured by amperometric methods which usually require redox-active molecules and/or catalytically active NPs to amplify the electrochemical current to at least pA level for detection. Previous research has demonstrated that the NP collision events can also be detected by the open-circuit potential (OCP) change at the UME.[92] The potential change induced by the NP collision events is typically big enough for the potentiometric method and no extra signal amplification method is needed. Therefore, it is simpler and suitable for many biological applications. Besides, the noise of the potentiometric method is smaller at the same bandwidth, allowing for higher sensitivity and faster detection than commonly used amperometric method.

Therefore, the potentiometric detection method provides new opportunities to study various non-electroactive biological entities at a single-entity level with close to physiological conditions.

1.2.2: Optical Methods

1.2.2.1: Dark Field Microscopy (DFM)

Dark Field Microscopy (DFM) is a very simple yet highly effective imaging technique and has been widely used for clinical diagnostics, NP and biological samples detection, tracking, and analysis.[93-98] Recently, real-time analysis of the carbohydrate-protein interaction at the single nanoparticle level was achieved using DFM.[99] Furthermore, DFM has been an extensively popular analytical tool for quantifying cancer biomarkers, single-particle imaging, and high-precision enzyme profiling.[100-105] A simple bright field microscope can be converted to in a DFM simply by adding "stop". The stop is a piece of opaque material placed below the condenser which blocks the center of the light beam coming from the top of the microscope and forms the hollow cone of light needed for darkfield illumination as shown in Figure 1.5b.

In standard brightfield microscopy, a filled cone of light illuminates the sample (Figure 1.5a) where some of the light is absorbed/reflected by the sample and rest is directly collected by the objective producing the bright background. The image produced by the brightfield microscope lacks contrast. Besides, samples with relatively similar refractive indexes with the surrounding medium, e.g., biological samples, are barely visible in the brightfield microscope. A common strategy to enhance contrast for the biological sample is to stain them artificially which often requires killing them. Therefore, the brightfield

microscope is not suitable for obtaining a high contrast image of thin, transparent and unstained biological samples.

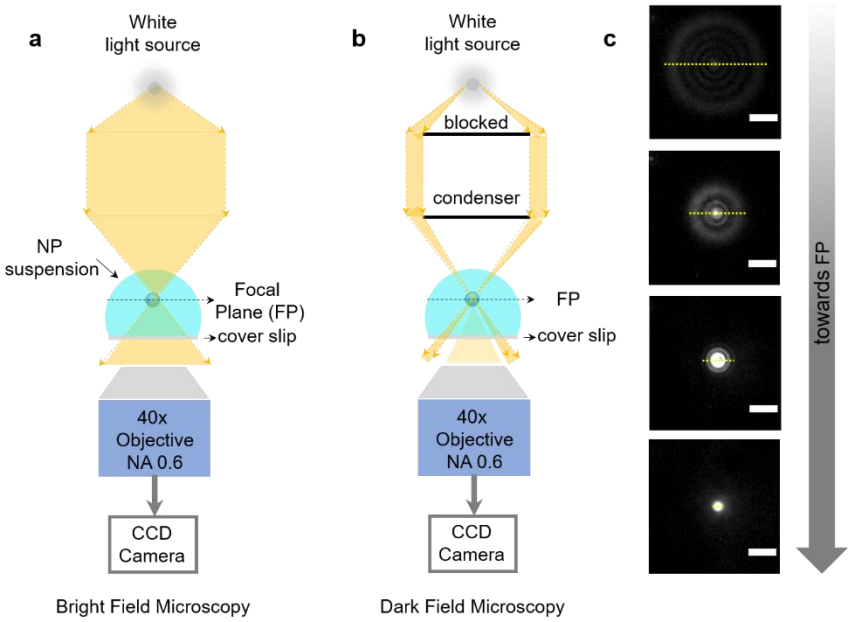

Figure 1. 5: Schematic of sample illumination strategy in brightfield and darkfield microscopy. (a) Schematic setup of the brightfield microscope. (b) Schematic setup of the darkfield microscope. (c) The consecutive high contrast DFM images of a single magnetoelectric nanoparticle (MENP) as it comes towards the focal plane (FP). The circular fringes are the diffraction patterns. At FP, there is just a bright spot without circular diffraction patterns. Yellow dotted lines denote the diameter of diffraction patterns. The scale bar is 10µm.

Dark field microscope works by utilizing the scattered beam from the sample and excluding all the unscattered beam of light that produces almost black background with bright objects on it. The schematic setup of the DFM is shown in Figure 1.5b and the experimental details about the DFM are presented in method section 2.2.2. Dark field microscope uses a condenser lens to form a hollow light cone and an objective lens (which is inside of the hollow light cone) collects only the scattered light from the sample as shown in Figure 1.5b. Without the sample, the DFM field of view is completely dark. However, with

samples such as nanoparticles, the samples appear as a bright spot with a dark background behind it as shown in Figure 1.5c. The scattered light collected by the objective goes to the CCD camera. The DFM images/videoes are recorded and analyzed using ImageJ software. Dark field microscope has superior contrast compared to the brightfield microscope. Besides, it can be used to observe live biological samples in liquid condition and require no staining.

1.3: Requirement of Multi-mode Analysis of Single Entities

Sensitivity and selectivity are two key requirements for a biosensor. In recent years, simultaneous multi-mode sensing of the single entity has attracted significant attention as a result of improved sensitivity and selectivity. Xie *et. al.* reported the simultaneous detection of ionic current and electrical potential change when individual DNA molecules translocated through the nanopore of a nanopore-nanowire sensor.[19] The integrated multi-mode nanopore-nanowire approach could enable large-scale integration with high intrinsic bandwidth. Larkin *et.al.* demonstrated the use of nanopore/zero-mode waveguide (ZMW) device for simultaneous detection of single-molecule fluorescence and changes in ionic current which showed the rapid, reversible and higher efficiency of molecular loading.[16] This integrated approach can contribute to the development of future single-molecule real-time sequencing applications in genetics and epigenetics. Concurrent ionic current changes and fluorescence signals were monitored by Song *et.al.* during single dye molecule transport *via* a carbon nanotube (CNT) nanopore.[17] Additionally, simultaneous measurement of ionic current changes and Surface-Enhanced Raman Spectroscoy (SERS) signals was reported by Cecchini *et.al*. as single GNPs transported *via* gold-coated

nanopore.[18] Surface-Enhanced Raman Spectroscoy integrated nanopore sensing scheme provides rich vibrational information on the analyte together with electrical signals from the nanopore. Similarly, Guo *et.al.* measured electrochemical current changes and Surface-SERS signals simultaneously during a single GNP collision at a gold nanoelectrode.[15] Thus, the integrated approach allows us to look at the same entity from different perspectives providing new insights in single entity measurements. Furthermore, the multi-mode analysis adds new functionality (control, manipulate and detect) to the existing method enhancing sensitivity and selectivity of the device. Here in my work, I want to use a nanopipette based multi-mode electrical sensing modality to detect and analyze range of single modal NPs including biomolecules.

1.4: Multi-mode Detection of Single Entities Using a Multi-functional Nanopipette

As a consequence of the recent technological advancement in the field of nanotechnology over the past two decades, the nanopore-based sensing modality has gained enormous popularity because of high sensitivity, selectivity, versatility yet cost-effective and facile fabrication. A nanopipette, as a subgroup of nanopores, is defined as a conically shaped nanopore and has been widely implemented in the study of single NPs, proteins, DNA and cell analysis.[106-109] One of the most intriguing features of the nanopipette is the low-cost, robust and easy fabrication and modification. Compared with other solid-state nanopores platforms (e.g., SiN_x, graphene, etc.. that usually require cleanroom facility, involve intricate and expensive instruments, are very time consuming and need nanofabrication expertise), the nanopipettes can be made inexpensively and reproducibly with a few tens of nanometer resolution from glass or quartz capillary tubes

within a minute. Furthermore, owing to its tip geometry, the nanopipettes can easily be integrated into the high precision positioning system as a scanning probe for the sub-nanometer spatial manipulation of single entities.[73, 110-114]

In recent years, nanopipette based multi-functional electrical sensing method with two nanodetectors (nanopore and nanoelectrode) at the nanopipette tip, has attracted many interests. The inspiration to design nanopore and nanoelectrode at the nanometer proximity raised from the morphology and excellent electrical and mechanical property of a single-walled CNTs which consists of an atomically thin conductive wall that acts as gating electrode and a nanochannel for the transport of single molecules. The main motivations behind the fabrication of nanopore-CNE multifunctional nanopipettes are to make a multi-mode electrical sensing platform for single molecules/NPs[115] and implement the platform for scanning probe techniques which is very powerful in the detection, analysis, and imaging of a single living cell.[73, 110, 111] The double-barrel nanopipettes were made from theta micropipettes and one of the barrels is converted to a CNE by filling the barrel with conductive materials, such as pyrolytic carbon through the pyrolysis process[111, 116] that results in a nanopore-CNE nanopipette which will be called multi-functional nanopipette throughout the text. The CNE and nanopore are very close to each other at the nanopipette tip to facilitate the concurrent measurements from both the detectors. As revealed from the SEM image (Figure 3.1), hemispherical CNE protrudes out from the nanopipette apex slightly.

Our nanopipette based multimode sensing method is highly innovative in that it integrates two electrical nanodetectors in a single nanopipette apex which can concurrently act as a feedback controller, nano sampler, electrical gating, manipulator and

electrochemical detector which will be very convenient for various single-entity detection and analysis. The facile, cost-effective, robust, versatile, sensitive and multi-functional sensing method will have a plethora of applications in drug delivery, clinical diagnostics, bioimaging, and single-cell analysis.

1.5: Overview of the Research Projects and Results

The main goal of my research project is to develop a multi-functional nanopipette based facile, label-free, versatile yet highly sensitive biosensing platform. To achieve that goal first, I fabricated and characterized the multi-functional nanopipette and performed a series of systematic studies using modal nanoparticles. Studies with GNPs have established that the multi-functional nanopipette is capable of sensing a single GNPs movement near the vicinity of the nanopipette apex via the simultaneous recording of the ionic current change in the nanopore and local potential change at the carbon nanoelectrode. To be able to sense bio-entities which are mainly dielectric, the multi-functional nanopipette based detection platform was first optimized for the detection of modal dielectric polystyrene (PS) nanoparticles of various sizes in an aqueous solution. To overcome the huge electrostatic repulsion between the PS NPs and the nanopipette wall, that severely limits the high throughput detection, dielectrophoretic (DEP) force applied via the nanoelectrode, which efficiently preconcentrated the PS NPs to form large assemblies outside the nanopipette tip, enabling high-throughput single NP analysis. Our study revealed how the interactions between NPs and between the NP and the nanopore surface affected the current and potential signals. On the basis of the simultaneous and correlated current and potential signals, the dynamic structures, and motions of PS NPs inside the large assembly were

studied. Our study revealed the small differences in the dynamic events between polarizable metallic NPs (e.g., GNPs) and non-polarizable dielectric NPs (e.g., PSNPs) during multi-NP structure formation and individual NP transport and translocation motions.

My second project focuses on the development of highly effective single entity manipulation and detection platform by implementing the multi-functional nanopipette. The nanoelectrode of a nanopore–nanoelectrode nanopipette was first employed to accumulate NPs in solution by dielectrophoresis (DEP). Instead of using amperometric methods, the continuous individual NP collision events on the nanoelectrode are sensitively detected by monitoring the open-circuit potential changes of the nanoelectrode. Metallic gold NPs (GNPs) and insulating polystyrene (PS) NPs with various sizes are used as the model NPs. As a result of the higher conductivity and polarizability of GNPs, the collision motion of a GNP is different from that of a PS NP. The difference is distinct in the shape of the transient potential change and its first-time derivative detected by the nanoelectrode. Therefore, the collision events by metallic and insulating NPs on a nanoelectrode can be differentiated from their polarizability. The DEP induced NP separation and cluster formation were also probed in detail in the concentrated mixture of PS NPs and GNPs.

I further demonstrated the sensitivity of the multi-functional nanopipette by measuring small surface charge increment on the surface of magneto-electric nanoparticles (MENPs) under an AC B-field during MENP-CNE collision events. My research, for the first time, implements a single-entity approach for probing AC B-field induced strain mediated surface potential enhancement on MENPs (composed of a piezoelectric shell as

$BaTiO_3$ and ferromagnetic shell as $CoFe_2O_4$) surface using a MENP-CNE collision method. The results confirmed that AC B-field stimulation (60 Oe for 10 minutes exposure time) makes MENP highly polarizable and cause magnetostrictive strain-induced localized surface potential (~1 mV) enhancement. The surface potential enhancement of the MENP is associated with the presence of a piezoelectric shell whereas magnetic nanoparticles (MNPs) were found unaffected under identical stimulation. Such observed phenomena in a controlled manner can be useful to achieve targeted transfection and drug delivery, even inside a cell, to cure targeted diseases. Altogether, these results suggest that a multifunctional nanopipette can sense a wide variety of modal nanoparticles; metallic, insulating, magnetic and magnetoelectric which prepare me to use multifunctional nanopipette platform for single biomolecule detection and analysis.

After successfully demonstrating the capability of the multi-functional nanopipette for detection and analysis variety of modal NPs, it was further used to detect and analyze the single proteins molecules. Commonly available proteins such as bovine hemoglobin, horse heart cytochrome c, horse spleen ferritin, lysozyme from chicken egg white, and bovine serum albumin were used for the measurement. The simultaneously monitored ionic current at the nanopore and surface potential changes at the nanoelectrode revealed single protein translocation via nanopore or collision with the nanoelectrode. When a protein molecule arrives at the vicinity of the electrically floating nanoelectrode, open-circuit potential (OCP) changes are detected at the nanoelectrode. The protein-CNE collision results revealed the motion differences between different proteins, the net charge contained by the protein and qualitative information about the properties such as rigidity and flexibility which is further supported by molecular dynamics (MD) simulation. Compared

with the ionic current change, the OCP changes can be detected with better signal-to-noise ratio and higher time resolution and larger sensing range thus high throughput detection which provides new opportunities to study various biological entities at a single-entity level with close to physiological conditions.

Finite element numerical simulations were also performed to understand the fundamental charge sensing mechanism during the NP-CNE collision of the charged NPs *via* multi-functional nanopipette under identical experimental conditions. The simulation results follow the experimental results.

In summary, my dissertation presents the fabrication, development, and optimization of the nanopipette electrical biosensing platform. First, it presents a systematic study using modal nanoparticles and tries to understand the underlying mechanism via numerical simulation. With experimental and simulation results, my dissertation describes a facile, cost-effective, versatile, sensitive, easy integration with another sensing platform, robust and label-free electrical sensing method to study single NPs to biomolecules primarily using a charge sensing mechanism. Overall, my dissertation, will be a valuable contribution to fill the knowledge gap in the field of biophysics research and provide new insights into the multimode analysis of single entities.

1.6: References

1. Wang, Y., X. Shan, and N. Tao, *Emerging tools for studying single entity electrochemistry*. Faraday Discussions, 2016. **193**(0): p. 9-39.
2. Todd, J., et al., *Ultrasensitive Flow-based Immunoassays Using Single-Molecule Counting*. Clinical Chemistry, 2007. **53**(11): p. 1990.

3. Müller, S. and G. Nebe-von-Caron, *Functional single-cell analyses: flow cytometry and cell sorting of microbial populations and communities.* FEMS Microbiology Reviews, 2010. **34**(4): p. 554-587.

4. Shen, H., et al., *Single Particle Tracking: From Theory to Biophysical Applications.* Chemical Reviews, 2017. **117**(11): p. 7331-7376.

5. Tessler, L.A., J.G. Reifenberger, and R.D. Mitra, *Protein Quantification in Complex Mixtures by Solid Phase Single-Molecule Counting.* Analytical Chemistry, 2009. **81**(17): p. 7141-7148.

6. Wang, S., et al., *Label-free imaging, detection, and mass measurement of single viruses by surface plasmon resonance.* Proceedings of the National Academy of Sciences, 2010. **107**(37): p. 16028.

7. Decrop, D., et al., *Optical Manipulation of Single Magnetic Beads in a Microwell Array on a Digital Microfluidic Chip.* Analytical Chemistry, 2016. **88**(17): p. 8596-8603.

8. Zhang, Y., et al., *Single-Molecule Study on Intermolecular Interaction between C60 and Porphyrin Derivatives: Toward Understanding the Strength of the Multivalency.* Langmuir, 2009. **25**(12): p. 6627-6632.

9. Ven, K., et al., *Target Confinement in Small Reaction Volumes Using Microfluidic Technologies: A Smart Approach for Single-Entity Detection and Analysis.* ACS Sensors, 2018. **3**(2): p. 264-284.

10. Long, Z., et al., *Recent Advances in Solid Nanopore/Channel Analysis.* Analytical Chemistry, 2018. **90**(1): p. 577-588.

11. Cadinu, P., et al., *Double Barrel Nanopores as a New Tool for Controlling Single-Molecule Transport.* Nano Letters, 2018. **18**(4): p. 2738-2745.

12. Mathwig, K., et al., *Challenges of Biomolecular Detection at the Nanoscale: Nanopores and Microelectrodes.* Analytical Chemistry, 2015. **87**(11): p. 5470-5475.

13. Duan, R., F. Xia, and L. Jiang, *Constructing Tunable Nanopores and Their Application in Drug Delivery.* ACS Nano, 2013. **7**(10): p. 8344-8349.

14. Reiner, J.E., et al., *Disease Detection and Management via Single Nanopore-Based Sensors.* Chemical Reviews, 2012. **112**(12): p. 6431-6451.

15. Guo, J., et al., *Monitoring the Dynamic Process of Formation of Plasmonic Molecular Junctions during Single Nanoparticle Collisions.* Small, 2018. **14**(15): p. 1704164.

16. Larkin, J., et al., *Reversible Positioning of Single Molecules inside Zero-Mode Waveguides.* Nano Letters, 2014. **14**(10): p. 6023-6029.

17. Song, W., et al., *Optical and Electrical Detection of Single-Molecule Translocation through Carbon Nanotubes.* ACS Nano, 2013. **7**(1): p. 689-694.

18. Cecchini, M.P., et al., *Rapid Ultrasensitive Single Particle Surface-Enhanced Raman Spectroscopy Using Metallic Nanopores.* Nano Letters, 2013. **13**(10): p. 4602-4609.

19. Xie, P., et al., *Local electrical potential detection of DNA by nanowire–nanopore sensors.* Nature Nanotechnology, 2012. **7**(2): p. 119-125.

20. Toh, H.S. and R.G. Compton, *Electrochemical detection of single micelles through 'nano-impacts'.* Chemical Science, 2015. **6**(8): p. 5053-5058.

21. Kim, B.-K., J. Kim, and A.J. Bard, *Electrochemistry of a Single Attoliter Emulsion Droplet in Collisions.* Journal of the American Chemical Society, 2015. **137**(6): p. 2343-2349.

22. Boika, A., S.N. Thorgaard, and A.J. Bard, *Monitoring the Electrophoretic Migration and Adsorption of Single Insulating Nanoparticles at Ultramicroelectrodes.* The Journal of Physical Chemistry B, 2013. **117**(16): p. 4371-4380.

23. Varongchayakul, N., et al., *Single-molecule protein sensing in a nanopore: a tutorial.* Chemical Society Reviews, 2018. **47**(23): p. 8512-8524.

24. Shi, W., A.K. Friedman, and L.A. Baker, *Nanopore Sensing.* Analytical Chemistry, 2017. **89**(1): p. 157-188.

25. Wanunu, M., *Nanopores: A journey towards DNA sequencing.* Physics of Life Reviews, 2012. **9**(2): p. 125-158.

26. Kasianowicz, J.J., et al., *Characterization of individual polynucleotide molecules using a membrane channel.* Proc Natl Acad Sci U S A, 1996. **93**(24): p. 13770-3.

27. Chuah, K., et al., *Nanopore blockade sensors for ultrasensitive detection of proteins in complex biological samples.* Nature Communications, 2019. **10**(1): p. 2109.

28. Han, A., et al., *Label-Free Detection of Single Protein Molecules and Protein−Protein Interactions Using Synthetic Nanopores.* Analytical Chemistry, 2008. **80**(12): p. 4651-4658.

29. Li, W., et al., *Single Protein Molecule Detection by Glass Nanopores.* ACS Nano, 2013. **7**(5): p. 4129-4134.

30. Zhang, Y., et al., *Short channel effects on electrokinetic energy conversion in solid-state nanopores.* Scientific Reports, 2017. **7**(1): p. 46661.

31. Xie, Y., et al., *Electric energy generation in single track-etched nanopores.* Applied Physics Letters, 2008. **93**(16): p. 163116.

32. Yeh, H.-C., C.-C. Chang, and R.-J. Yang, *Reverse electrodialysis in conical-shaped nanopores: salinity gradient-driven power generation.* RSC Advances, 2014. **4**(6): p. 2705-2714.

33. Sahu, S. and M. Zwolak, *Ionic selectivity and filtration from fragmented dehydration in multilayer graphene nanopores.* Nanoscale, 2017. **9**(32): p. 11424-11428.

34. Heiranian, M., A.B. Farimani, and N.R. Aluru, *Water desalination with a single-layer MoS2 nanopore.* Nature Communications, 2015. **6**(1): p. 8616.

35. Xu, Y., et al., *Detection of Viral Pathogens With Multiplex Nanopore MinION Sequencing: Be Careful With Cross-Talk.* Frontiers in microbiology, 2018. **9**: p. 2225-2225.

36. Cretu Stancu, M., et al., *Mapping and phasing of structural variation in patient genomes using nanopore sequencing.* Nature Communications, 2017. **8**(1): p. 1326.

37. Howorka, S. and Z. Siwy, *Nanopores and Nanochannels: From Gene Sequencing to Genome Mapping.* ACS Nano, 2016. **10**(11): p. 9768-9771.

38. Jain, M., et al., *Nanopore sequencing and assembly of a human genome with ultra-long reads.* Nature Biotechnology, 2018. **36**(4): p. 338-345.

39. Bowden, R., et al., *Sequencing of human genomes with nanopore technology.* Nature Communications, 2019. **10**(1): p. 1869.

40. Coulter, W.H., *Means for counting particles suspended in a fluid. U.S.Patent 2,656,508, filed August 27, 1949 and issued October 20,.* 1953.

41. Firnkes, M., et al., *Electrically Facilitated Translocations of Proteins through Silicon Nitride Nanopores: Conjoint and Competitive Action of Diffusion, Electrophoresis, and Electroosmosis.* Nano Letters, 2010. **10**(6): p. 2162-2167.

42. German, S.R., et al., *Controlling Nanoparticle Dynamics in Conical Nanopores.* The Journal of Physical Chemistry C, 2013. **117**(1): p. 703-711.

43. Wu, J., et al., *Highly efficient electroosmotic flow through functionalized carbon nanotube membranes.* Nanoscale, 2011. **3**(8): p. 3321-3328.

44. Miller, S.A., V.Y. Young, and C.R. Martin, *Electroosmotic Flow in Template-Prepared Carbon Nanotube Membranes.* Journal of the American Chemical Society, 2001. **123**(49): p. 12335-12342.

45. Lan, W.-J., et al., *Effect of Surface Charge on the Resistive Pulse Waveshape during Particle Translocation through Glass Nanopores.* The Journal of Physical Chemistry C, 2014. **118**(5): p. 2726-2734.

46. White, H.S. and A. Bund, *Ion Current Rectification at Nanopores in Glass Membranes.* Langmuir, 2008. **24**(5): p. 2212-2218.

47. Kasianowicz, J.J., et al., Proc. Natl. Acad. Sci. U.S.A., 1996. **93**: p. 13770.

48. Biesemans, A., M. Soskine, and G. Maglia, *A Protein Rotaxane Controls the Translocation of Proteins Across a ClyA Nanopore.* Nano Letters, 2015. **15**(9): p. 6076-6081.

49. Fahie, M., C. Chisholm, and M. Chen, *Resolved single-molecule detection of individual species within a mixture of anti-biotin antibodies using an engineered monomeric nanopore.* ACS nano, 2015. **9**(2): p. 1089-1098.

50. Gu, L.-Q., et al., *Stochastic sensing of organic analytes by a pore-forming protein containing a molecular adapter.* Nature, 1999. **398**(6729): p. 686-690.

51. Ettedgui, J., J.J. Kasianowicz, and A. Balijepalli, *Single Molecule Discrimination of Heteropolytungstates and Their Isomers in Solution with a Nanometer-Scale Pore.* Journal of the American Chemical Society, 2016. **138**(23): p. 7228-7231.

52. Howorka, S., S. Cheley, and H. Bayley, *Sequence-specific detection of individual DNA strands using engineered nanopores.* Nature Biotechnology, 2001. **19**(7): p. 636-639.

53. Zahid, O.K., et al., *Sequence-Specific Recognition of MicroRNAs and Other Short Nucleic Acids with Solid-State Nanopores.* Nano letters, 2016. **16**(3): p. 2033-2039.

54. Akeson, M., et al., *Microsecond Time-Scale Discrimination Among Polycytidylic Acid, Polyadenylic Acid, and Polyuridylic Acid as Homopolymers or as Segments Within Single RNA Molecules.* Biophysical Journal, 1999. **77**(6): p. 3227-3233.

55. Braha, O., et al., *Simultaneous stochastic sensing of divalent metal ions.* Nature Biotechnology, 2000. **18**(9): p. 1005-1007.

56. Ying, Y.-L., C. Cao, and Y.-T. Long, *Single molecule analysis by biological nanopore sensors.* Analyst, 2014. **139**(16): p. 3826-3835.

57. Manara, R.M.A., E. Jayne Wallace, and S. Khalid, *DNA sequencing with MspA: Molecular Dynamics simulations reveal free-energy differences between sequencing and non-sequencing mutants.* Scientific Reports, 2015. **5**(1): p. 12783.

58. Tiwari, P.B., et al., *Quantitative study of protein–protein interactions by quartz nanopipettes.* Nanoscale, 2014. **6**(17): p. 10255-10263.

59. Traversi, F., et al., *Detecting the translocation of DNA through a nanopore using graphene nanoribbons.* Nature Nanotechnology, 2013. **8**(12): p. 939-945.

60. Wang, Y., et al., *Fabrication of multiple nanopores in a SiNx membrane via controlled breakdown.* Scientific Reports, 2018. **8**(1): p. 1234.

61. Hall, A.R., et al., *Hybrid pore formation by directed insertion of α-haemolysin into solid-state nanopores.* Nature Nanotechnology, 2010. **5**(12): p. 874-877.

62. Miles, B.N., et al., *Single molecule sensing with solid-state nanopores: novel materials, methods, and applications.* Chemical Society Reviews, 2013. **42**(1): p. 15-28.

63. Geng, J., et al., *Stochastic transport through carbon nanotubes in lipid bilayers and live cell membranes.* Nature, 2014. **514**(7524): p. 612-615.

64. Zhou, Y., et al., *Ion channel probes for scanning ion conductance microscopy.* Langmuir : the ACS journal of surfaces and colloids, 2014. **30**(50): p. 15351-15355.

65. Bell, N.A.W., et al., *DNA Origami Nanopores.* Nano Letters, 2012. **12**(1): p. 512-517.

66. Peng, Y.-Y., et al., *Stochastic Collision Nanoelectrochemistry: A Review of Recent Developments.* ChemElectroChem, 2017. **4**(5): p. 977-985.

67. McKelvey, K., et al., *Nanopipettes as a tool for single nanoparticle electrochemistry.* Current Opinion in Electrochemistry, 2017. **6**(1): p. 4-9.

68. Xiao, X. and A.J. Bard, *Observing Single Nanoparticle Collisions at an Ultramicroelectrode by Electrocatalytic Amplification.* Journal of the American Chemical Society, 2007. **129**(31): p. 9610-9612.

69. Quinn, B.M., P.G. van't Hof, and S.G. Lemay, *Time-Resolved Electrochemical Detection of Discrete Adsorption Events.* Journal of the American Chemical Society, 2004. **126**(27): p. 8360-8361.

70. Baker, L.A., *Perspective and Prospectus on Single-Entity Electrochemistry.* Journal of the American Chemical Society, 2018. **140**(46): p. 15549-15559.

71. Mirkin, M.V., et al., *Electrochemistry at One Nanoparticle.* Accounts of Chemical Research, 2016. **49**(10): p. 2328-2335.

72. Han, L., et al., *Single molecular catalysis of a redox enzyme on nanoelectrodes.* Faraday Discussions, 2016. **193**(0): p. 133-139.

73. Takahashi, Y., et al., *Topographical and electrochemical nanoscale imaging of living cells using voltage-switching mode scanning electrochemical microscopy.* Proceedings of the National Academy of Sciences, 2012. **109**(29): p. 11540.

74. Kranz, C., *Recent advancements in nanoelectrodes and nanopipettes used in combined scanning electrochemical microscopy techniques.* Analyst, 2014. **139**(2): p. 336-352.

75. Clausmeyer, J. and W. Schuhmann, *Nanoelectrodes: Applications in electrocatalysis, single-cell analysis and high-resolution electrochemical imaging.* TrAC Trends in Analytical Chemistry, 2016. **79**: p. 46-59.

76. Zhang, J., et al., *New Frontiers and Challenges for Single-Cell Electrochemical Analysis.* ACS Sensors, 2018. **3**(2): p. 242-250.

77. Ying, Y.-L., et al., *Advanced electroanalytical chemistry at nanoelectrodes.* Chemical Science, 2017. **8**(5): p. 3338-3348.

78. Zhou, X.S., et al., *Transient electrochemistry: beyond simply temporal resolution.* Chemical Communications, 2016. **52**(2): p. 251-263.

79. Cheng, W. and R.G. Compton, *Electrochemical detection of nanoparticles by 'nano-impact' methods.* TrAC Trends in Analytical Chemistry, 2014. **58**: p. 79-89.

80. Tschulik, K., et al., *Coulometric sizing of nanoparticles: Cathodic and anodic impact experiments open two independent routes to electrochemical sizing of Fe3O4 nanoparticles.* Nano Research, 2013. **6**(11): p. 836-841.

81. Batchelor-McAuley, C., et al., *In situ nanoparticle sizing with zeptomole sensitivity.* Analyst, 2015. **140**(15): p. 5048-5054.

82. Dick, J.E., C. Renault, and A.J. Bard, *Observation of Single-Protein and DNA Macromolecule Collisions on Ultramicroelectrodes.* Journal of the American Chemical Society, 2015. **137**(26): p. 8376-8379.

83. Boika, A. and A.J. Bard, *Time of First Arrival in Electrochemical Collision Experiments as a Measure of Ultralow Concentrations of Analytes in Solution.* Analytical Chemistry, 2015. **87**(8): p. 4341-4346.

84. Krause, K.J., A. Yakushenko, and B. Wolfrum, *Stochastic On-Chip Detection of Subpicomolar Concentrations of Silver Nanoparticles.* Analytical Chemistry, 2015. **87**(14): p. 7321-7325.

85. Lees, J.C., et al., *Nanoparticle Impacts Show High-Ionic-Strength Citrate Avoids Aggregation of Silver Nanoparticles.* ChemPhysChem, 2013. **14**(17): p. 3895-3897.

86. Dasari, R., et al., *Electrochemical Monitoring of Single Nanoparticle Collisions at Mercury-Modified Platinum Ultramicroelectrodes.* ACS Nano, 2014. **8**(5): p. 4539-4546.

87. Kwon, S.J., et al., *Stochastic electrochemistry with electrocatalytic nanoparticles at inert ultramicroelectrodes—theory and experiments.* Physical Chemistry Chemical Physics, 2011. **13**(12): p. 5394-5402.

88. Oja, S.M., et al., *Nanoscale Electrochemistry Revisited.* Analytical Chemistry, 2016. **88**(1): p. 414-430.

89. Rees, N.V., *Electrochemical insight from nanoparticle collisions with electrodes: A mini-review.* Electrochemistry Communications, 2014. **43**: p. 83-86.

90. Anderson, T.J. and B. Zhang, *Single-Nanoparticle Electrochemistry through Immobilization and Collision.* Accounts of Chemical Research, 2016. **49**(11): p. 2625-2631.

91. Panday, N., et al., *Simultaneous Ionic Current and Potential Detection of Nanoparticles by a Multifunctional Nanopipette.* ACS Nano, 2016. **10**(12): p. 11237-11248.

92. Zhou, H., et al., *Observation of Single Metal Nanoparticle Collisions by Open Circuit (Mixed) Potential Changes at an Ultramicroelectrode.* Journal of the American Chemical Society, 2012. **134**(32): p. 13212-13215.

93. Liu, X., et al., *Single Gold Nanoparticle-Based Colorimetric Detection of Picomolar Mercury Ion with Dark-Field Microscopy.* Analytical Chemistry, 2016. **88**(4): p. 2119-2124.

94. Benenson, A.S., M.R. Islam, and W.B. Greenough, 3rd, *RAPID IDENTIFICATION OF VIBRIO CHOLERAE BY DARKFIELD MICROSCOPY.* Bulletin of the World Health Organization, 1964. **30**(6): p. 827-831.

95. Jamjoom, G.A., *Dark-field microscopy for detection of malaria in unstained blood films.* Journal of Clinical Microbiology, 1983. **17**(5): p. 717.

96. Hu, M., et al., *Dark-field microscopy studies of single metal nanoparticles: understanding the factors that influence the linewidth of the localized surface plasmon resonance.* Journal of Materials Chemistry, 2008. **18**(17): p. 1949-1960.

97. Liu, H., C. Dong, and J. Ren, *Tempo-Spatially Resolved Scattering Correlation Spectroscopy under Dark-Field Illumination and Its Application to Investigate Dynamic Behaviors of Gold Nanoparticles in Live Cells.* Journal of the American Chemical Society, 2014. **136**(7): p. 2775-2785.

98. Larsen, S.A., B.M. Steiner, and A.H. Rudolph, *Laboratory diagnosis and interpretation of tests for syphilis.* Clinical microbiology reviews, 1995. **8**(1): p. 1-21.

99. Jin, H.-Y., et al., *Analyzing Carbohydrate–Protein Interaction Based on Single Plasmonic Nanoparticle by Conventional Dark Field Microscopy.* ACS Applied Materials & Interfaces, 2015. **7**(22): p. 12249-12253.

100. Li, J., et al., *The aptamer-thrombin-aptamer sandwich complex-bridged gold nanoparticle oligomers for high-precision profiling of thrombin by dark field microscopy.* Analytica Chimica Acta, 2018. **1028**: p. 66-76.

101. Ju, S., et al., *Supersensitive single-particle plasmonic scattering-based cancer antigen 125 nanoimmunosensor by enhanced dark-field microscopy with dual-detection mode.* Sensors and Actuators B: Chemical, 2017. **245**: p. 1015-1022.

102. Poon, C.-Y., et al., *Quantification of Cancer Biomarkers in Serum Using Scattering-Based Quantitative Single Particle Intensity Measurement with a Dark-Field Microscope.* Analytical Chemistry, 2016. **88**(17): p. 8849-8856.

103. Luo, W., et al., *Nanoprecipitation of Fluorescent Conjugated Polymer onto the Surface of Plasmonic Nanoparticle for Fluorescence/Dark-Field Dual-Modality Single Particle Imaging.* Analytical Chemistry, 2016. **88**(13): p. 6827-6835.

104. Sun, D. and T.Y. Hu, *A low cost mobile phone dark-field microscope for nanoparticle-based quantitative studies.* Biosensors and Bioelectronics, 2018. **99**: p. 513-518.

105. Shen, H., et al., *3D darkfield imaging and single particle tracking of peptide-coated nanocargoes in live cells.* Analytical Methods, 2014. **6**(23): p. 9202-9205.

106. Wang, Y., et al., *Resistive-pulse measurements with nanopipettes: detection of Au nanoparticles and nanoparticle-bound anti-peanut IgY.* Chemical Science, 2013. **4**(2): p. 655-663.

107. Freedman, K.J., et al., *Nanopore sensing at ultra-low concentrations using single-molecule dielectrophoretic trapping.* Nature Communications, 2016. **7**: p. 10217.

108. Fosdick, S.E., et al., *Correlated Electrochemical and Optical Tracking of Discrete Collision Events.* Journal of the American Chemical Society, 2013. **135**(16): p. 5994-5997.

109. Kleijn, S.E.F., et al., *Landing and Catalytic Characterization of Individual Nanoparticles on Electrode Surfaces.* Journal of the American Chemical Society, 2012. **134**(45): p. 18558-18561.

110. Takahashi, Y., et al., *Multifunctional Nanoprobes for Nanoscale Chemical Imaging and Localized Chemical Delivery at Surfaces and Interfaces.* Angewandte Chemie International Edition, 2011. **50**(41): p. 9638-9642.

111. Takahashi, Y., et al., *Simultaneous Noncontact Topography and Electrochemical Imaging by SECM/SICM Featuring Ion Current Feedback Regulation.* Journal of the American Chemical Society, 2010. **132**(29): p. 10118-10126.

112. Comstock, D.J., et al., *Integrated Ultramicroelectrode−Nanopipet Probe for Concurrent Scanning Electrochemical Microscopy and Scanning Ion Conductance Microscopy.* Analytical Chemistry, 2010. **82**(4): p. 1270-1276.

113. Zhou, L., et al., *Capturing Rare Conductance in Epithelia with Potentiometric-Scanning Ion Conductance Microscopy.* Analytical Chemistry, 2016. **88**(19): p. 9630-9637.

114. Perry, D., et al., *Simultaneous Nanoscale Surface Charge and Topographical Mapping.* ACS Nano, 2015. **9**(7): p. 7266-7276.

115. Hu, K., et al., *Open Carbon Nanopipettes as Resistive-Pulse Sensors, Rectification Sensors, and Electrochemical Nanoprobes.* Analytical Chemistry, 2014. **86**(18): p. 8897-8901.

116. Lai, S.C.S., et al., *Visualizing Zeptomole (Electro)Catalysis at Single Nanoparticles within an Ensemble.* Journal of the American Chemical Society, 2011. **133**(28): p. 10744-10747.

CHAPTER 2: MATERIALS AND METHODS

My dissertation used electrical, optical and scanning probe microscopy techniques to study and analyze single nanoparticles and single biomolecules. The nanopore-carbon nanoelectrode (CNE) nanopipette is used to concurrently acquire ionic current from the nanopore and local electric potential from the nanoelectrode. The nanopore-CNE nanopipette is also called a multi-functional nanopipette. Optical methods such as dark-field microscope (DFM) and single-molecule fluorescence microscope were used to monitor the motion of the single entities. Scanning probe microscopy (such as AFM and SICM) was also used to study and analyze single nanoparticles and cells. This section provides details on the fabrication and characterization of the electrical and scanning probes. Altogether, the chapter presents all the experimental methods and theoretical calculations, by projects, which I performed as a part of my dissertation research.

2.1: Probing Dynamic Events of Dielectric Nanoparticles by Multi-functional Nanopipettes

The multi-functional nanopipette was used to probe single dielectric polystyrene nanoparticles (PS) NP events. Nanopipettes are a highly versatile and cost-effective electrical method for probing single entities. Depending on the purpose of the study, different nanopipettes can be utilized. For ionic current based detection only, a single barrel borosilicate glass or quartz nanopipette was used. The single barrel quartz nanopipette was used to prepare a single barrel CNE to monitor local electric potential and to probe electrochemistry at the nanoelectrode *via* nanoelectrode collision. Here the detection is mainly as a result of diffusion. The measurement from a single barrel CNE serves as a control for the nanoelectrode collisions as it is free from external forces such as

electrophoresis. For the simultaneous recording of the ionic current and electrical potential, double-barrel quartz theta nanopipette (multi-functional nanopipette) was used where the induced events are not solely the result of diffusion. The detailed fabrication and characterization procedures are explained below.

2.1.1: Single Barrel Quartz Nanopipette

The single barrel quartz capillary tubes (Q100-70-7.5), Sutter Instrument) were cleaned by piranha[1] (*caution: Piranha solutions are highly corrosive and must be handled with extreme caution!*) for 30 minutes. The cleaned quartz pipettes were repeatedly rinsed with deionized water until pH meter reads neutral pH, and then dried in an oven at 120^{o}C overnight. Quartz nanopipettes were fabricated from these cleaned capillary tubes by using a laser-based pipette puller (P-2000, Sutter Instrument) with the following one-line parameters: HEAT=680, FIL=4, VEL=60, DEL=170, PUL=180.

2.1.2: Dual Barrel Quartz Theta Nanopipette

The quartz theta capillary tubes (FG-G QT120-90-7.5, Sutter Instrument) as shown in Figure 2.1a were first cleaned by Piranha (*caution: Piranha solutions are highly corrosive and need to be handled with extreme caution!*) for 30 minutes and then repeatedly rinsed with deionized water until pH meter reads neutral pH and dried in an oven at 120^{o}C for overnight. Quartz dual nanopore nanopipettes were fabricated from these cleaned capillary tubes by using a laser pipette puller (P-2000, Sutter Instrument) with the following one-line parameters: HEAT=825, FIL=3, VEL=40, DEL=220, PUL=190 for nanopore-carbon-nanoelectrode fabrication. Different parameters were used during the pulling to adjust the pore diameter according to the purpose of the experiment. It must be

noted that the reported nanopore diameter may vary depending upon humidity, room temperature, and proper loading (which may vary person to person) of the quartz capillary in the P-2000 puller. Now the theta nanopipette is ready for pyrolytic carbon fabrication.

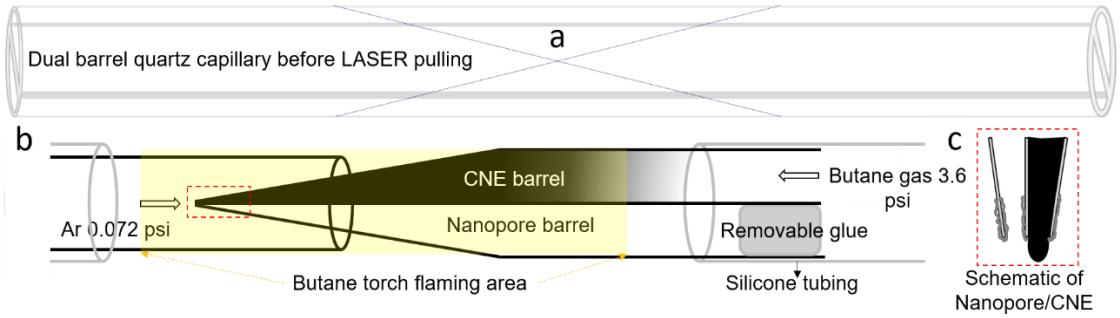

Figure 2.1: (a) Schematic illustration of making a nanopore-CNE theta nanopipette using Laser Puller (not-to-scale). A single quartz theta capillary tube is pulled to create two symmetrical theta nanopipette. (b) Fabrication of the nanopore-CNE nanopipette from a theta nanopipette. (c) The cartoon-illustration of nanopore-CNE nanopipette tip. We assume that the protruded CNE has a roughly hemispherical shape.

2.1.3: Pyrolytic Carbon Nanoelectrode (CNE) Fabrication.

The preparation of nanopore-carbon nanoelectrode nanopipette has been previously explained in detail.[1] In short, cleaned quartz theta pipettes (FG-G QT120-90-7.5, Shutter Instruments) were pulled using a laser pipette puller (P-2000, Sutter Instrument) with the following parameters: HEAT=825, FIL=3, VEL=40, DEL=220, PUL=190 to create a dual nanopore nanopipette. To make a solid pyrolytic carbon nanoelectrode (CNE), butane gas flowed through one of the barrels of the dual-barrel nanopipette under carefully controlled pressure. The nanopipette tip region was then heated with a torch (Blazer) for just 30-40 seconds from the tip towards the base slowly for about 3-4 times (see Figure 2.1b). Note that the nanopipette tip must be kept away from the central blue flame of the blazer to avoid tip bending and breaking.

2.1.4: The Nanopore-Nanoelectrode Nanopipette Characterization

The fabricated nanopore-carbon nanoelectrode nanopipette was characterized using a simple bright-field optical microscope, SEM, and electrical and electrochemical methods. The pore conductance measurement (*i.e.,* IV measurements), SEM, and bright-field images were used to measure nanopipette tip geometry. The electrochemical measurement was used to estimate the protruded carbon nanoelectrode size.

2.1.4.1: Bright Field Imaging

The fabricated nanopore-CNE nanopipette is first characterized via a bright-field optical microscope. An optical microscope (Nikon Eclipse Ti-U) with a 10X lens was also used. Figure 2.4 (top) represents the typical optical images of theta nanopipettes after carbon deposition. The black side denotes the carbon-filled barrel and faintly grey side denote the nanopore barrel.

2.1.4.2: SEM

Field emission scanning electron microscope (SEM) (FE-SEM, JEOL JSM-6330F) was used to characterize the nanopore-CNE nanopipette geometry. The nanopipette was precut to ~1 cm from tip and the exterior of the nanopipette coated with ~5 nm thick gold using an auto sputter coater (PELCOSC-7) to make nanopipette surface conducting and avoid the charging effect during SEM measurements. Figure 2.4 shows the SEM characterization of the double-barrel theta nanopipette tip. The size of the nanopore and the carbon nanoelectrode of nanopore-CNE nanopipette is shown in Figure 2.2. The cone angle from the SEM images of the 5 representative double-barrel quartz theta nanopipette

was estimated at 11°. The estimated half cone angle for the nanopipette was used for the estimation of nanopore diameter from IV measurement and in numerical simulations.

2.1.4.3: Estimation of the Nanopore Diameter from the IV Measurement

A simple analytical equation shown below is used for the estimation of nanopore diameter after CNE fabrication. The half cone angle of the nanopipette is 5.5 ± 0.5^{o} according to the SEM images. The mean nanopore resistance (R_p) is determined from the IV measurements in 10 mM PBS. The κ for 10 mM PBS (at pH 7.4) is determined to be 1312 µS/cm from conductivity measurements. Figure 2.2a shows the distribution of IV curves in a heat map from 56 nanopipettes. Figure 2.2b shows the distribution of R_p, derived from the IV curves. The mean value of R_p was found to be 2.99 ± 0.21 GΩ from the Gaussian fit. From the R_p distribution, the mean nanopore diameter is 73 nm and the majority of the nanopipettes have the diameter ranging from 60-90 nm.

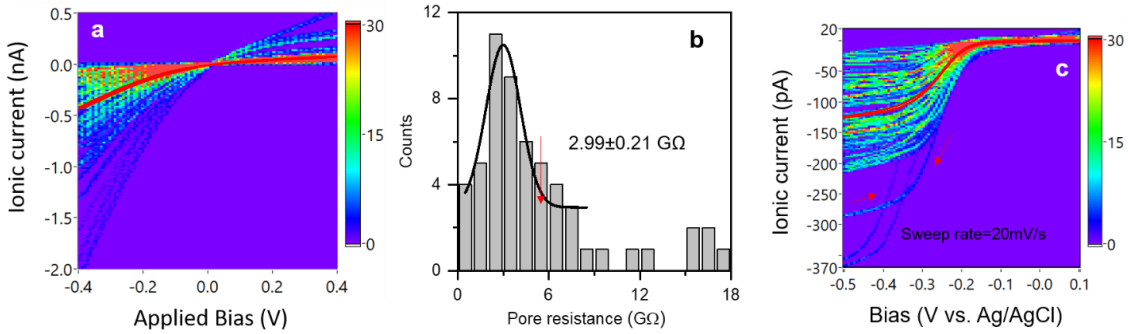

Figure 2.2: (a) The heat map of IV curves from 56 nanopipettes after CNE fabrication. The overlaid red curve represents the average of all IV curves. (b) The histogram of the pore resistance R_p derived from the IV curves. The nanopipettes, which have a resistance value greater than 5.5 GΩ (indicated by red solid arrow), were not used in the experiments. The black curve is a Gaussian fit to the histogram. (c) The steady-state CVs (at a sweep rate 20 mV/s) from 56 CNEs in 1x PBS solution containing 1mM Ru $(NH_3)^{6+}$ ions. The overlaid red curve is the average of all CVs with i_d = 125 pA, corresponding to an averaged CNE surface area 0.49 µm^2. Red arrows indicate the potential sweep direction.

2.1.4.4: Characterization of the Nanoelectrode Size Using Cyclic Voltammetry (CV) Method

Details of the fabrication of CNE can be found in our previous publication[1] and briefly discussed in section 2.1.1.3. Figure S2 shows the cyclic voltammogram (CV) heat map constructed from the data of 56 CNEs. These CVs were collected in 1x PBS with 1 mM redox mediator Ru $(NH_3)^{6+}$ using a potentiostat (CHI760D, CH Instruments, Inc., USA). The shape of the CV curves is sigmoidal. The diffusion-limited current i_d of the CV was used to evaluate the CNE size and effective surface area[1]. The obtained CNE effective surface area ranged between 0.1 – 3.9 μm^2 with the average value at 0.49 μm^2 as shown in Figure 2.2c.

2.1.5: Estimation of the Nanopore Surface Charge

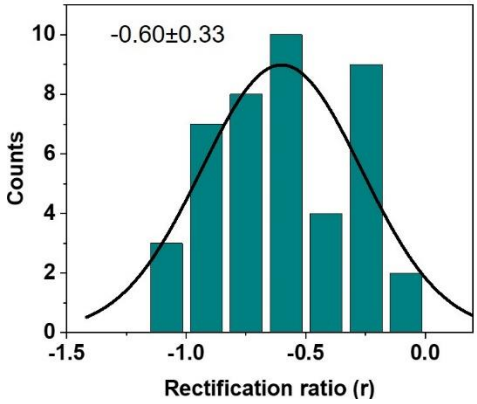

Figure 2.3: The histogram of rectification ratio (r) after CNE fabrication. The solid line is Gaussian fit to the histograms. The mean value is −0.60 ± 0.33 after GNE fabrication.

The magnitude and polarity of the nanopore surface charge determine the motion of the approaching or translocating single entities. To obtain a statistically large number of single nanoparticle events, it is crucial to quantify the nanopore surface charge. I used the previously reported method[1] where the asymmetric IV curves resulted from the IV measurements were used to estimate the surface charge of the nanopipette inner wall. The

assymetric IV curves are the result of the intrinsic negative charge on the nanopipette surface and the narrow conical shaped geometry of the nanopipette tip. These asymmetric IV curves were used to predict the surface charge density of the nanopore assuming the half cone angle of the nanopipette apex is fixed. The asymmetricity of the IV curves are obtained using the relation $r = log_{10}|I_+/I_-|$,[2] where r is called rectification ratio. The nanopipettes with larger negative r values (e.g., -1.0) are more negatively charged than the nanopipettes with small negative r values (e.g., -0.2). After the fabrication of CNE, the magnitude of the rectification ratio r was reduced to -0.60 ± 0.33 which is ~15% less than before CNE fabrication.

2.1.6: Zeta Potential Measurements of Nanoparticles Using Dynamic Light Scattering (DLS)

Malvern Zetasizer was used to measure the Zeta potential of the particles. For 60 nm and 120 nm PS NPs, zeta potential measurements were conducted in 25 mM and 50 mM PBS and for 26 nm PS NP, the measurements were performed in 10 mM and 25 mM PBS. At least five measurements were done for each PBS concentration. The average value of the results of five measurements was used as the zeta potential value of the nanoparticle at one PBS concentration. The zeta potential obtained for 26 nm NPs at 10 mM and 25 mM PBS was -56.66 mV and -44.6 mV, respectively. The zeta potential obtained for 60 nm NPs at 25 mM and 50 mM PBS was -57.98 mV and -46.12 mV, respectively. Similarly, for 120 nm NP, the zeta potential was -66.84 mV and -57.26 mV in 25 mM and 50 mM PBS, respectively.

The measured zeta potential is at the slipping plane of the NP. At low salt concentration, we can ignore the stern layer. The slipping plane thickness x_{SP} of the NP can be calculated with the following formula:[3]

$$\chi_{sp} = \frac{ln\frac{\zeta_1}{\zeta_2}}{(\frac{1}{\delta_2}-\frac{1}{\delta_1})} \tag{2.1}$$

where ζ_1 and ζ_2 are the zeta potentials, and δ_2 and $\delta_1$are the Debye lengths of the 25mM and 50 mM PBS solutions for 60 nm and 120 nm beads and 10mM and 25mM PBS solutions for 26 nm bead. For the 60 nm bead, NPs used in the present experiment, ζ_1 = -58 mV, ζ_2 = -46 mV, δ_1= 1.79 nm and δ_1= 1.27 nm for 25 mM and 50 mM PBS solutions. The slipping plane thickness was estimated to be ~1.0 nm. Using this slipping plane thickness, the GNP surface potential V_0 was calculated with the following formula:

$$V_0 = V_{sp}e^{\chi_{sp}/\delta} \tag{2.2}$$

where V_{sp} is the potential of GNP at the slipping plane or the measured zeta potential. We first calculated the slipping plane thickness(χ_{sp}), which was estimated to be ~1.0 nm. The 60 nm PS NP measured surface potential was estimated to be -101 mV. Finally, using the Grahame equation,

$$\sigma = 2\epsilon_r\varepsilon_0\kappa\left(\frac{RT}{zF}\right)[\sinh\left(\frac{zF\zeta}{2RT}\right) + \frac{2}{\kappa a}\tanh\left(\frac{zF\zeta}{4RT}\right) \tag{2.3}$$

Where ϵ_r and ϵ_r are permittivity of medium and air respectively. $1/\kappa$ is Debye length, R is gas constant, *T* is the temperature in Kelvin, *F* is Faraday's constant, a is the radius of nanoparticle, ζ is the measured surface zeta potential and *z* is the number of charges on a functional group.

As shown above the corresponding surface charge density σ of 60 nm PS NPs in 10 mM PBS was calculated to be -73 mC/m^2. Similarly, surface charge densities of 120 nm and 26 nm PS NPs were estimated as -67 mC/m^2 and -37 mC/m^2, respectively.

2.1.7: Electrical Measurements

The same electrolyte was used inside (*i. e.,* nanopore barrel) and outside (*i. e.,* bath solution). An Ag/AgCl electrode (0.2 mm diameter) was introduced from the back of the nanopore barrel filled with electrolyte. A copper wire coated with silver paint was inserted into the nanoelectrode barrel of the pipette to make secure contact with the CNE. The fabricated nanopore-nanoelectrode nanopipette was characterized using I–V and CV (Cyclic Voltammetry) measurements (see section 2.2). The ionic current-time (*i*-*t*) and potential-time (*V*-*t*) traces were recorded using the experimental setup shown in Figure 2.4. The setup was housed inside a Faraday cage on an air floating optical table to reduce electrical and mechanical noise. One Ag/AgCl wire electrode was placed inside the nanopipette and another one was placed in the bath. The bath electrode always remained grounded. The *i*-*t* traces were collected at various voltages using Axon 200B (Molecular Devices Inc., CA) in voltage-clamp mode. A home-built battery-powered high input impedance differential amplifier measured the potential change at the CNE. A digital oscilloscope (Yokogawa DL850 scopecorder) was used to record current and potential traces with a sampling rate of 50 kHz. The potential data noise at high frequency is considerably smaller than the current data, and thus, the low-pass filter bandwidth is 5 kHz for current and 40 kHz for potential. All the measurements were done at room temperature.

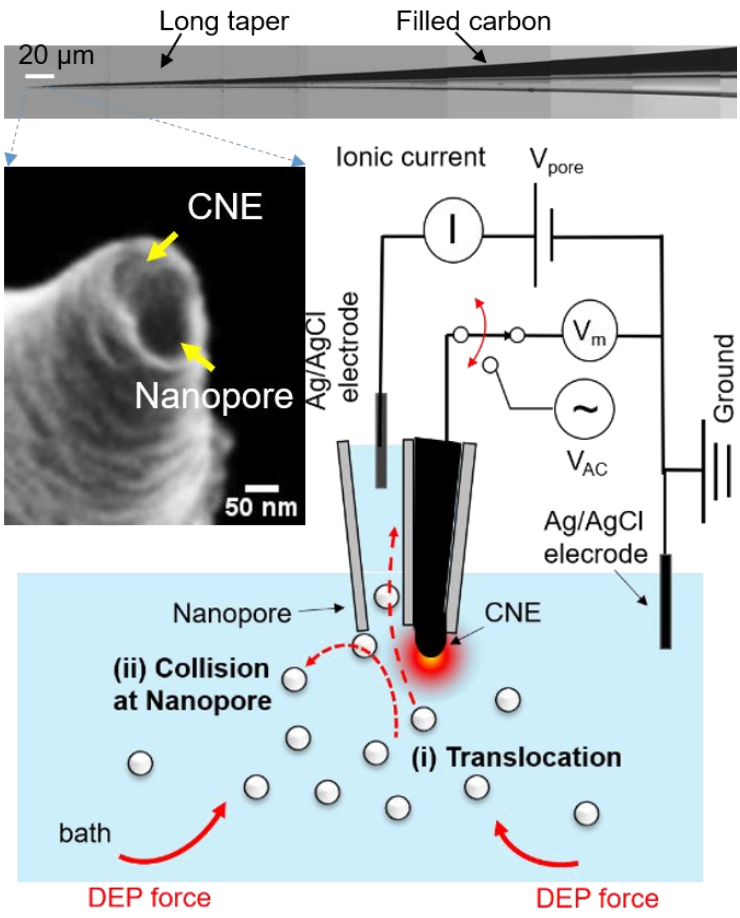

Figure 2.4: Experimental setup of using nanopore-nanoelectrode nanopipette to probe the dynamic NP motion in solution. Top inset: bright-field optical microscope image (stitched by 8 images) to show the long taper of the fabricated dual-barrel nanopipette. Left inset: SEM image of the nanopipette tip. The bath solution (10 mM PBS) is grounded and V_{pore} is the bias applied across the nanopore barrel filled with the same solution as the bath. A high impedance differential amplifier connected to the CNE is used to measure the potential (V_m) near the nanopipette tip, indicated by the blue shaded area. V_{AC} is applied for a short time to preconcentrate the NPs near the nanopipette apex through the AC DEP force. Two types of single NP events are illustrated: (i) translocation through the nanopore, and type (ii) collision of NPs at the nanopore.

2.1.8: Characteristics of the nanopipettes used in the experiment

The characteristics of the nanopore-CNE nanopipettes used in the study are shown below.

The IV and CV curves in Figure 2.5a and b were used to estimate the nanopore diameter and CNE area. The table in Figure 2.5c presents the estimated values derived from the

analytical equations. The area of the CNE can be converted to the diameter by assuming its shape as a hemisphere.

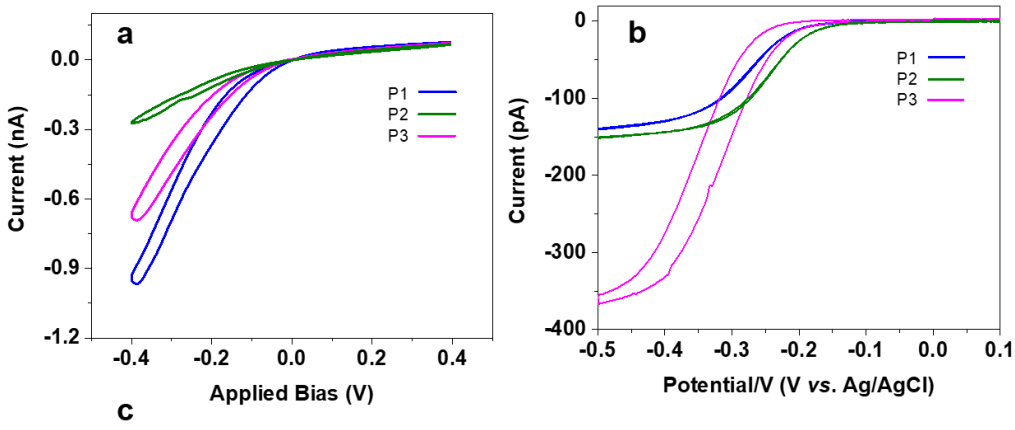

c

Nanopipette	Diameter (nm)	Effective CNE area (μm^2)
P1	71 ± 7	0.53 ± 0.04
P2	45 ± 4	0.56 ± 0.04
P3	59 ± 6	3.43 ± 0.24

Figure 2.5: The IV (a) and CV (b) characteristics of 3 nanopipettes mentioned in the main text. (c) A table summarized the nanopore diameter and effective CNE surface area of all three nanopipettes. The error in the CNE effective area is mainly as a result of its geometry. Assuming the hemispherical geometry of the protruded nanoelectrode, the geometry factor (m) of 1 is used for CNE effective area estimation. 'm' changes slightly (< 10 %) for other geometries.

2.1.9: Di-electrophoretic (DEP) Trapping

For the DEP experiments, a 2 MHz frequency AC voltage with 20 Volts peak to peak amplitude was applied using a Function generator (DS 340, Stanford Research System). Alternating Current (AC) voltage was applied between the CNE and a circular-ring shaped (~0.5 cm diameter) platinum wire electrode in the bath. The detailed force calculation on a single 60 nm PS NP under the AC DEP is estimated in section 2.3.3.

2.1.10: Noise Analysis of Ionic Current and Potential Measurements

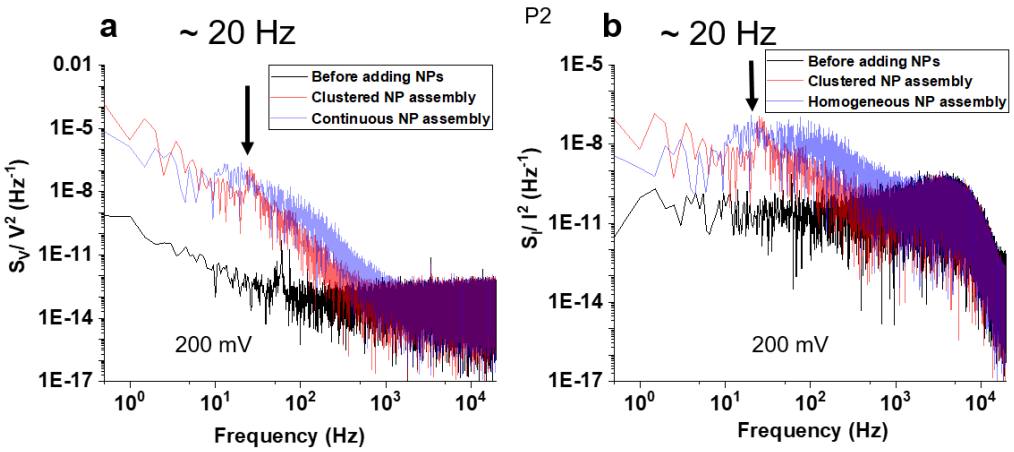

Figure 2.6: The normalized noise power spectra for potential (a) and ionic current (b) of a 2 second time trace from nanopipettes P3 at an applied bias V_b = 200 mV in 10 mM PBS. The black-colored noise spectra are recorded before the accumulation of 60 nm PS NPs. The Red and blue colored noise spectra are recorded after the accumulation of 60 nm PS NPs. The black arrow indicates the NP translocation frequency, which is close to 20 Hz. The sampling rate is 50 kS/s for both measurements and the bandwidth is 5 kHz for current and 40 kHz for potential. The 60 nm NP concentration is 1 pM.

We used a battery-powered high impedance voltage meter to record potential so that the bandwidth for potential measurement can be much larger than the current measurement. We used 5 kHz and 40 kHz low-pass filter bandwidth for current and potential measurements respectively. We analyzed the current and potential noise power spectrum in our measurements. The noise power spectrum density (PSD) S(*f*) is obtained by performing Fast Fourier Transformations (FFT) on a current or potential time trace (2 seconds) at 0.2V. Figure 2.6 (a) and (b) show the normalized PSDs of current (S_I/I^2) and potential (S_V/V^2) for P3 before adding PS NPs, during clustered and homogeneous PS NP assembly respectively. It is observed that at high frequency (>100 Hz) the noise of potential is much smaller than that of current. The potential noise spectra display characteristic 1/*f* noise at low frequency (<100 Hz). The potential noise spectral density distribution flattens

out at higher frequency with reduced magnitude. In contrast, the ionic current noise spectra show capacitance noise, which increases with the frequency. The noise analysis suggests that the analysis of the PSD helps us to understand the nanoparticle assembling dynamics in solution in real-time. When the clustered NPs assembly forms near the vicinity of the CNE, the noise spectrum broadens at a lower frequency with a peak at 20 Hz and when the assembly becomes homogeneous, the spectrum broadens further without the peak at 20 Hz.

2.1.11: Threshold Detection Scheme for Nanopore Collision Events

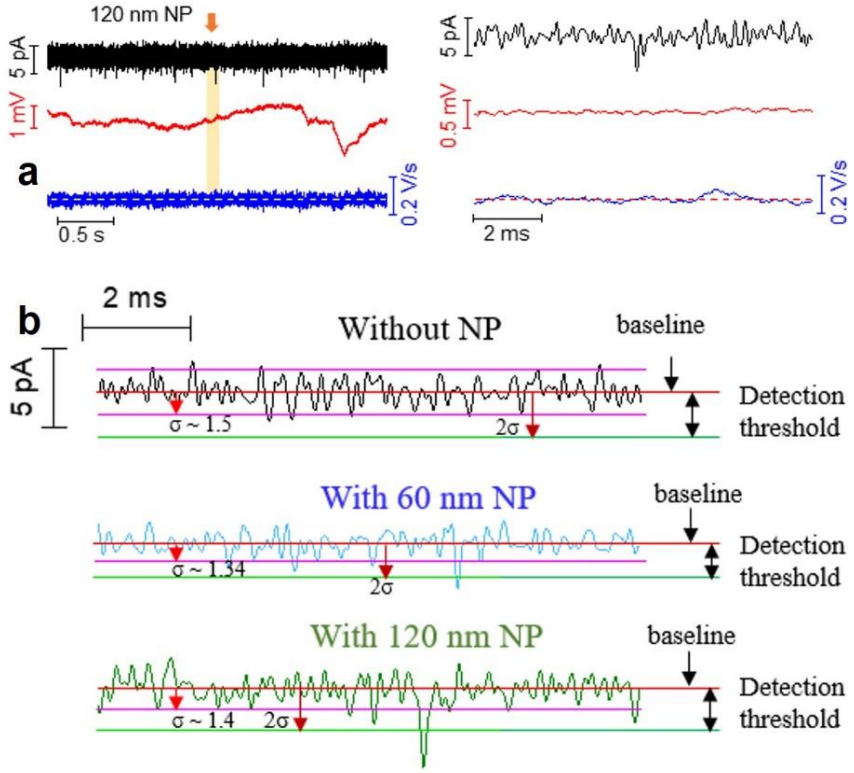

Figure 2. 7: (a) A typical time trace of current (black color), potential (red color) and the first derivative of potential (blue color) show small current spikes as a result of the collision of 120 nm NPs on the nanopore circumference of P1 at V_{pore} = 200 mV. The concentration of 120 nm PS NP was 100 pM in 10 mM PBS. The zoom-in of a current spike is shown on the right side. Slow and small changes are observed in the potential trace but no potential step can be observed at the same time with the current spike in the zoom-in. (b) Noise level comparison of current time trace without NPs, with 60 nm NPs, and with 120 nm NPs, at 200 mV bias. 10 ms time window is used to generate a baseline histogram and calculate standard deviation σ.

The collision of the nanoparticle at the circumference of the nanopore of the multi-functional nanopipette results in small current spikes but no potential change, Figure 2.7. These small spikes can be detected by using a threshold of 3 pA (~2σ of the baseline current). Where σ is the standard deviation. The magnitudes of these small spikes are similar for both 26 nm and 60 nm NPs but become slightly bigger (~ 4 pA) for 120 nm NPs. Because these spikes are typically shorter than 1 ms, a moving average window of 0.1 ms was used for these current time traces before analysis.

2.1.12: Data Analysis

The data were analyzed by using customized Labview programs and Originpro 2015. Moving average smoothing method with a 0.2 ms time window is typically applied to the current and potential results before statistical analysis. The dV/dt curves were smoothed by the moving average method using a 2 ms time window if not mentioned otherwise. The current spikes were detected by the threshold detection method.[4]

2.2: Differentiation of Metallic and Dielectric Nanoparticles in Solution *via* NP-CNE Collision Events

This section provides the methods used to accomplish the research project described in Chapter 4. The following subsections provide the descriptions of characteristics of the nanopipettes used in the study, hybrid AC-DC DEP method, theoretical estimation of the DEP forces for GNP and PSNP and darkfield microscopy, and data analysis methods.

2.2.1: Fabrication and Characterization of the Nanopipette

The details on the fabrication and characterization of the nanopipette are presented in section 2.1. The table below presents the characteristics of the nanopipettes used in the study.

Table 2. 1: The nanopore diameter and the effective CNE surface area of 7 nanopipettes.

Nanopipette	CNE Area (μm^2) [a]	Nanopore diameter (nm)[b]	Measurements
P1	0.020 ± 0.001	11 ± 1	Mixture
P2	0.13 ± 0.01	70 ± 6	60 nm PS NP
P3	0.44 ± 0.03	18 ± 2	10 nm GNP
P4	0.08 ± 0.01	55 ± 5	40 nm GNP
P5	0.57 ± 0.04	60 ± 5	60 PS NP
P6	0.68 ± 0.05	38 ± 3	26 PS NP
P7	1.07 ± 0.06	49 ± 4	60 nm PS NP

[a]The error in the CNE effective area is mainly as the result of uncertainly of geometry. [b]The error in the nanopore diameter is calculated using the uncertainty of the nanopipette geometry (half cone angle).

2.2.2: Electrical Measurements

The fabrication and characterization methods of the nanopore-CNE nanopipette have been reported previously and described briefly in section 2.2. The ionic current-time (*i*-*t*) and potential-time (*V*-*t*) traces are recorded using the experimental setup illustrated in Figure 2.4. The rest of the measurement procedures are described in section 2.2. Axopatch 200B amplifier (Molecular Devices Inc., CA) is used in voltage-clamp mode to measure the current. A home-built high input impedance differential amplifier is used to measure the

open-circuit potential V of the CNE. An oscilloscope (Yokogawa DL850) is used to record the data with a sampling rate of 50 kHz. The bandwidth of the low-pass filter is 5 kHz for current and 40 kHz for potential signals. All the measurements are performed at room temperature. The GNP and PS NP concentrations in the bath solution (10 mM PBS) are typically 10 pM and 100 pM, respectively, if not mentioned otherwise.

2.2.3: Dielectrophoresis (DEP) Theory

Dielectrophoresis is referred to as the motion of a particle in a nonuniform electric field that results from the interaction of a polarizable particle in medium with the spatially nonuniform electric field. The direction and magnitude of DEP depend on the particle polarizability relative to the suspending medium, particle size, and the gradient of the electric field. For a spherical particle of radius R, the DEP force is expressed as

$$< \boldsymbol{F_{DEP}} > = 2\pi\varepsilon_m R^3 Re[f_{CM}(\omega)]^* \boldsymbol{\nabla}|\boldsymbol{E_{rms}}|^2 \quad (2.4)$$

where ε_m is an absolute permittivity of the surrounding medium, R is the particle radius, E_{rms} is the amplitude of the electric field, ∇ is a gradient operator and $[f_{CM}(\omega)]$* is the Clausius-Mossotti factor related to effective polarizability of the particle and medium which is defined as

$$[f_{CM}(\omega)] * = \frac{\varepsilon_p^* - \varepsilon_m^*}{\varepsilon_p^* + 2\varepsilon_m^*} \text{ OR } [f_{CM}(\omega)]^* = \frac{\sigma_p^* - \sigma_m^*}{\sigma_p^* + \sigma_m^*} \quad (2.5)$$

Where $\varepsilon_p^* and\ \sigma_p^*$ are the complex permittivity and complex conductivity, $\omega = 2\pi f$; f denotes the frequency of the AC field.

For positive DEP (*i.e.*, $Re[f_{CM}(\omega)]^* > 0$ or $\varepsilon_p > \varepsilon_m$), particles are attracted to electric field maxima and for negative DEP (*i.e.*, $Re[f_{CM}(\omega)]^* < 0$ or $\varepsilon_p < \varepsilon_m$) particles are repelled from electric field maxima.

For a Polystyrene particle with radius R, its electrical conductivity is the sum of bulk conductivity ($\sigma_{p,bulk}$) and the particle surface conductance *Ks* and is expressed as

$$\sigma_p = \sigma_{p,bulk} + \frac{2K_s}{R} \tag{2.6}$$

The variable $\sigma_{p,bulk}$ is the bulk conductivity of insulating polystyrene spheres and is very small compared to the second term and thus can be ignored.[5] The total particle conductivity σ_p is dominated by K_S. The *Ks* of polystyrene particle is the sum of two surface conductances of the double layer: one associated with the stern layer charge (K_{Stern}) which is independent of medium conductivity, and the other as a result of the diffuse layer charge (K_{diff}) which is inversely proportional to the medium conductivity.[6, 7] The medium conductivity in our experiment is 0.13 S/m. At 0.13 S/m medium conductivity, K_{Stern} and K_{diff} have similar values and both contribute to the total particle conductivity. From the previous report,[7-9] we use the total surface conductance value *Ks*=2.2 nS. From equation (3), we estimated $\sigma_p \sim 0.15$ for 60 nm PS NP and $\sigma_p \sim 0.34$ for 26 nm NP.

Two dimensional (2D) axis-symmetry electrostatic numerical simulation[1, 10] give us the electric field intensity gradient $|\nabla|\boldsymbol{E}_{rms}|^2|$ = 10^{23} V^2/m^3.

For 60 nm and 26 nm PS NPs in 10 mM PBS

$\varepsilon_m = 80\varepsilon_o \quad \sigma_m = 0.13\frac{S}{m}, \quad \varepsilon_0 = 8.854 * 10^{-12}, \varepsilon_p = 2.5\varepsilon_o, \sigma_p^{26} = 0.35\ \frac{S}{m}, \sigma_p^{60} = 0.15\ \frac{S}{m}, R_{26} = 13\ nm, R_{60} = 30\ nm\ and\ f = 2MHz$

Using equation (2), CM factor is ~0.02 for 60 nm PS NP and ~0.35 for 26 nm NP. From equation (1), the corresponding positive DEP force for 60 nm PS NP is ~0.25 nN and for 26 nm PS NP is ~0.33 nN which are much larger than the thermal fluctuation force (*i.e.*, ~ 9.92 fN).

Similarly, for 40 nm GNPs in 10 mM PBS,

$$\varepsilon_{m=}80\varepsilon_o \quad \sigma_{m=}\ 0.13\frac{S}{m}, \quad \varepsilon_0 = 8.854 * 10^{-12}, \varepsilon_p = 2.5\varepsilon_o, \sigma_p = \frac{4.5 * 10^7 S}{m}, R = 20\ nm\ and\ f = 2MHz$$

CM factor is ~1. The corresponding DEP force for 40 nm GNP is ~3.47 nN. Thus, the AC DEP force on 40 nm GNP is ~14 times stronger than on 60 nm PS NP and is ~10 times stronger than on 26 nm PS NP.

It should be noted that the estimations above are derived from symmetric planer electrode geometry. In our experimental setup, the high asymmetry between the nanometer-sized CNE and the circular platinum (Pt) electrode contribute to the efficient NP trapping.

2.2.4: Di-electrophoretic Enrichment of Nanoparticles

We apply a DC/AC DEP hybrid method to accumulate NPs near the CNE [38]. A dielectric object in a dielectric medium experiences a large DEP force when exposed to a spatially non-uniform electric field. Because of the tip geometry, the DC nanopore bias (V_{pore}) can also generate DC DEP force on the NPs near the nanopipette apex. However,

the most effective means to preconcentrate the NPs near the nanopipette apex is to apply an AC bias to the CNE. A relatively big V_{pore} (~0.8 V) is applied initially for about 10–30 min, which slowly gathering NPs near the nanopipette tip. In the next step, an AC voltage of 20 V peak-to-peak magnitude and 2 MHz frequency is applied to the CNE for 1–3 min using a function generator (Stanford Research Systems DS340). The CNE is at the center of a grounded circular (r = 0.5 mm) platinum (Pt) wire electrode. The switch in Figure 4.1a is used to apply the AC DEP trapping (at position 2). After AC DEP trapping, the switch is changed to position 1 to record signals. As shown in our calculations (see section 2.2.3 for detail), both PS NP and GNP experience positive DEP forces but the GNP with higher polarizability is exerted a bigger DEP force.

2.2.5: Dark Field Microscopy (DFM)

Figure 2.8a shows the schematic of the Dark Field Microscopy (DFM) setup. The DFM images shown in Figure 2.8b were captured by a CCD camera (Point Grey Grasshopper 3) on an inverted optical microscope (Nikon Eclipse Ti-U) equipped with a dark-field condenser (Nikon, Ti-DF, NA ~0.8-0.95) and a 40x objective lens (NA = 0.6). A CCD camera (Point Grey Grasshopper 3) was used to capture the dark-field images. 100 µl of the NPs suspension in 10 mM PBS is placed at the liquid cell.

2.2.6. Data Analysis

The data were analyzed using a custom LabVIEW program and OriginPro 2018. The current and potential results are smoothed by a moving average method with 0.1 ms and 0.2 ms time windows, respectively. The dV/dt curves are smoothed by the moving average method using a 3 ms time window if not mentioned otherwise.

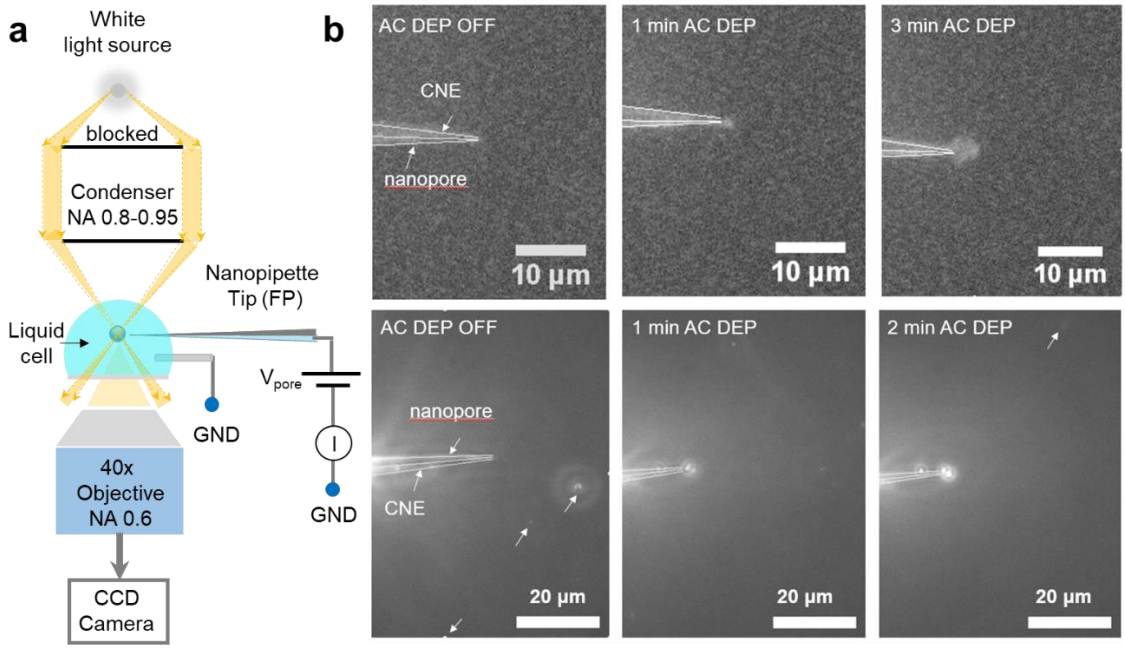

Figure 2. 8 (a) Schematic of the Dark-Field microscope (DFM) setup. (b) The DFM images of 40 nm GNPs (first row), 60 nm PS NPs (second row) accumulation near the nanopipette apex after DEP trapping. The bright blob at the pipette apex is as a result of the NPs accumulation. The blob size varies from a minimum of 1 µm to a maximum of 4 µm. After DEP trapping NPs are more aligned towards the CNE side of the nanopore-CNE nanopipette. The small white arrows denote the NPs in the bath solution. Interestingly, DEP trapping is highly efficient for the smaller CNE diameter (*i.e.*, 40 nm-150 nm). The nanopipettes shown above have an approximate CNE diameter of 60 nm. The solid white lines represent an eye guide to see an edge of the nanopipette.

2.3: Surface Charge Enhancement of Magneto-electric Nanoparticles Under AC Magnetic Field

2.3.1: Fabrication and Characterization of the Nanopipette

The details on the fabrication and characterization of the nanopipette are presented in section 2.1. The table below presents the characteristics of the nanopipettes used in the study. The diameter of the nanopore ranges from 40-100 nm. The CNE effective surface area ranges between 0.02-1.02 µm^2 with a mean value of 0.21 µm^2. The detailed information of each nanopipette is summarized in the table below.

Table 2. 2: The nanopore diameter and the effective CNE surface area of 8 nanopipettes.

Nanopipette	CNE Area (μm^2) [a]	CNE radius (nm)	Nanopore diameter (nm)[b]	Measurements
P1	0.378 ± 0.026	241 ± 64	96 ± 9	MENP
P2	0.091 ± 0.006	120 ± 31	95 ± 9	MNP
P3	0.078 ± 0.005	111 ± 29	58 ± 5	MENP
P4	0.488 ± 0.034	278 ± 73	71 ± 6	MNP
P5	0.080 ± 0.005	113 ± 29	60 ± 5	MENP
P6	0.094 ± 0.007	120 ± 37	138 ± 13	MNP
P7*	0.344 ± 0.024	234 ± 61	85 ± 8	MENP
P8	0.017 ± 0.001	89 ± 24	44 ± 4	MENP

[a]The error in the CNE effective area is mainly as a result of the uncertainly of geometry. [b] The error in the nanopore diameter is calculated considering the uncertainty of the nanopipette geometry (half cone angle). *Salinized nanopipette.

2.3.2: Electrical Measurements

The fabrication and characterization methods of the nanopore-CNE nanopipette have been reported in our previously published research.[1] In brief, the ionic current-time (*i-t*) and potential-time (*V-t*) traces are recorded using the experimental setup as illustrated in Figure 1a. The setup is housed in double Faraday cages on an air floating optical table to reduce electrical and mechanical noise. We used homemade Ag/AgCl electrodes and an Axopatch 200B amplifier (Molecular Devices Inc., CA) in voltage-clamp mode to measure the ionic current through the nanopore. A customized, battery-powered, high input impedance differential amplifier was used to measure the OCP of the CNE. A digital oscilloscope (Yokogawa DL850 Scopecorder) was used to record the current and potential traces with a sampling rate of 50 kHz. The bandwidth of the low-pass filter was 5 kHz for current and

40 kHz for potential signals. All experiments and measurements were performed at room temperature. The collision experiments were performed in 10 mM PBS. The NPs concentration in the bath solution was typically 1 nM if not mentioned otherwise.

2.3.3: Dark Field Microscopy (DFM)

The dark-field microscopy (DFM) images were captured using an inverted optical microscope (Nikon Eclipse Ti-U) equipped with a dark-field condenser (Nikon, Ti-DF, NA ~0.8 - 0.95) and a 40x objective lens (Nikon CFI Super Plan Fluor ELWD, NA = 0.6). (See Figure 2.8 for the detailed schematic setup). A CCD camera (Point Grey Grasshopper 3) was used to capture the dark-field images. 100 µl of the NPs suspension in 10 mM PBS was placed at the liquid cell. The liquid cell was kept at the center of the solenoid. The nanopipette tip was placed horizontally within the liquid cell and the motion of the MENPs was monitored with and without an AC B-field. As a control experiment, the DF video of the ~50 nm MNP is also recorded. The detailed DFM setup is presented in section 2.3.3.

2.3.4: Estimation of Net Force Acting on the Single MENP and MNP Under AC Magnetic Field.

There are three major forces involved in our electrical measurement setup. (i) Electrical force ($\mathbf{F_e}$) as a result of the charge of the nanoparticle. (ii) Magnetic force ($\mathbf{F_m}$) as a result of the AC B-field and (iii) Stoke's drag force ($\mathbf{F_d}$) as a result of the viscosity of the medium. Besides, there is also torque associated with the magnetic field and fluid friction. The parameters required to estimate all these forces are presented in the table below

Table 2. 3: MENP and MNP parameters used in the calculation

Parameters	Diameter d (m)	Surface charge density σ [a] (C/m^2)	Electric Field E (V/m)[b]	Viscosity of water η (kg/m.s)	Magnetic moment $m=M\rho V$ (Am^2)	Specific magnetization (M) (Am^2/kg)	Density ρ (kg/m^3)	Magnetic Field B (T)
MENP	25×10^{-9}	23×10^{-3}	10^7	1.0×10^{-3}	1.5×10^{-18}	34[c]	5299[c]	6×10^{-3}
MNP	50×10^{-9}	16×10^{-3}	10^7	1.0×10^{-3}	9.5×10^{-17}	80[d]	5400[d]	6×10^{-3}

Note: [a]The surface charge densities of MENP and MNP are estimated from zeta potential measurements. [b]The E at the nanopipette apex is adopted from the simulation of previous work.[1] [c]The density and specific magnetization of MENP are taken from previous work.[11-13] [d]The density and specific magnetization of MNP are taken from the previous report.[13]

Table 2. 4: Force (F), torque (τ) and MENP/MNP rotational parameters calculations

Electric force (F_e)	$F_e = q*E = \frac{\pi}{4}\sigma d^2 E$	~10^{-11} N
Magnetic Force (F_m)	$F_m = (m.\nabla)B = \rho * V(M.\nabla)B$	0 N for uniform B-field
Magnetic torque (τ_m)[14, 15]	$\tau_m = m \times B = MV * B$ $\tau_m = \frac{V\chi^2 B^2 Sin(2\theta)}{2(2+\chi)}$ $2\theta = 15^0$ (assume) and $\chi = 2\ for\ MENP$ and 5 for MNP[14]	MENP: 0.01 $pN\ nm$ MNP: 0.08 $pN\ nm$ Where θ is the angle between m and B and χ is the magnetic susceptibility.
Frictional torque (τ_f)[15, 16]	$\tau_f = 8\pi\eta r^3\omega$;	30 nm MENP: $7.55 \times 10^{-26}\omega$ Nm 50 nm MNP: $3.49 \times 10^{-25}\ \omega$ Nm
Angular velocity (ω)	$\omega = \frac{V\chi B^2 Sin(2\theta)}{2\mu_0(2+\chi)8\pi\eta r^3}$ Where μ_0 is the magnetic permeability of free space	30 nm MENP: 433 rad/s 50 nm MNP: 1032 rad/s
Tangential velocity (v)	$v = \omega r$ Where ω is the angular frequency	30 nm MENP: 6.5 μm/s 50 nm MNP: 25.8 μm/s
Frequency of rotation (f)	$f = \omega/2\pi$	30 nm MENP: 69 Hz 50 nm MNP: 164 Hz
Stoke's drag Force (F_d)	$F_d = 3\pi * \eta * d * v$; v~10^{-6} m/s	~10^{-15} N

The force involved in the DFM experiment is F_e. The drag force is comparable to the force caused by Brownian motion. Since the externally applied magnetic field is uniform, there is no magnetic field gradient and thus no magnetic force. However, there is a torque on the particles because the uniform B-field causes rotational motion. We estimated that the torque experienced by MENP in presence of 6 mT AC B-field is an order of magnitude smaller than that of the MNP. As particles rotate, they experience frictional torque. In Newtonian fluids, the frictional torque (τ_f) for rotation can be expressed as $8\pi\eta r^3\omega$, where ω is the angular velocity of the nanoparticle, and η is the fluid viscosity. In the inertia-less limit, the frictional torque balances with magnetic torque. This balance allows us to estimate the terminal angular velocity of the magnetic nanoparticle.

2.3.5: Theoretical Estimation of Electric Potential Change on a MENP Surface

Assuming the simplest case where CFO core and BTO shell interface is tightly connected such that any stress from the CFO core completely transfers to the BTO. The solenoid generates the magnetic field along the *z*-axis. In a dielectric ceramic material like BTO without the center of symmetry, an electric polarization (*P*) is induced as a result of external mechanical stress.

$$P = d \times \sigma \ (direct\ effect) \tag{2.7}$$

$$\varepsilon = d \times E \ (converse\ effect) \tag{2.8}$$

Where *d* is the piezoelectric coefficient (m/V) and ε is the strain produced by stress.

Assuming the field and the displacement along the *z*-direction, the value of *d* for BTO is 200 pC/N. Or pm/V.[17] The strain ($\varepsilon = \Delta l/l$) produced in the BTO shell can be

calculated by taking the ratio of change in dimension to the original dimension. The maximum change in dimension for BTO under 60 Hz of AC frequency and 50 Oe field is ~-43 ppm.[18] Note that 43 ppm is 0.0043%. Thus, Δl is 0.0043% of ~$l = 6\ nm$. The AC magnetic field pulse strength and frequency in our experiment is ~60 Oe and 1 kHz.

Thus, using $\varepsilon = \Delta l/l$ and $E = V/l$ in equation (2) gives

$$\Delta l = d * V \tag{2.9}$$

WhereΔl = -0.00026 nm; $d = 200$ pm/V;

Thus, potential change as a result of AC B-filed induced magnetostriction can be approximated to be ~-1.30 mV. Thie potential change is an estimation of the local potential generated on the surface of a single MENP under AC B-field stimulation. The estimated value is in the same order of magnitude range compared with the experimentally observed potential amplitude difference (~0.63 mV from P1 and ~12.9 mV from P2).

2.3.6: Diffusion-limited Event Rates: Stokes-Einstein Relationship

The Stokes-Einstein relationship for the diffusion coefficient *D* of a spherical particle of radius *r* in a fluid of dynamic viscosity η at absolute temperature *T* (K) is given as

$$D = \frac{k_B T}{6\pi\eta r} \tag{2.10}$$

Where, $k_B = 1.3803 \times 10^{-23}$ J K^{-1} is a Boltzmann's constant. The viscosity of the water is $1.0 \times 10^{-3} Kg/ms$.

If the mass transfer to the hemispherical electrode is mainly as a result of the diffusive flux of biomolecules, the frequency of collision, f_{diff}, can be estimated using the following relation.

$$f_{diff} = 4DC_{NP}\, r_{CNE}\, N_A \tag{2.11}$$

Where D is the diffusion coefficient of the NPs, C_{NP} is the concentration of the NP in particles/m^3, r_{CNE} is the nanoelectrode radius and N_A is Avogadro's number. The nanoelectrodes of P1 and P6 are used in the calculation. The radii of P1 and P2 are 241±64 nm and 120±32 nm respectively. The experimental diffusion induced MENP-CNE collision event rate value at 0 mV is 0.46 /s. The theoretical and experimental values (at 400 mV) of the diffusion induced NP collision frequency, f_{diff} $(events/s)$ are tabulated below.

Table 2. 5: The MENP-CNE and MNP-CNE collision frequency (/s) calculated using theory and experimental results.

	Theory		Experiment V_{pore} = 0 mV		Experiment V_{pore}= 400 mV	
NP (probe)	$D \times 10^{-7}$ (cm^2/s)	f_{diff} $(/s)$	f_{diff}@ 0 Oe	f_{diff} @ 60 Oe	f_{diff}@ 0 Oe	f_{diff} @ 60 Oe
MENP (P1)	1.46	8.45	0.46	-	1.30	1.27
MNP (P6)	0.44	1.26	0.21	-	0.25	0.22
MENP (P8)	1.46	8.45	0.26	0.16	0.33	0.18

2.3.7: Salinization

The exterior of the nanopore-nanoelectrode nanopipette surface was modified *via* immersing the nanopipette tip (<5 mm) in a 2% *v/v* solution of 3-

cyanopropyldimethlychlorosilane in CH_3CN for 2 h. The nanopipette was then rinsed sequentially with acetonitrile (CH_3CN), ethanol (EtOH), and DI water followed by argon gas drying. The modified nanopipette was characterized using electrochemical measurements and used for the experiment.

2.3.8: AC B-field Stimulation

To enhance the throughput of single-MENP measurements, we apply AC B-field *via* a custom-built solenoid. An AC voltage of 20 Volts peak-to-peak (V_{pp}) magnitude at 1 kHz frequency (f_{ac}) was applied to the CNE using a Function generator (KEITHLEY 3390). The current in the solenoid was applied using a DC power supply (KEITHLEY 2230-30-1). The current in the solenoid coil was varied to adjust B-field intensity at the center of the solenoid. The heat produced in the coil was negligible (temperature difference varies from 23 to 26 ^oC) for measurement ~15 minutes. However, to avoid possible heating effects, the current in the coil was turned off for ~ 5 minutes after every 10 minutes of AC B-field stimulation. The magnetic field at the center of the coil was measured using a Gauss meter (Magsys Magnetometer).

2.4: A Multi-functional Nanopipette for Detection of Single Biomolecules in Aqueous Solution

The work integrates two single entity electrochemical methods (nanopore and nanoelectrode) in one nanopipette apex to simultaneously monitor the ionic current and surface potential changes at the nanopore and the nanoelectrode when a single protein translocates through the nanopore or collides with the nanoelectrode. The sections below present the methods employed to execute this research work.

2.4.1: Fabrication and Characterization of the Nanopipette

The details on the fabrication and characterization of the nanopipette are presented in section 2.1.

2.4.2: Electrical Measurements

The electrochemical measurements procedure is similar as described in the previous section 2.1.7

2.4.3: Finite Element Based Numerical Simulation

We used FEM simulation to solve coupled Poisson−Nernst−Planck (PNP) partial differential equations (see chapter1, equations 1.8 and 1.9). To simplify the simulation, a steady-state system was considered and fluidic flow term was not included. The AC/DC and chemical reaction engineering modules (COMSOL Multiphysics 5.2) were used for the FEM simulation. See Chapter 6 for a detailed description of the FEM simulation. The simulation results presented in Chapter 6 lays the foundation for the nanopipette optimization for protein detection.

2.5: Data Analysis

The data were analyzed by using customized Labview programs and Originpro 2018. Moving average smoothing method with a 0.2 ms time window is typically applied to the current and potential results before statistical analysis. The dV/dt curves were smoothed by the moving average method using a 2 ms time window if not mentioned otherwise.

2.6: References

1. Panday, N., et al., *Simultaneous Ionic Current and Potential Detection of Nanoparticles by a Multifunctional Nanopipette.* ACS Nano, 2016. **10**(12): p. 11237-11248.

2. Vilozny, B., et al., *Reversible Cation Response with a Protein-Modified Nanopipette.* Analytical Chemistry, 2011. **83**(16): p. 6121-6126.

3. Shan, X., et al., *Detection of Charges and Molecules with Self-Assembled Nano-Oscillators.* Nano Letters, 2014. **14**(7): p. 4151-4157.

4. Plesa, C. and C. Dekker, *Data analysis methods for solid-state nanopores.* Nanotechnology, 2015. **26**(8): p. 084003.

5. Hughes, M.P., H. Morgan, and M.F. Flynn, *The Dielectrophoretic Behavior of Submicron Latex Spheres: Influence of Surface Conductance.* Journal of Colloid and Interface Science, 1999. **220**(2): p. 454-457.

6. Kijlstra, J., H.P. van Leeuwen, and J. Lyklema, *Effects of surface conduction on the electrokinetic properties of colloids.* Journal of the Chemical Society, Faraday Transactions, 1992. **88**(23): p. 3441-3449.

7. Ermolina, I. and H. Morgan, *The electrokinetic properties of latex particles: comparison of electrophoresis and dielectrophoresis.* Journal of Colloid and Interface Science, 2005. **285**(1): p. 419-428.

8. Lewpiriyawong, N. and C. Yang, *AC-dielectrophoretic characterization and separation of submicron and micron particles using sidewall AgPDMS electrodes.* Biomicrofluidics, 2012. **6**(1): p. 012807.

9. Arnold, W.M., H.P. Schwan, and U. Zimmermann, *Surface conductance and other properties of latex particles measured by electrorotation.* The Journal of Physical Chemistry, 1987. **91**(19): p. 5093-5098.

10. Freedman, K.J., et al., *Nanopore sensing at ultra-low concentrations using single-molecule dielectrophoretic trapping.* Nature communications, 2016. **7**.

11. Kaushik, A., et al., *Investigation of ac-magnetic field stimulated nanoelectroporation of magneto-electric nano-drug-carrier inside CNS cells.* Scientific Reports, 2017. **7**: p. 45663.

12. Rafferty, A., T. Prescott, and D. Brabazon, *Sintering behaviour of cobalt ferrite ceramic*. Ceramics International, 2008. **34**(1): p. 15-21.

13. Golovin, Y.I., et al., *Theranostic multimodal potential of magnetic nanoparticles actuated by non-heating low frequency magnetic field in the new-generation nanomedicine.* Journal of Nanoparticle Research, 2017. **19**(2): p. 63.

14. Gabayno, J.L.F., et al., *Controlled manipulation of Fe3O4 nanoparticles in an oscillating magnetic field for fast ablation of microchannel occlusion.* Nanoscale, 2015. **7**(9): p. 3947-3953.

15. Moerland, C.P., L.J. van Ijzendoorn, and M.W.J. Prins, *Rotating magnetic particles for lab-on-chip applications – a comprehensive review.* Lab on a Chip, 2019. **19**(6): p. 919-933.

16. Janssen, X.J.A., et al., *Controlled torque on superparamagnetic beads for functional biosensors.* Biosensors and Bioelectronics, 2009. **24**(7): p. 1937-1941.

17. Dong, L., D.S. Stone, and R.S. Lakes, *Enhanced dielectric and piezoelectric properties of xBaZrO3-(1−x)BaTiO3 ceramics.* Journal of Applied Physics, 2012. **111**(8): p. 084107.

18. Betal, S., et al., *Magneto-elasto-electroporation (MEEP): In-vitro visualization and numerical characteristics.* Scientific Reports, 2016. **6**: p. 32019.

CHAPTER 3: PROBING DYNAMIC EVENTS OF DIELECTRIC NANOPARTICLES USING NANOELECTRODE-NANOPORE NANOPIPETTE

In Chapter 3, we demonstrate the use of a nanopore-nanoelectrode based method to study polystyrene (PS) NPs with various sizes, which were used as the model dielectric NPs. Furthermore, by utilizing dielectrophoretic (DEP) force applied through the nanoelectrode, we showed that PS NPs can be efficiently preconcentrated to form large assemblies outside the nanopipette tip, enabling high-throughput single NP analysis. The study further reveals that the interactions between NPs and between the NP and the nanopore surface affect the current and potential signals. We investigated the dynamic structures and motions of PS NPs inside the large assembly using the complementary and correlated the ionic current and potential signals from both the nanopore and the nanoelectrode. We also compared the difference in the dynamic events between polarizable metallic NPs and non-polarizable dielectric NPs during multi-NP structure formation and individual NP transport and translocation motions. The content presented here is the slightly modified version of my published peer-reviewed article.[1-3]

3.1 Introduction

Synthetic Nanoparticles (NPs) have been widely used in various fields, including energy, environmental, chemical and biomedical applications.[4-6] However, multiparameter analysis of NPs at the single NP level in ionic solution remains challenging and efficient and high-precision methods are still limited and at the early developing stage.[7, 8] In the last two decades, nanopore-based single-entity sensing techniques have been developed into powerful methods to study different properties of various nanoscale entities.[9-11] Utilizing the ionic current change induced by the NP translocation event, information of

target analyte, including number density, size, shape, charge, and even the dynamic orientation and motion speed during translocation can be obtained.[12-19] To further improve the sensitivity and selectivity of the ionic current detection based nanopore technique, as well as add new functionalities to it, it is of great interest to bring new sensing modules to the resistive-pulse based detection method.[20-24]

Previously, we have demonstrated how a new nanopore-nanoelectrode dual-barrel nanopipette based method can detect both the ionic current and potential change induced by the translocation of individual gold NPs (GNPs) through the nanopore.[25] The floating nanoelectrode detects the moving NP induced local potential change, which is mainly induced by the surface charge of the NP. Surface charge induced potential chnage is different from the capacitive signal, which is induced by the disturbance of the electrical double layer (EDL) near the electrode surface by NP collision events.[26-28] The capacitance change is difficult to detect when the NP size is smaller than 100 nm. The charge-based potential detection mechanism is also different from the NP collision-induced open circuit (mixed) potential change, which is related to the redox process.[23, 29] The addition of potential sensing capability to the ionic current based nanopore sensing method brings a valuable new perspective to the understanding of the dynamic events of individual NPs near the nanopipette tip. Because of the extended detection distance range of potential sensing by the carbon nanoelectrode (CNE), we can track the transport dynamics of single NP from the initial approaching motion towards the nanopore orifice using potential changes while no current changes can be probed. In addition to detecting single NP motion, rich information of the dynamic assembly process of a large number of NPs near the nanopore entrance can be revealed. With the gradual accumulation of GNPs near the

nanopore entrance, small GNP clusters with short pearl-chain structures are formed in the accumulated large GNP assembly, as a result of the strong polarization of GNP. These small multi-NP structures cannot be detected by using a conventional fluorescence microscope and limited information can be acquired if only ionic current changes are analyzed. The strong polarization of GNPs in a strong non-uniform electric field can significantly alter the local electric potential distribution and greatly enhance the potential detection sensitivity. Therefore, a question is raised on the sensitivity of potential method for the detection of dielectric NPs. It is also of fundamental interest to investigate the dynamic accumulation and small cluster formation of dielectric NPs (including nanoscale biological entities) suspended in solution under external forces[30] and understand the differences between metallic NPs and dielectric NPs in these dynamic events.

Here, we used a systematic approach to study non-polarizable negatively charged polystyrene (PS) NPs with three different sizes. Indeed, under the same conditions, the electric force exerted on the dielectric NPs is smaller than that on the metallic NPs, resulting in much fewer successful translocation events and much more collision events at the nanopore orifice. By analyzing the NP size effect on these individual NP translocation events, we consolidated our understanding of the current and potential sensing mechanism. Then, we took the advantage of the presence of the CNE at the nanopipette tip to generate a strong AC DEP force, which can efficiently concentrate tens of thousands of NPs near the nanopipette tip in a very short time, enabling high-throughput single NP analysis. The accumulation of NPs leads to the formation of large homogeneous NP domains and small inhomogeneous regions between the domains, which contain many small NP clusters. The structural differences between PS NP and GNP clusters have been identified. The structures

of small NP clusters and large NP assemblies also depend on the size and surface charge of NP, the interactions between NPs and the applied external forces. These detailed studies underscore the capability of the nanopore-nanoelectrode nanopipette based multimode detection method, expanding the research from investigating isolated single NP behavior to single/multi-NP events in a crowded environment.

3.2 Experimental Methods

The majority of the experimental methods used to accomplish the project are described in Chapter 2. Section 2.1 and its subsections provide an overview of multi-functional nanopipette fabrication and electrical/optical characterization. The electrical data collection and analysis, DEP methods are also presented in subsection 2.1. The reagents and solutions used in the project are described in the subsection below.

3.2.1 Reagents and Solutions

Carboxyl-functionalized (26nm, 60nm and 120nm diameter) PS NPs were bought from Bangs Laboratories *Inc.* The surface charge density of each bead particle was estimated from the parking area provided by the manufacturer. Furthermore, Zeta potential measurements were also performed, using the dynamic light scattering method (Malvern Zetasizer). Phosphate Buffer Saline (PBS, for pH 7.3-7.5) powder was purchased from Fisher Scientific. For 10 mM PBS, the NaCl concentration was about 9.1 mM and the phosphate concentration was about 0.8 mM. The ionic strength of the 10 mM PBS solution is approximately 11.4 mM. All other chemicals were purchased from Sigma Aldrich. Finally, all of the aqueous solutions were prepared using Deionized Water (~18 MΩ) (Ultra

Purelab system, ELGA/Siemens). All the chemicals were purchased with ACS grade and used as it is without further purification.

3.3 Results and Discussion

3.3.1 Experimental Setup for Probing Dynamic Events of Dielectric PS NPs

The nanopore-nanoelectrode nanopipette based experimental setup is illustrated in Figure 3.1. The optical microscope image shows the side view of a two-barrel nanopipette after filling one barrel with pyrolytic carbon (see the Methods section 2.1.3). The half-cone angle of the nanopore is 5.5˚±0.5˚ and the taper of the nanopipette is quite long, as revealed by the stitched optical microscope image. The CNE and nanopore at the apex of the dual-barrel nanopipette are shown in the scanning electron microscopy (SEM) image. The fabricated nanopore diameter ranges from 50 to 90 nm with a mean diameter of 73 nm (see Method section 2.1.4). The average effective surface area of the fabricated CNE is 0.49 μm^2 (see Method section 2.1.4) In the measurement, the ionic current through the nanopore is measured by a low noise current amplifier through the Ag/AgCl electrode inside the nanopore barrel. The open-circuit potential of the CNE is detected by a high impedance voltage meter.

The blocked current induced by NP translocation through the nanopore is sensitive to the diameter ratio between NP and nanopore. Because of the size variation of nanopipette nanopore, we investigated the changes of both ionic current and potential signals when different size NPs translocate through the same nanopore. We have tested negatively charged PS NPs with three sizes in the bath solution. The smallest PS NP has a diameter of 26 nm and a surface charge density of -0.037 C/m^2. The medium size PS NP has a

diameter of 60 nm and a surface charge density of -0.073 C/m^2. The largest PS NP has a diameter of 120 nm and a surface charge density of -0.067 C/m^2. The surface charge density was estimated from the zeta potential measurements in 10 mM PBS electrolyte using the dynamic light scattering method (see Method section 2.1.6). The nanopore experiment was performed with a 10 mM PBS electrolyte. A DC bias (V_{pore}) applied across the nanopore barrel typically generates two types of events, (i) translocation through the nanopore, and (ii) collision at the nanopore circumference and rebound back,[31-33] which is also a failed translocation event. The type (ii) non-translocation events dominated the results which is attributed to the large entrance barrier for the negatively charged NPs to enter the negatively charged nanopore. The V_{pore} applied through the nanopore barrel is not effective in reducing the barrier because it is heavily screened as a result of the long taper geometry of the nanopipette with a negative surface charge. A common strategy to boost the NP translocation event rate is to use a pressure gradient.[34, 35] Here, we employed a facile electrical method by taking advantage of the presence of CNE near the nanopore. Following previous reports [36-39] we used the AC DEP trapping method by applying an AC bias at the CNE (see Method section 2.1.9). The strong AC dielectrophoretic force steers NPs to move rapidly towards nanopipette tip and causes NP accumulation. The AC DEP applied through the CNE is highly effective. Type (i) translocation events with a high event rate can be observed in a few minutes even with a femtomolar concentration of PS NPs in the bath solution. However, a longer AC DEP application (*i.e.*, > 5 minutes) may lead to the permanent deposition of NPs on the glass wall and CNE surface. Therefore, we developed a DC/AC DEP hybrid method to avoid the electrical deposition of NPs but still

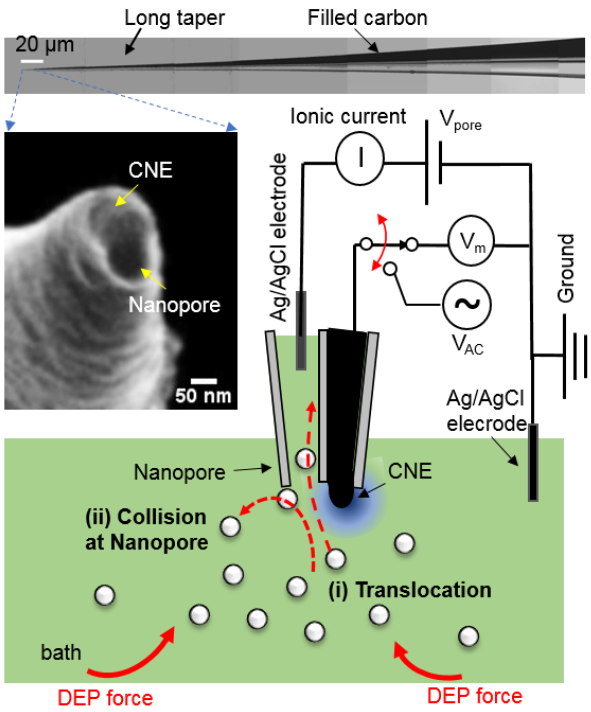

Figure 3.1: The schematic experimental setup of using nanopore- nanoelectrode nanopipette to probe the dynamic NP motion in solution. Top inset: a bright-field optical microscope image (stitched by 8 images) to show the long taper of the fabricated dual-barrel nanopipette. Left inset: an SEM image of the nanopipette tip. The bath solution (10 mM PBS) is grounded and V_{pore} is the bias applied across the nanopore barrel filled with the same solution as the bath. A high impedance differential amplifier connected to the CNE is used to measure potential (V_m) near the nanopipette tip, indicated by the blue shaded area. V_{AC} is applied for a short time to pre-concentrate the NPs near the nanopipette apex through the AC DEP force. Two types of single NP events, (i) translocation through the nanopore, and type (ii) collision of NPs at the nanopore circumference are illustrated.

allow an effective accumulation of PS NPs near the nanopore entrance. In hybrid method, a relatively big DC bias V_{pore} (~ 0.8 V) is first applied for a relatively long time (about 40-60 mins). We typically measure the individual NP translocation events during this stage. Large DC bias also slowly gathers a large number of NPs near the nanopipette tip vicinity. Then the AC bias was applied at the CNE, but only for a very short time (~30 - 60 seconds). The AC bias on the CNE generates a large DEP force, which effectively concentrates the NPs near the nanopipette tip,[39, 40] and triggers continuous translocations of individual

PS NPs through the nanopore. We often observed 15,000 to 30,000 translocation events, lasting 20-30 minutes. Generally, smaller 26 nm NPs resulted in a higher number of events compared to the larger 60 nm NPs. Considering that some NPs also move in other directions to escape from the nanopore, the number of assembled NPs is even bigger. Importantly, if more measurements are needed, the short AC DEP can be applied repeatedly to accumulate new assemblies with similar size, without going through the first DC bias stage again. Therefore, simple electric enrichment method (DEP) makes our measurement very efficient and enables us to systematically examine the effect of various parameters for nanopore and nanoelectrode detection.

3.3.2 Single NP Translocation and Collision Events at the Nanopore

To develop a better understanding of the current and potential signals detected by the nanopore-nanoelectrode method, we first studied the translocation of PS NPs by only applying V_{pore}. Before adding PS NPs in the solution, both current and potential baselines are stable and no transient changes are presented in the time traces at various biases. After adding PS NPs in the bath solution, transient changes are observed from time to time in both current and potential traces. Reproducible results have been acquired from more than 20 nanopipettes. The typical results in Figure 3.2 were acquired using nanopipette P1 after applying V_{pore} = +200 mV. The nanopore diameter of P1 is characterized to be around 71 ± 7 nm and the CNE effective surface area of P1 is about 0.53 μm^2 (see Method section 2.1.8). Here, we carefully compared the results between 26 nm and 60 nm PS NPs. The results of 120 nm PS NPs are also used for reference.

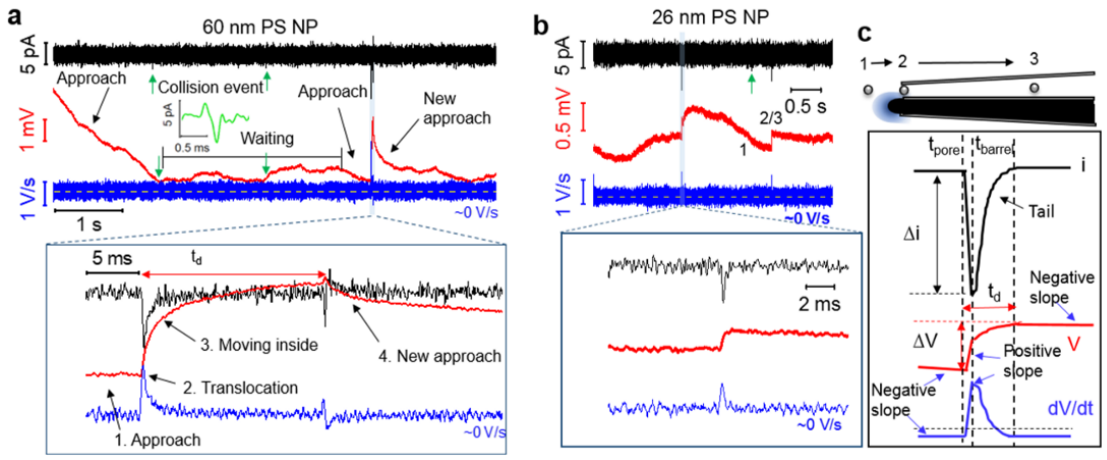

Figure 3.2: Individual NP events. (a) Current (black), potential (red) and the first derivative of potential (blue) time traces at 0.2 V (V_{pore}) after adding 100 pM concentration 60 nm PS NPs (a) and 26 nm PS NPs (b) in the 10 mM PBS bath solution. Small green arrows in (a) and (b) are types (ii) events. The current change of one such event is shown in the zoom-in plot in (a) in green color. The large current spikes are shown in (a) and (b) are type (i) events, which are also shown in the zoom-in traces. Current and potential traces are collected at 5 kHz and 40 kHz sampling rates and smoothed using a moving average method with 0.1 ms (5 points) moving window size for current and 0.2 ms (10 points) moving window size for potential, respectively. (c) Schematic illustration of the current and potential signals induced by the single NP translocation through the nanopore barrel. Translocation time, current spike height and potential step height are denoted respectively as t_d, Δi, and ΔV. The t_d is also divided into two: time duration at nanopore entrance (t_{pore}) and time duration inside the nanopore barrel (t_{barrel}).

Figure 3.2a shows the typical changes observed in current and potential time traces after adding 60 nm PS NPs in the bath solution. More data can be found in the online version of the article.[41]. The current baseline is quite stable. In contrast, the potential baseline fluctuates significantly. As we showed before with GNPs,[25] these potential changes reflect the movement of PS NPs near the nanopore entrance. In the beginning, the potential baseline decreases continuously, suggesting that a few NPs approach the vicinity of the nanopore. Then, the potential baseline stays at the same level for a while, suggesting that the NPs are "waiting" outside the nanopore. During this time, there are also a few small current spikes (two are indicated by the green arrows and a zoom-in of the small spike is

shown in the inset in green color), coupled with small dips in potential (see Method section 2.1.11). These small current spikes are attributed to the unsuccessful NP translocation events (type (ii) in Figure 1), which will be further discussed later. Finally, a distinctive downward current spike and a sharp rise in potential appear, indicating a successful translocation event. The zoom-in of the event is shown in the Figure below. The duration t_d of the downward current spike is about 22 ms and the height Δi is about 11 pA. The current spike displayed an asymmetric triangular shape, showing a long tail in the current spike. The long tail is also obvious in the potential trace and can be explained by the interaction at the interface between the NP surface and the inner wall of the nanopipette. In the time trace of the first derivative of the potential (blue color), the fast-rising potential change as a result of NP translocation appeared as an upward spike with a magnitude up to 2.1 V/s. All other potential changes, including several type (ii) events, are too slow to be distinguishable in the dV/dt trace. The small kink in the potential and the small jump in the current trace at the end of step 3 is likely the indication of the arrival of the next NP to the potential sensing zone of the CNE, which may be arisen from the sudden change of the CNE potential.

The same nanopipette P1 was used to study the translocation of 26 nm PS NPs. Compared with 60 nm PS NP, the diameter of 26 nm NP is much smaller than the diameter of the nanopore of P1. Figure 3.2b shows the typical current and potential time traces. Similar to the results of 60 nm NP, the current baseline is stable but the potential baseline fluctuates with the NP motion near the nanopipette tip. Two downward current spikes appeared, coupled with sharp-rise potential changes. These current and potential changes are assigned to the translocation of 26 nm PS NPs. When zooming in the first current spike, we noticed

the current spike shape became more symmetric with a short tail. The potential change also flats out quickly and becomes step-wise shaped. The duration t_d of the downward current spike is about 0.4 ms and the height Δi is about 7 pA. The Δi is 3 - 4 pA smaller (27% - 36%) than that of 60 nm NP and can be attributed to the smaller volume exclusion of the ion flow. The shape changes in the current spike and potential step suggest that the 26 nm PS NP is easier to translocate through the nanopore and moves faster inside the long taper portion of the nanopipette. Considering the surface charge density and surface area of NPs, the 60 nm NP is expected to experience more than 10 times bigger electrokinetic force than the force on the 26 nm NP. The obvious contradiction suggested that the translocation speed of NP is sometimes strongly affected by the interfacial interaction between NP surface and the nanopore inner wall surface. This is reasonable considering the size difference between the 26 nm, 60 nm PS NPs and the inner diameter of the nanopore barrel.

The results in Figures 3.2a and 3.2b demonstrated how the translocation event of PS NP was affected by the interactions between NP and the inner surface of the nanopore barrel. Figure 3.3c summarizes the general shape of the current, potential, and dV/dt changes generated by the translocation events. Before the dramatic decrease of current, the potential often decreases gradually with a small negative slope (dV/dt), associating with the approach of a negatively charged NP from position 1 to 2. The width of the downward current spike is characterized by the duration time t_d, which can be further divided into t_{pore} and t_{barrel}. The t_{pore} is the time for the NP to pass the narrowest region of the nanopore entrance (position 2). Normally, the NP moves fast in that region and the t_{pore} is very short. Correspondingly, the potential appears as a sharp rise and the dV/dt reaches the positive maximum in this time duration. However, prolonged t_{pore} can appear when the NP motion

near the nanopore orifice is slowed down (see results in Figures 3.3 and 3.4). When this happens, the bottom of the current spike flattens and the shape becomes rectangular. Meanwhile, the magnitude of dV/dt is also smaller. t_{barrel} is the time for the NP to move in the narrow nanopore barrel after passing position 2 (between 2 and 3 in Figure 3.2c), which is responsible for the asymmetric tail in the current spike. Because of the long taper geometry, the movement of NP deep inside the narrow barrel still impacts the barrel resistance R_b, and thus the overall current of the nanopore and the potential at the CNE.[25] Obviously, t_{barrel} is also sensitive to the interfacial interaction between NP surface and the inner surface of the nanopore barrel. Therefore, t_{barrel} of the current spike for 60 nm NP is much longer than that of 26 nm NP. During this time, the potential increases to reach maximum and the dV/dt falls off from the positive maximum, with the changing rate depending on the details of interactions.

Although we successfully observed the type (i) translocation events for PS NPs (both sizes) driven by a DC bias, the event rate was quite low. Under the same condition, the event rate is also much lower compared to that of GNPs. Therefore, the electric driving force generated by V_{pore} is less effective for PS NPs than for polarizable GNPs. In contrast, we observed many small current spikes with short time durations, along with small and slow potential changes (see green arrows in Figures 3.2a-b and the zoom-in of one event in the inset of Figure 3.2a). This small current and potential changes appeared more often in the results of 60 nm NPs. The small current spikes have been reported before and were assigned to the collision events of NPs with the nanopore orifice.[31-33] We further confirmed it by analyzing the data from 120 nm PS NPs, which obviously could not enter the 71 nm size nanopore of P1. Indeed, only small current spikes (with slightly bigger

amplitude) were observed for 120 nm PS NPs (see Method section 2.1.11), suggesting that the origin of these small current spikes is as a result of the type (ii) non-translocation events.

3.3.3 Dynamic Assembly of PS NPs Near the Nanopipette Apex

We have observed the slow accumulation of negatively charged GNPs near the nanopipette tip after applying a large DC bias across the nanopore barrel, which generates a DC DEP force on the GNP because of the highly enhanced (~10^7 V/m) non-uniform electric field near the nanopore.[25] The polarization of conductive GNPs by the enhanced electric field helps to reduce the electrostatic repulsion between GNPs, leading to the formation of short pearl chain structure. Following the accumulation, the GNPs in a cluster translocated through the nanopore one after the other. As we discussed in section 2.1, the DC bias V_{pore} induced DC DEP force did not work well for PS NPs. We instead used the hybrid DC/AC DEP method to pre-concentrate the PS NPs to the nanopore entrance and investigated the translocation events. We have tested about 10 nanopipettes with various AC DEP trapping conditions. Thorough studies have been carried out by four nanopipettes with the same trapping condition and multiple experiments were conducted for each nanopipette. We will discuss the representative results below.

In one experiment, we studied the dynamic events of 26 nm PS NPs from a crowded assembly using the nanopipette P2 (which has a nanopore with 45 ± 4 nm in diameter and a CNE with an exposed surface area of about 0.56 μm^2). The initial NP concentration in the bath solution was 100 pM. After a 30 s AC DEP following a 40 minutes DC DEP, we switched to the detection mode and applied different V_{pore} biases to study the NP accumulation. The ionic current baseline remained more or less at the same level. However,

the potential baseline descended dramatically (more negative). The potential baseline change suggested that a large number of NPs were successfully accumulated. Instead of a few isolated events, large downward current spikes appeared with high density in the ionic current time trace. Corresponding potential and dV/dt changes appeared in the potential and dV/dt time traces. As shown in Figures 3.3a and 3.3b, two types of data were observed. Time traces (1) and (2) show the continuous translocation of individual NPs and small NP clusters, respectively. The zoom-in of the trace (2) showing the details of the clusters (yellow shaded) is displayed at the right. Each cluster typically contains 2 to 6 NPs. The type (1) data often lasted for a few minutes (< 5 minutes) but the type (2) only appeared for less than 1 minute. The two types of data appeared one after the other and alternatively in the measurements (see Figure 3.6). With the increase of V_{pore}, the duration time for type (1) data increases but the duration time for type (2) data decreases. These observations imply that the large NP assembly contains many small ordered domains, which are formed by evenly distributed individual NPs. The size of these domains vary. At the boundaries of ordered domains, the NPs are not evenly distributed and many small NP clusters appeared (see illustration in Figure 3.3f). When the magnitude of the external electrical force is increased by the increase of V_{pore}, the ordered domains grow in size and merge.

The translocation event rate is found to change with time, which reflects the dynamic change in the NP density of the assembly. In one experiment run, we investigated how the translocation event rate changed with time after stopping AC DEP trapping, under a constant V_{pore} = 200 mV. The translocation event rate was determined using the type (1) data and each point was averaged over a time duration of 20 s. As shown in Figure 3c, the NP translocation event rate was about 21 events/s right after applying AC DEP trapping.

In a minute, the event rate jumped to about 100 events/s and then rapidly decreased to about 20 event/s. Afterward, the event rate became stable and decreased gradually. The appearance of the event rate spike suggests that the core of the NP assembly was likely formed some distance away from the nanopore orifice. The core of the assembly then moved to the nanopore entrance after V_{pore} was on. In addition to relatively uniformly distributed current spikes and potential steps from translocation events, there were also small current and potential changes induced by non-translocation events, but the rate of these events was very low. After 30-40 minutes, the translocation events became rare and the NP non-translocation events dominated again. At this time, all the accumulated NPs dissipated away from the nanopipette apex. The following discussions are based on the data acquired when the event rate is stabilized, which is around 3-6 minutes after applying the AC DEP.

Figure 3.3d shows the typical current spikes and potential steps induced by translocation events from NPs in the ordered domain. The shape of the current spike and potential step in the domain boundaries (trace (2)) is also similar. The overall shape of these current spikes and potential steps can be explained by the diagram in Figure 2c. Compared with the isolated translocation events, differences including the shorter tail of the current spike and the tilted potential step, are observed and can be explained by the high NP concentration gradient across the nanopore and the repulsion forces between the NPs in the large assembly, which drives the NP at a higher velocity during the translocation event.

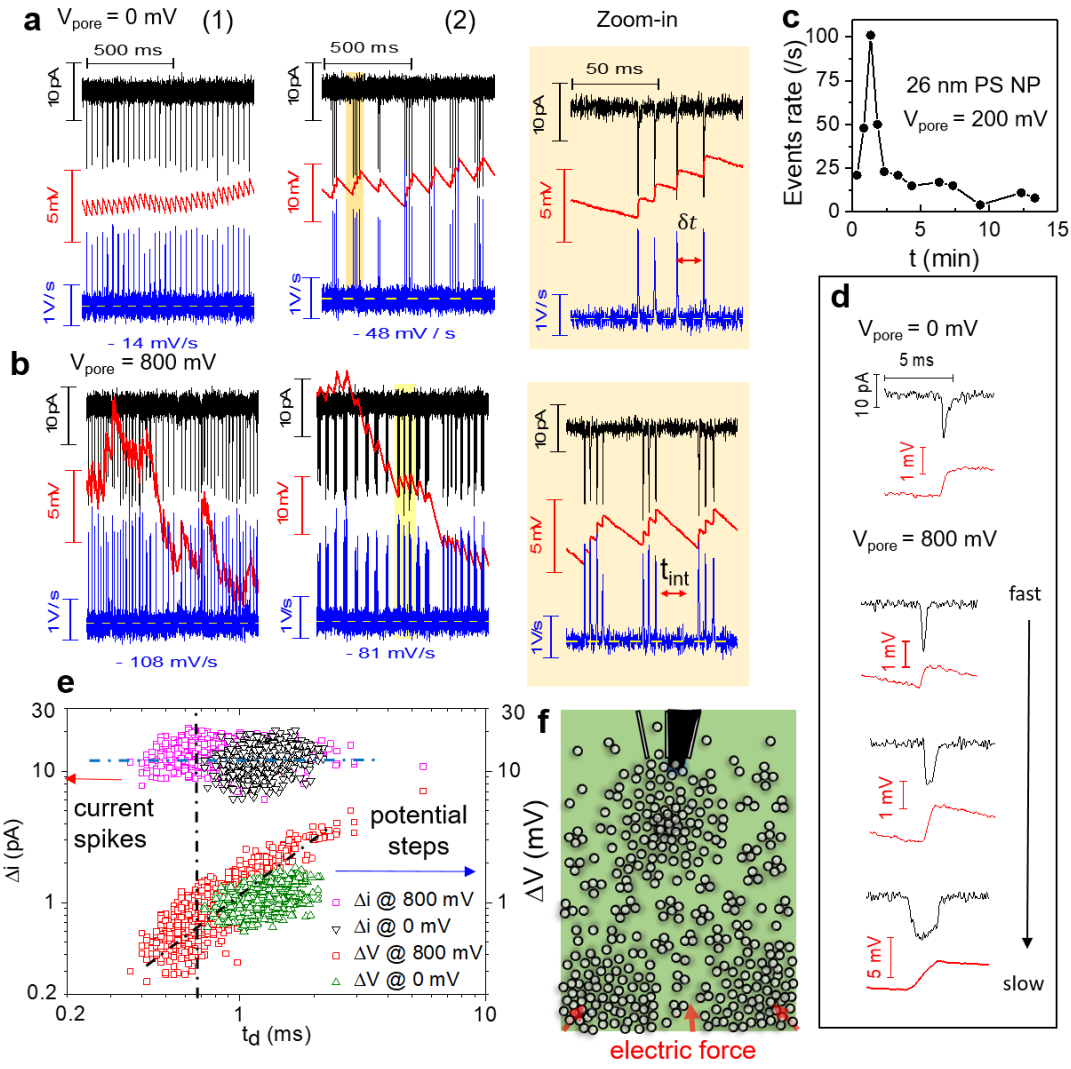

Figure 3. 3: The translocation of 26 nm PS NPs after short (~30sec) AC DEP trapping. (a-b) Current (black), potential (red) and the first derivative of potential (dV/dt, blue) traces at V_{pore} = 0 mV (a) and 800 mV (b) after adding 26 nm PS NPs in the bath solution. Time traces (1) in (a) and (b) show the continuous translocations of NPs. Time traces (2) in (a) and (b) represent the translocation of NP clusters. The yellow shaded regions of traces (2) in (a) and (b) are respectively shown in zoom-in traces at the right. The inter-cluster time gap and inter-event interval are denoted as t_{int} and δt, respectively. (c) The translocation event rate as a function of time at V_{pore} = 200 mV. Each point is averaged over a 20 s data. (d) Typical current spikes and potential steps at 0 mV and 800 mV. Three representative fast to slow translocation events at 800 mV bias are displayed. (e) Scatter plots of NP translocation events in type (2) data at 0 mV and 800 mV bias. N = 831 for 0 mV and N = 694 for 800 mV bias. The dashed lines are eye-guides. (f) Schematic Illustration of the NP assembly structure near the pipette apex, showing three domains and non-uniform boundary regions between domains. The red arrows indicate the direction of the DC DEP electric force as a result of the applied V_{pore}.

We compared the events in traces (1) and (2) of Figure 3.3a. For the continuous translocation of individual NPs in the ordered domain (trace (1), the interval between the uniformly distributed current spikes is about 29 ms. The potential trace also displays repeated changes as tilted potential steps. For the translocation of clusters (trace (2)), the time gap between two clusters (t_{int}) varies but is always much longer than 29 ms. However, the interval between two events in a cluster (δt) is about 9 ms, which is much shorter than 29 ms, suggesting that the NPs are much closer to each other within a cluster. Besides, the potential drops continuously during the time gap between

two cluster translocation events but increases in a stepwise manner inside a cluster translocation event. Therefore, the NPs in a cluster approach the nanopore together, then the cluster breaks apart and individual NPs in the cluster enters the nanopore sequentially. Similar results are also observed in Figure 3b.

The appearance of small PS NP clusters reminds us of the small GNP clusters reported in previous work.[25] In a GNP cluster, the interval between two events was even shorter and the potential changes showed flat steps (*i.e.*, slope dV/dt was close to zero). Therefore, the structure of small GNP clusters was speculated to be a one-dimensional pearl chain. Here, the interval is bigger and the potential steps also display bigger negative slopes (dV/dt). These differences suggest that the NPs in a PS NP cluster are not tightly bound. Without the strong polarization, the PS NPs do not form the chain structure.

We can also find the effect of applied bias V_{pore} on the current and potential signals induced by the translocation events. Figures 3.3a, b, and d show the typical results at V_{pore} = 0 mV and 800 mV. At 0 mV, the large NP concentration gradient and the repulsive forces

between charged NPs sustain continuous translocation events. The application of V_{pore} = 800 mV provides an extra pushing, further compresses the NP assembly and drives NPs to move faster toward and through the nanopore orifice. It is evident from the trace (2) of Figure 3b that both t_{int} and δt are reduced, although the number of NPs in a cluster did not change with bias. For the uniform single NP translocation in trace (1) of Figure 3b, the event rate is also increased to about 34 events/s from 26 events/s at 0 mV. In the potential steps, the magnitude of the negative slope increases significantly, suggesting faster approaching speeds.

Figure 3.3e shows the statistical results for current spikes and potential steps of the translocation events from NPs in the ordered domain at two different biases. The most noticeable difference is in the distribution of time duration t_d, which is much broader at 800 mV. This is also evident in Figure 3d, showing three signals with very different t_d at V_{pore} = 800 mV. For nanopores with small aspect ratio geometry, the t_d always decreases with the increase of bias because the NPs move faster at higher bias.[33, 42] Here, we indeed observed a large number of fast events with t_d shorter than 0.7 ms (left side of the vertical dash line) at 800 mV. However, there are also many events with similar or even bigger t_d than that at 0 mV (right side of the vertical dash line). The shape of these current spikes and potential steps are shown in Figure 3.3d. The t_{pore} is longer and the spike shape is close to a rectangular shape. At 800 mV, the NP has a higher momentum and therefore has a higher probability to move off-axis and collide with the nanopore inner surface, leading to a slowed translocation through the orifice.

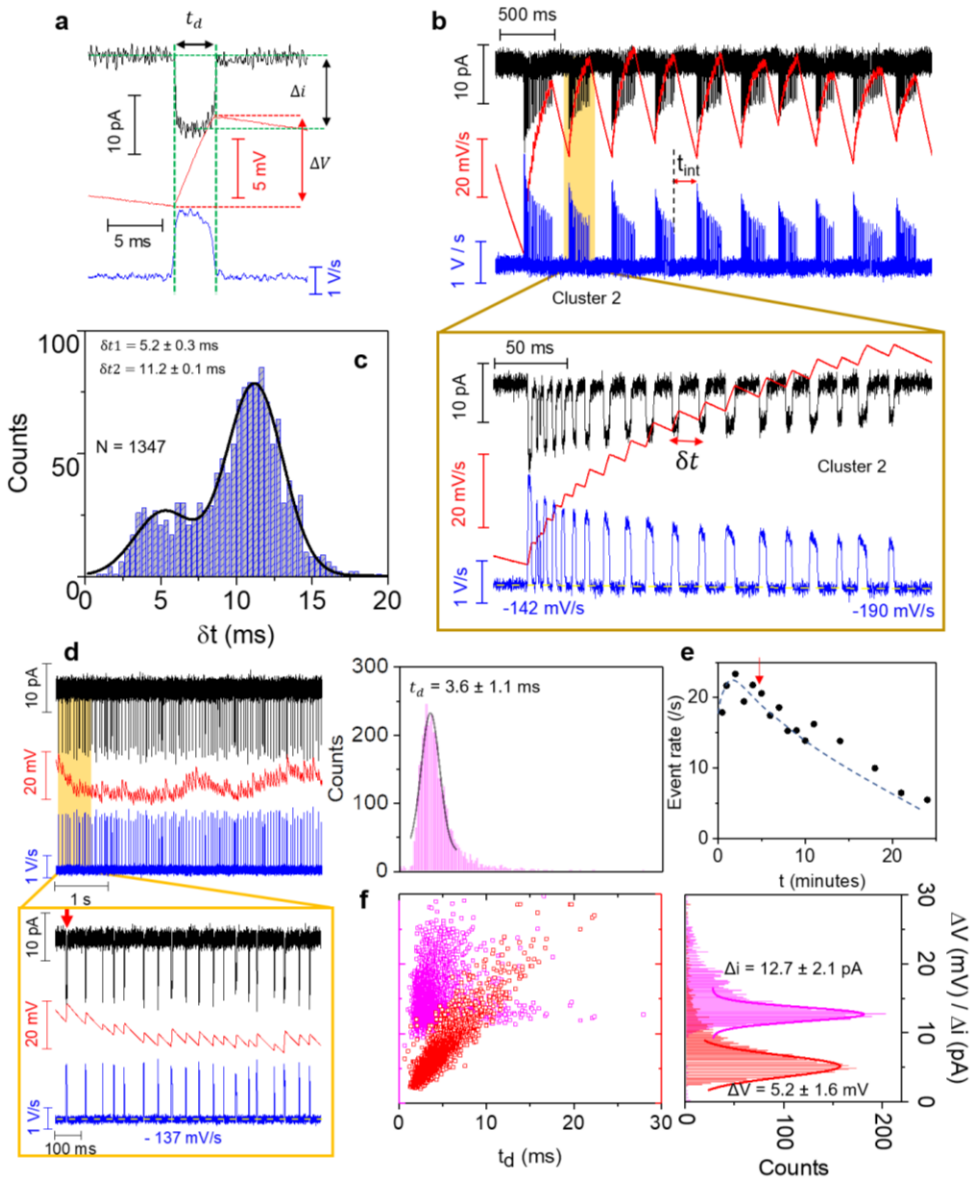

Figure 3. 4: Translocation events of 60 nm PS NPs after the formation of a large assembly. (a) The zoom-in of a typical translocation event signal (indicated by the red arrow in trace (d)), showing current spike (black), potential step (red) and the first derivative of potential (blue). (b) Typical current, potential and the first derivative of potential time traces with V_{pore} = 200 mV and after applying 30 s AC DEP. The zoom-in time trace of cluster 2 (highlighted by the yellow strip) is shown below. (c) The histogram of δt from 1347 events and the solid black line in the histogram is a Gaussian fit. (d) Continuous translocation events of NPs at V_{pore} = 200 mV and a few minutes after applying 1 min AC DEP. The yellow shaded region is shown in the zoom-in trace below. (e) The plot of event rate *vs.* time after applying a 1 min AC DEP. The event rate data point is averaged over 20 s. The dashed line is an eye guide. (f) Scatter plot and histograms of t_d, Δi (pink color) and ΔV (red color) for 3806 translocation events. The solid lines in the histograms are Gaussian fits.

The Δi of current spikes did not change much with V_{pore} or t_d, suggesting the blocking current origin of the current spikes. At 0 mV, the ΔV is also insensitive to t_d. But at 800 mV, the ΔV increases linearly as a function of t_d with a large slope, which has been explained previously for GNPs.[25] In short, the slower NPs are closer to the CNE and induce bigger ΔV.

In another study, we investigated the translocation of 60 nm PS NPs through the 59 ± 6 nm diameter nanopore of nanopipette P3. The concentration of NPs in the bath solution was 1 pM. Here, the diameters of the nanopore and NP are the same, which is very different from the previous case with nanopipette P2 and 26 nm PS NPs. Also, the CNE effective surface area of P3 is 3.43 ± 0.24 μm^2, which is much bigger than that of P2 (see Methods section 2.1.8). Therefore, the 60 nm PS NP will experience more difficulties entering the nanopore of P3. Figure 3.4 shows the typical results with V_{pore} = 200 mV after 30 s AC DEP trapping. The overall features are very similar to the results of 26 nm NPs shown in Figure 3. One noticeable difference is that the shape of the current spikes all became rectangular (see Figure 3.4a). The current spike shape is similar to the slow event in Figure 3.3d, but the bottom of the current spike is flatter. The shape change in current spikes is a clear sign of the increased interaction between NP and the nanopore orifice. The tail of these rectangular shapes current spike is not obvious because t_{barrel} becomes relatively short, suggesting the major bottleneck of the NP motion is at the nanopore orifice.

The translocation of NP clusters appeared immediately after 30 s AC DEP trapping, as a typical trace shown in Figure 3.4b. The number of spikes in each cluster was often more than 20, suggesting a much bigger cluster size formed by these 60 nm NPs. The

bigger cluster size likely reflects the bigger size of 60 nm NP and the increased difficulty of the 60 nm NP to translocate through the nanopore. The slower movement, bigger surface area and longer 'waiting time' outside the nanopore lead to the formation of bigger clusters. The mean t_{int} between two 60 nm NP clusters was 142.1 ± 75.5 ms. In contrast, the mean t_{int} between two 26 nm NP clusters in Figure 3b was 68.7 ± 28.6 ms (Figure 3.5). Therefore, it took more time for the larger clusters of 60 nm NPs to reach the nanopore orifice. Systematic changes were observed in the current spikes and potential steps within a cluster. This is different from the small clusters of 26 nm NP described previously, in which all the current spikes and potential steps are similar. As shown in the zoom-in plot of cluster 2, the Δi of current spikes decreases gradually

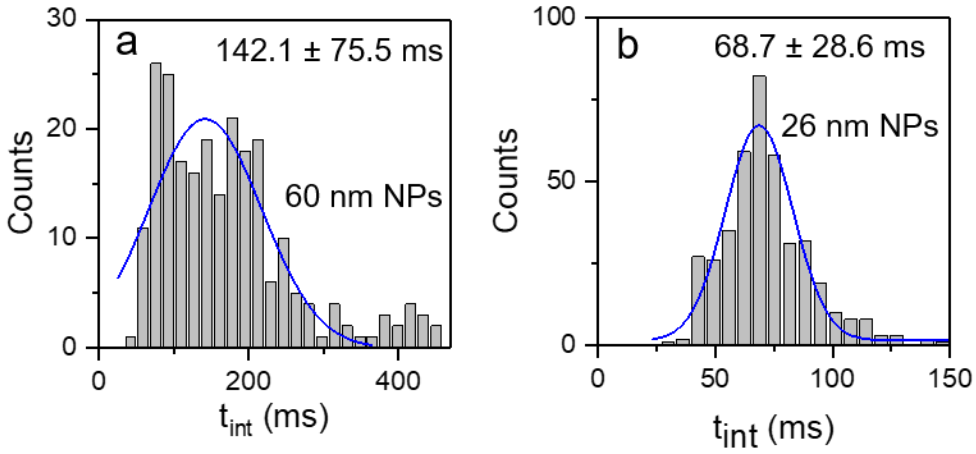

Figure 3. 5: The histograms of inter-cluster time (t_{int}) of 60 nm NPs (a) (same dataset as Figure 3.4b) and 26 nm NPs (b) (same dataset as Figure 3.3a). The solid blue line in the histogram is a Gaussian fit.

for about 37% from the first spike to the last spike. Meanwhile, the spike duration time t_d and the interval between two spikes δt increases gradually. These changes are attributed to the larger size of NP cluster formed by 60 nm NPs and the increased ionic current blocking capability of larger NPs with more charges. The current spike height change is

attributed to the change of access resistance as a result of the presence of a large cluster near the nanopore entrance. After several NPs were translocated, the size of the NP cluster is reduced, leading to reduced access resistance and thus reduced height Δi of blocking current spike. As shown in Figure 3.4c, the histogram of δt shows two peaks at 5.2 ms and 11.2 ms, respectively. The first peak is from the interval between the first few spikes in a cluster and the second peak is from the interval between the later current spikes. Therefore, the interval between two neighboring spikes increased more than 2 times. The time duration t_d of each spike also increased by about ~43% from the first spike to the last spike in a cluster. The increase of δt and t_d revealed the effect of repulsive force on the translocated NP imposed by other NPs in the cluster. With fewer NPs outside, the repulsive force is reduced and the translocation speed of the NP is reduced, leading to slower translocations. The potential trace also shows tilted stepwise potential changes. We observed that the magnitude of the positive slope decreased from about 1.6 V/s of the first few steps to 0.9 V/s of the last few steps, confirming the reduction of NP translocation speed. The negative slope of the potential step gives the information of NP approaching speed. Interestingly, the negative slope changed from -142 mV/s to -190 mV/s. So the NP cluster with shrinked size moves faster toward nanopore entrance, which may be attributed to the reduced geometrical hindrance by neighboring clusters and CNE.

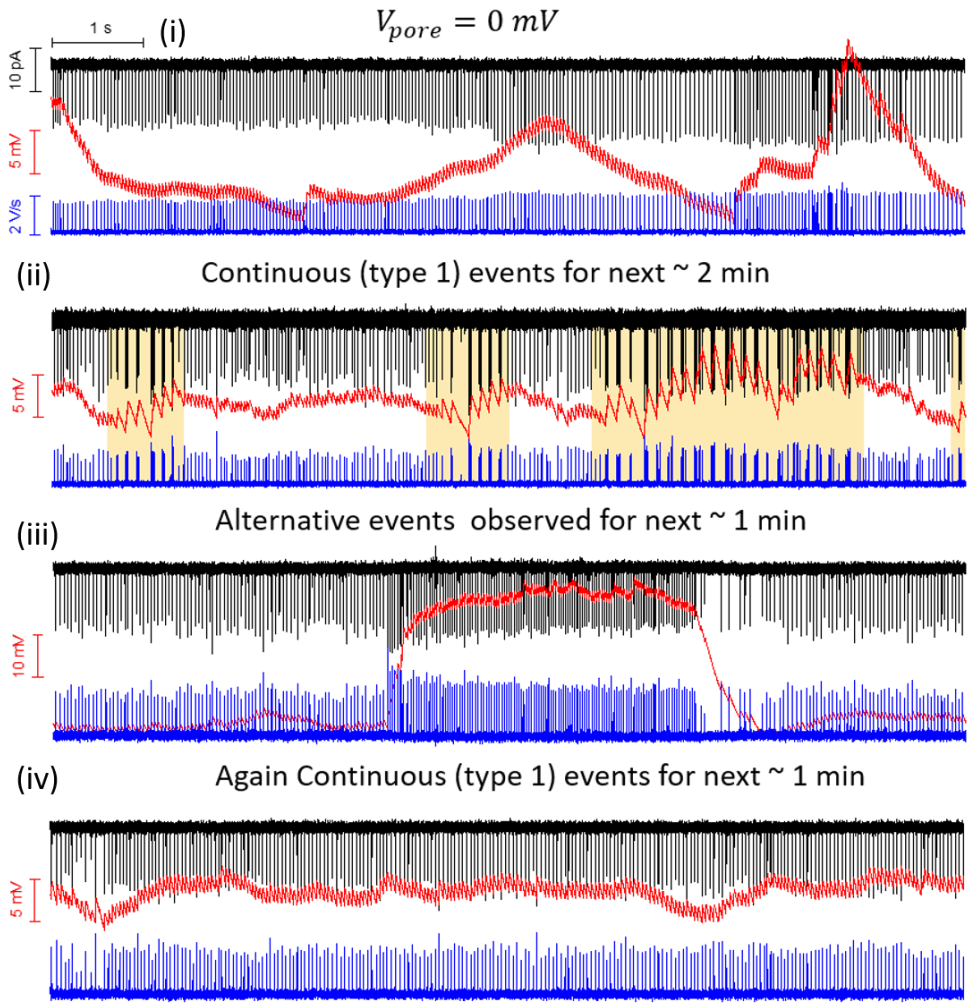

Figure 3. 6: (i)-(iv) Representative 10s duration time traces of current (black), potential (red) and the first derivative of potential dV/dt (blue) of the 26 nm NPs translocation through the pipette P2 after short (~30 sec) AC DEP trapping and at V_{pore} = 0 mV. The clustered (type 2) events are highlighted in yellow color. The traces appeared sequentially from (i) to (iv).

After all the accumulated NPs were dissipated away from the nanopipette apex, we applied again 1 minute of AC DEP trapping (no DC DEP) to accumulate and drive another large NP assembly to the nanopipette apex. No small clusters were observed, suggesting that the whole PS NP assembly becomes homogenous as a result of the longer AC DEP trapping time. The change of event rate with time is shown in Figure 3.4e, which is similar

to Figure 3c, though the decay in the event rate is much slower. A typical trace is shown in Figure 3.4d, which is taken a few minutes after AC DEP (see the red arrow in Figure 3.4e). The current spikes are uniform with similar current spike height Δi and time duration t_d. The spikes are also distributed evenly and the interval between two events is about 47 ms. The periodicity is also clearly illustrated by the pronounced peak near 20 Hz in the power spectral density (PSD) analysis of current and potential time traces (see supporting information S10).

We also performed a statistical analysis of these current spikes and potential steps appeared in a 3 minutes time window near the time indicated by the red arrow in Figure 3.4e. The histograms and scatter plots of Δi and ΔV are shown in Figure 3.4f. The mean t_d of the translocation event is 3.6 ms. Compared with the results in Figure 3e, the mean t_d here is longer, supporting the conclusion that the translocation is more difficult in this case. As shown in the histogram of Δi, the mean current spike height Δi by Gaussian fit to the peak is 12.7 pA. Considering the nature of blocking current, it is surprising that Δi here is similar to that in Figure 3e. To understand this, we checked the Δi of individual current spikes before applying AC DEP trapping, which was about 21 pA. Therefore, Δi is likely suppressed by NP accumulation. One possibility is that the high density of 60 nm NPs near the nanopore entrance induces ion depletion,[43, 44] resulting in ionic current reduction. This is supported by the fact that the volume of 60 nm NP is about 12 times bigger than that of 26 nm NP. Interestingly, the Δi histogram also has a long tail extending to bigger values. Most of these bigger current spikes appeared earlier. They also have a shorter t_d, as shown in the scatter plot. This is consistent with the systematic change we observed in the current spikes in a cluster (Figure 3.4b) and is attributed to the bigger access resistance at

the earlier time. The analysis of Δi is more challenging here because the resistive pulses are also affected by neighboring NPs. The mean potential change of each potential step is about 4.7 mV, which is much bigger than that of the previous case (Figure 3e), either 0.8 mV at V_{pore} = 800 mV or 1 mV at V_{pore} = 0 mV. This is expected because of the bigger size and bigger surface charge density of 60 nm NP and the slower translocation speed of the NP through the nanopore orifice. Again, the distribution of ΔV is broad and a linear relationship between ΔV and t_d is evident.

The data shown in Figures 3.3 and 3.4 revealed the dynamic assembly of PS NPs in solution. Under DEP forces, a significant number of PS NPs in the solution can be accumulated near the nanopipette tip. In this process, some NPs form small clusters with neighboring ones, which is analogous to the nucleation process of the crystal formation process. Later on, with the increased magnitude and duration of the applied electric force, small clusters grow bigger and merge to form large uniform domains. Eventually, all the NPs in the assembly are well-packed, evenly spaced and the assembly becomes a large homogenous colloidal structure. This dynamic process is strongly affected by the physical and chemical properties of NPs (*i.e.*, size, surface charge), the interaction between NPs and the applied external force. The study of the dynamic assembly process of NPs near the nanopipette apex may provide us a better understanding of the general colloidal assembling dynamics.

3.4 Conclusions

In summary, we reported the multimode detection of dynamic events of insulating PS NPs in a solution using the multifunctional nanopipette. Because of the high entrance barrier of

the long taper quartz nanopipette for negatively charged PS NPs, it was difficult to drive individual PS NPs to enter the nanopore by simply applying a DC bias. However, we were able to effectively pre-concentrate a significant number of PS NPs near the nanopipette tip by using the combination of DC and AC DEP. The implementation of AC DEP was straightforward by taking advantage of the presence of the CNE at the nanopipette tip. The high NP concentration gradient and repulsive forces between NPs in the accumulated NP assembly triggered continuous translocation with a high event rate. Combining ionic current and potential detection, we were also able to analyze more complicated multi-NP events happening near the nanopipette tip. The large PS NP assembly was formed by many uniform domains. Small cluster structures formed by several PS NPs were also detected between domains. The NP assembly became more uniform when the applied external electric force was increased. Further, the effect of NP size on the structures of NP small clusters and large assembly was discussed. Overall, this study deepens our understanding of the dynamics of a colloidal system. We have demonstrated here that the nanopore-nanoelectrode nanopipette can be used to effectively study different dynamic events of dielectric NPs in an electrolyte.

Compared with conductive NPs, fewer methods are capable of single entity studies of insulating NPs. In recent years, individual insulating NPs have been investigated by novel optical methods, such as surface plasmon resonance imaging (SPRi) microscopy and super-resolution fluorescence microscopy.[45, 46] These imaging methods can reveal single NP dynamics in solution, but the experiment setups are complicated and expensive. ‘Nano-impact’ based electrochemical measurement method is simple and shows great potential for single insulating NP detection.[47-49] The detection of this method often relies on the

faradaic process. In contrast, for the reported method, there is no requirement for the label-free NP to be fluorescent or redox-active. Our results show that the nanopore-nanoelectrode nanopipette has the potential to be developed as both a nanoreactor and nanosensor to control and detect the motion and interactions between a few or a large number of charged NPs (either conductive or insulating) and investigating in real-time the dynamic formation of interesting multi-NP structures, such as NP superstructures. Especially, this method can be applied to study nanoscale biological entities, *i.e.*, liposomes and viruses. We have shown that the characteristics of the observed current spikes and potential step changes are sensitive to the interactions between the NP and the nanopore surface. With well-defined surface chemistry on both CNE and nanopore surface, it is possible to incorporate the molecule recognition capability to this method for biomedical applications.[15, 50, 51] Besides, the chemical binding can transiently define the NP-CNE distance, enabling more quantitative potential measurement by the nanoelectrode.

3.5: References

1. Pandey, P., et al., *Probing Dynamic Events of Dielectric Nanoparticles by a Nanoelectrode-Nanopore Nanopipette.* ChemElectroChem, 2018. **5**(20): p. 3102-3112.

2. Pandey, P. and J. He, *Detection and manipulation of single nanoparticle (NP) dynamic assembly process by the integration of nanopore and nanoelectrode.* Bulletin of the American Physical Society, 2018. **63**.

3. Pandey, P. and J. He, *Integration of Nanopore and Nanoelectrode for Single Entity Detection and Manipulation.* Biophysical Journal, 2018. **114**(3): p. 685a.

4. Kleijn, S.E.F., et al., *Electrochemistry of Nanoparticles.* Angewandte Chemie International Edition, 2014. **53**(14): p. 3558-3586.

5. Dykman, L. and N. Khlebtsov, *Gold nanoparticles in biomedical applications: recent advances and perspectives.* Chemical Society Reviews, 2012. **41**(6): p. 2256-2282.

6. Wang, W. and N. Tao, *Detection, Counting, and Imaging of Single Nanoparticles.* Analytical Chemistry, 2014. **86**(1): p. 2-14.

7. Oja, S.M., et al., *Nanoscale Electrochemistry Revisited.* Analytical Chemistry, 2016. **88**(1): p. 414-430.

8. Wang, Y., X. Shan, and N. Tao, *Emerging tools for studying single entity electrochemistry.* Faraday Discussions, 2016. **193**(0): p. 9-39.

9. Howorka, S. and Z. Siwy, *Nanopore analytics: sensing of single molecules.* Chemical Society Reviews, 2009. **38**(8): p. 2360-2384.

10. Kasianowicz, J.J., et al., Proc. Natl. Acad. Sci. U.S.A., 1996. **93**: p. 13770.

11. Shi, W., A.K. Friedman, and L.A. Baker, *Nanopore Sensing.* Analytical Chemistry, 2017. **89**(1): p. 157-188.

12. Lin, X., A.P. Ivanov, and J.B. Edel, *Selective single molecule nanopore sensing of proteins using DNA aptamer-functionalised gold nanoparticles.* Chemical Science, 2017. **8**(5): p. 3905-3912.

13. Terejánszky, P., et al., *Calibration-Less Sizing and Quantitation of Polymeric Nanoparticles and Viruses with Quartz Nanopipets.* Analytical Chemistry, 2014. **86**(10): p. 4688-4697.

14. Steinbock, L.J., et al., *Detecting DNA folding with nanocapillaries.* Nano letters, 2010. **10**(7): p. 2493-2497.

15. Tiwari, P.B., et al., *Quantitative study of protein–protein interactions by quartz nanopipettes.* Nanoscale, 2014. **6**(17): p. 10255-10263.

16. Zhou, K., et al., *Characterization of Hepatitis B Virus Capsids by Resistive-Pulse Sensing.* Journal of the American Chemical Society, 2011. **133**(6): p. 1618-1621.

17. Sze, J.Y.Y., et al., *Fine tuning of nanopipettes using atomic layer deposition for single molecule sensing.* Analyst, 2015. **140**(14): p. 4828-4834.

18. Yusko, E.C., et al., *Real-time shape approximation and fingerprinting of single proteins using a nanopore.* Nature Nanotechnology, 2016. **12**: p. 360.

19. Qiu, Y., et al., *Role of Particle Focusing in Resistive-Pulse Technique: Direction-Dependent Velocity in Micropores.* ACS Nano, 2016. **10**(3): p. 3509-3517.

20. Liu, S., et al., *Correlated Electrical and Optical Analysis of Single Nanoparticles and Biomolecules on a Nanopore-Gated Optofluidic Chip.* Nano Letters, 2014. **14**(8): p. 4816-4820.

21. Song, W., et al., *Optical and Electrical Detection of Single-Molecule Translocation through Carbon Nanotubes.* ACS Nano, 2013. **7**(1): p. 689-694.

22. Angeli, E., et al., *Simultaneous Electro-Optical Tracking for Nanoparticle Recognition and Counting.* Nano Letters, 2015. **15**(9): p. 5696-5701.

23. Yu, Y., et al., *Three-Dimensional Super-resolution Imaging of Single Nanoparticles Delivered by Pipettes.* ACS Nano, 2017. **11**(10): p. 10529-10538.

24. Tsutsui, M., et al., *Single-molecule sensing electrode embedded in-plane nanopore.* Scientific Reports, 2011. **1**: p. 46.

25. Panday, N., et al., *Simultaneous Ionic Current and Potential Detection of Nanoparticles by a Multifunctional Nanopipette.* ACS Nano, 2016. **10**(12): p. 11237-11248.

26. Hellberg, D., et al., *Bursting and spreading of liposomes on the surface of a static mercury drop electrode.* Electrochemistry Communications, 2002. **4**(4): p. 305-309.

27. Poon, J., et al., *Single graphene nanoplatelets: capacitance, potential of zero charge and diffusion coefficient.* Chemical Science, 2015. **6**(5): p. 2869-2876.

28. Sokolov, S.V., et al., *Electrode-particle impacts: a users guide.* Physical Chemistry Chemical Physics, 2017. **19**(1): p. 28-43.

29. Zhou, H., et al., *Observation of Single Metal Nanoparticle Collisions by Open Circuit (Mixed) Potential Changes at an Ultramicroelectrode.* Journal of the American Chemical Society, 2012. **134**(32): p. 13212-13215.

30. Wang, L., et al., *Dynamic Nanoparticle Assemblies.* Accounts of Chemical Research, 2012. **45**(11): p. 1916-1926.

31. Webb, J.R., et al., *Fabrication of a single sub-micron pore spanning a single crystal (100) diamond membrane and impact on particle translocation.* Carbon, 2017. **122**(Supplement C): p. 319-328.

32. Li, T., et al., *Observing single nanoparticle events at the orifice of a nanopipet.* Chemical Science, 2016. **7**(10): p. 6365-6368.

33. Bacri, L., et al., *Dynamics of Colloids in Single Solid-State Nanopores.* The Journal of Physical Chemistry B, 2011. **115**(12): p. 2890-2898.

34. Lan, W.-J., et al., *Pressure-Driven Nanoparticle Transport across Glass Membranes Containing a Conical-Shaped Nanopore.* The Journal of Physical Chemistry C, 2011. **115**(38): p. 18445-18452.

35. Lan, W.-J. and H.S. White, *Diffusional Motion of a Particle Translocating through a Nanopore.* ACS Nano, 2012. **6**(2): p. 1757-1765.

36. Freedman, K.J., et al., *Nanopore sensing at ultra-low concentrations using single-molecule dielectrophoretic trapping.* Nat Commun, 2016. **7**: p. 10217.

37. Tanaka, S., et al., *Tailoring particle translocation via dielectrophoresis in pore channels.* Scientific Reports, 2016. **6**.

38. Ying, L., et al., *Frequency and Voltage Dependence of the Dielectrophoretic Trapping of Short Lengths of DNA and dCTP in a Nanopipette.* Biophysical Journal, 2004. **86**(2): p. 1018-1027.

39. Freedman, K.J., et al., *On-Demand Surface- and Tip-Enhanced Raman Spectroscopy Using Dielectrophoretic Trapping and Nanopore Sensing.* ACS Photonics, 2016. **3**(6): p. 1036-1044.

40. Chen, D., H. Du, and C. Tay, *Rapid Concentration of Nanoparticles with DC Dielectrophoresis in Focused Electric Fields.* Nanoscale Research Letters, 2010. **5**(1): p. 55-60.

41. Popular Pandey, N.p., chang shuai, Peipang, xuewen wang, and Fu Qiang, Jin He, *Probing dynamic events of dielectric nanoparticles by ananoelectrode-nanopore nanopipette.* ChemElectroChem, 2018.

42. Davenport, M., et al., *The Role of Pore Geometry in Single Nanoparticle Detection.* ACS Nano, 2012. **6**(9): p. 8366-8380.

43. Chun, H., *Electroosmotic Effects on Sample Concentration at the Interface of a Micro/Nanochannel.* Analytical Chemistry, 2017. **89**(17): p. 8924-8930.

44. Pu, Q., et al., *Ion-Enrichment and Ion-Depletion Effect of Nanochannel Structures.* Nano letters, 2004. **4**(6): p. 1099-1103.

45. Wang, S., et al., *Label-free imaging, detection, and mass measurement of single viruses by surface plasmon resonance.* Proceedings of the National Academy of Sciences, 2010. **107**(37): p. 16028.

46. Shen, H., et al., *Single Particle Tracking: From Theory to Biophysical Applications.* Chemical Reviews, 2017. **117**(11): p. 7331-7376.

47. Quinn, B.M., P.G. van't Hof, and S.G. Lemay, *Time-Resolved Electrochemical Detection of Discrete Adsorption Events.* Journal of the American Chemical Society, 2004. **126**(27): p. 8360-8361.

48. Boika, A., S.N. Thorgaard, and A.J. Bard, *Monitoring the Electrophoretic Migration and Adsorption of Single Insulating Nanoparticles at*

Ultramicroelectrodes. The Journal of Physical Chemistry B, 2013. **117**(16): p. 4371-4380.

49. Toh, H.S. and R.G. Compton, *Electrochemical detection of single micelles through 'nano-impacts'.* Chemical Science, 2015. **6**(8): p. 5053-5058.

50. Krishnakumar, P., et al., *Slowing DNA translocation through a nanopore using a functionalized electrode.* ACS nano, 2013. **7**(11): p. 10319-10326.

51. Yusko, E.C., et al., *Controlling protein translocation through nanopores with bio-inspired fluid walls.* Nature Nanotechnology, 2011. **6**: p. 253.

CHAPTER 4: DIFFERENTIATION OF METALLIC AND DIELECTRIC NANOPARTICLES IN SOLUTION BY SINGLE-NANOPARTICLE COLLISION EVENTS AT THE NANOELECTRODE

In Chapter 4, we demonstrate a highly effective method to generate and detect single nanoparticle (NP) collision events on a nanoelectrode in aqueous solutions. The nanoelectrode of a nanopore–nanoelectrode nanopipette is first employed to accumulate NPs in solution by dielectrophoresis (DEP). Instead of using amperometric methods, the continuous individual NP collision events on the nanoelectrode are sensitively detected by monitoring the open-circuit potential changes of the nanoelectrode. Metallic gold NPs (GNPs) and insulating polystyrene (PS) NPs with various sizes are used as the model NPs. As a result of the higher conductivity and polarizability of GNPs, the collision motion of a GNP is different from that of a PS NP. The difference is distinct in the shape of the transient potential change and its first-time derivative detected by the nanoelectrode. Therefore, the collision events by metallic and insulating NPs on a nanoelectrode can be differentiated from their polarizability. DEP induced NP separation and cluster formation can also be probed in detail in the concentrated mixture of PS NPs and GNPs. The contents presented in this chapter are the slightly modified version of my published peer-reviewed research article.[1, 2]

4.1: Introduction

Nanoparticles (NPs) have been widely used in biomedical, energy, and environmental applications.[3-5] As a result of the ubiquitous nature of the synthetic and biological NPs around us, it is very important to have reliable, cost-effective, and facile methods to study different properties of the NPs. Single-entity electrochemistry techniques have been

developed rapidly in NP analysis, providing new insights different from the traditional ensemble measurements.[6, 7] In the last two decades, the nanopore-based techniques have been developed into a powerful method to study NPs at the single-NP level.[8-11] Utilizing the ionic current change induced by the single-NP translocation event, the shape, charge, and even dynamic orientation of NP can be revealed.[12-19] Another technique, the electrochemical detection of single-NP collisions on an ultra-small electrode (UME, micron- and nanoscale) has also emerged as a very useful electrochemical method to study individual NPs in solution.[20-23] The so-called nanoparticle nano-impact technique enables us to characterize, quantify, and detect the nanoparticles and biological entities.[24] Also, they allow us to understand the inter-particle interactions and the aggregation of NPs in the solution and at the UME surface; probe the redox reaction kinetics of catalytic NPs and electroactive species at the surface of NPs, and obtain information on the surface chemistry of NPs.[25-28]

To date, most single-NP collision experiments are measured by amperometric methods. Typically, redox-active molecules and/or catalytically active NPs are needed [29-38] to amplify the electrochemical current to at least pA level for detection. Instead of current sensing, it has been demonstrated that the NP collision events can also be detected by the open-circuit potential change at the UME.[39] The potential change induced by the NP collision events is typically big enough for the potentiometric method and no extra signal amplification method is needed. Therefore, it is simpler and suitable for many biological applications. In addition, the noise of the potentiometric method is smaller at the same bandwidth, allowing for higher sensitivity and faster detection. Although all of these

advantages, the potentiometric method is still rarely used in single-entity studies and thus worth to be further explored.

We are motivated to integrate two promising single-entity electrochemistry techniques, the nanopore technique and the potentiometric based nano-impact technique, together to study NPs simultaneously. The quartz nanopipette can be an extremely versatile platform to integrate both methods. We have shown that a nanopore-carbon nanoelectrode (CNE) nanopipette can detect both the ionic current and open-circuit potential changes induced by the transport and translocation of individual gold NPs (GNPs) or polystyrene NPs (PS NPs) when they approach and pass through the nanopore.[40, 41] However, NP collision events at the CNE are rarely observed in previous studies, thus they have not been investigated by using the new approach by nanopore-nanoelectrode nanopipette. To enable the nanopore-nanoelectrode nanopipette based multifunctional NP detection, it is important to develop new approaches to generate and detect NP-CNE collision events using the CNE of the nanopipette.

In this report, we demonstrate that continuous NP-CNE collision events can also be generated under the proper condition. Previously, we have demonstrated that the alternating current dielectrophoresis (AC DEP) can be applied to effectively accumulate the NP near the nanopore and enhance throughput for the NP translocation measurement.[40] Here, the NPs are steered preferentially towards the CNE side. After trapping, a large fraction of pre-concentrated NPs collides at the CNE, instead of translocating through the nanopore. Thus, the NP-CNE collision signals dominate the observed signal. The recorded potential signal suggest that, the motion pattern of GNP is

different from PS NP in the collision events at the CNE. Such difference is distinct in the potential change signal, which can be used to separate the GNPs from the PS NPs in real-time even in a concentrated NP mixture.

4.2: Experimental Methods

The experimental methods used to accomplish this project are described in Chapter 2. Section 2.1 and its subsections provide an overview of multi-functional nanopipette fabrication and its electrical/optical characterization. Section 2.2 and its subsections describe the electrochemical measurements, dielectrophoretic enrichment of nanoparticles, darkfield microscopy, data collection and analysis, DEP methods are also presented in subsections 2.2. The reagents and solutions used in the project are described in the subsection below.

4.2.1 Materials and Reagents

ACS grade chemicals (e.g., Phosphate Buffer Saline (PBS) for pH 7.3-7.5) were purchased from Fisher Scientific and used without any further purification. For 10 mM PBS solution, the phosphate concentration is about 0.8 mM and the NaCl concentration is about 9.1 mM. The ionic strength of the 10 mM PBS solution is about 11.4 mM. The spherical shape 26 nm and 60 nm carboxyl functionalized PS NPs were purchased from Bangs Laboratory, Inc. and the spherical shape 10 nm and 40 nm GNPs were bought from BBI Solutions. The size and shape of the purchased NPs have been verified by scanning electron microscope (SEM), dynamic light scattering (DLS) and UV-Vis spectroscopy (for GNPs only). Redox molecule Hexaaminеruthenium (III) chloride [Ru (NH3)6Cl3] (98% pure) was purchased

from Sigma-Aldrich. All solutions were prepared using DI water (~18 MΩ) (Ultra Purelab System, ELGA/Siemens).

4.3: Results and Discussions

4.3.1 Detecting Single-NP Collision Events

The nanopore-CNE nanopipette used in the experiment has a long-taper geometry with the nanopore diameter in the range of 50-90 nm. The average effective surface area of the CNE is 0.42 μm^2. Systematic measurements have been carried out using 7 nanopipettes (see Chapter 2 section 2.2.1) and both insulating PS NPs and conductive GNPs.

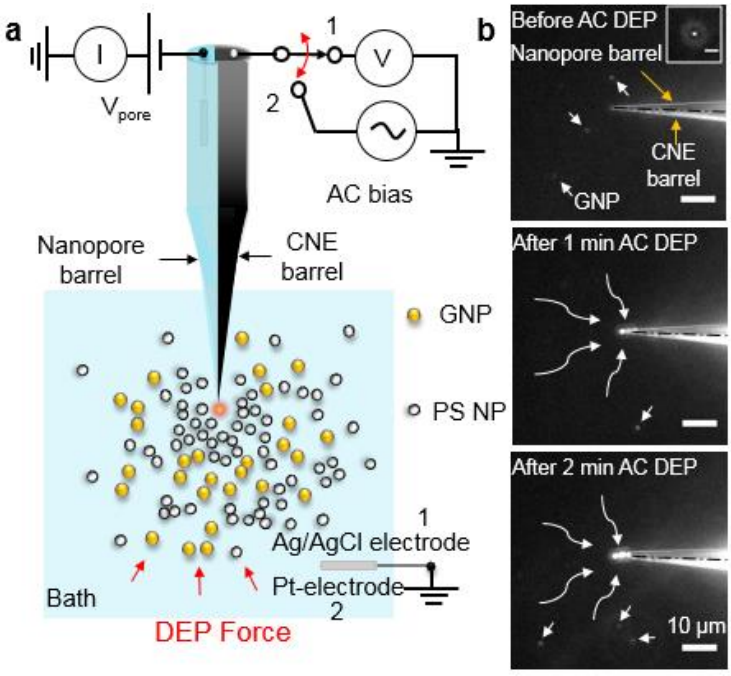

Figure 4.1: (a) The schematic experimental setup (not to scale). V_{pore} is the applied bias. The AC bias source and Pt-electrode are for AC DEP trapping purpose. (b) DFM images of GNPs accumulation near the nanopipette apex by AC DEP. The black dash lines represent the middle separation between two barrels. The bright dots indicated by white arrows are GNPs. The zoom-in of one dot is shown in the inset (the scale bar is 4 μm). The curved white arrows indicate the motion of GNPs towards the nanopipette apex.

From the DLS based zeta potential measurements in 10 mM PBS, the zeta potentials of the 26 nm and 60 nm PS NP are found to be -47.4 ± 3.6 mV and -56.3 ± 4.4 mV respectively. Similarly, -20.2 ± 4.5 mV and -34.2 ± 5.1 mV are the zeta potentials for 10 nm and 40 nm GNP respectively. The error is the standard deviation of 5 measurements.

The schematic of the experimental setup is shown in Figure 4.1a. Before adding NPs in the bath solution, both *i-t* and *V-t* time traces are featureless and very stable. After adding NPs, current and potential changes appeared in the traces, indicating that single-NP events happened at the apex. With both nanopore and nanoelectrode at the nanopipette apex, the NPs can interact with the tip in different ways, including translocation through the nanopore, collision at the nanopore orifice sidewall, and collision at the nanoelectrode. However, as a result of the large electrostatic repulsion forces from the negatively charged long-taper nanopipette tip, the events rate of these events is low under V_{pore}. Especially, the NP-CNE collision event is rarely observed. Following previous reports,[40, 42-44] we employed DEP to boost the event rate (see Experimental Section). The AC bias on the CNE effectively concentrates the NPs near the nanopipette tip [44, 45] and triggers continuous translocation or collision events of individual NPs at a high event rate. We found that the AC DEP application time is critical for producing different types of NP events. A short AC DEP trapping time between 30 sec to 1 min often produces translocation events or collision events at the nanopore circumference.[40] By slightly increasing the AC DEP time to 1-3 minutes, collision events at the CNE dominate. The observed event rate increased at least 30 times after AC DEP and up to a few thousands of collision events can be observed in 20-35 minutes.

To better understand the accumulation of NPs by the AC DEP forces and the following NP-CNE collision events, we monitored these processes by using the DFM microscope (see Chapter 2 sections 2.2.4 and 2.2.5). The representative DFM videos are shown in supporting information of the online version of the article.[1] Without AC DEP, the NPs move slowly in random Brownian motion. Occasionally, an NP speeds up and collides with the apex when it wanders the vicinity of the apex. Upon applying AC DEP, all the NPs in the field of view speed up and move towards the CNE. Similar results have been observed for all NPs. However, the speeds of the PS NPs under the same AC DEP condition are noticeably slower because of their lower polarizability.

Figure 4.1b shows three sequential DFM snapshots when applying AC DEP forces to trap 40 nm GNPs. The accumulated NPs appear as a bright blob near the nanopipette apex. With the increase of AC DEP trapping time, the size and brightness of the 'blob' increase rapidly, indicating the efficient accumulation of NPs from solution to the nanopipette apex. Although the blob size increased continuously with the AC DEP trapping time, the NP trapping efficiency gradually drops. At the first 30 s of the AC DEP trapping time, the NPs move very fast towards the apex. Thereafter, the speed of NP is greatly reduced and a big fraction of GNPs are scattered away from the tip apex before reaching and joining the 'blob'. With the increased number of accumulated NPs near the apex, the electrostatic repulsive force is increased and the DEP force is likely reduced as a result of screening by the accumulated NPs. Interestingly, the baseline of *i-t* trace is unaltered by the NP accumulation. In contrast, the baseline of *V-t* trace descends dramatically (more negative) with the presence of 'blob'. This suggests that the DEP force steers the NPs closer to the

CNE side, without affecting the ion flux through the nanopore. This is consistent with the observation that the position of 'blob' is shifted to the CNE side with the increase of AC DEP time (Figure 4.1(b) and Chapter 2 section 2.2.5).

It is worth mentioning that the small size of CNE further enhances the NP trapping efficiency. We have tested CNEs with effective radii ranging from ~20 nm to ~410 nm. Revealed by the DFM, the CNEs with smaller radii, *i.e.*, radius <100 nm, consistently show a higher trapping efficiency than the bigger ones. Because of the small size of CNE, we can effectively trap NPs as small as 10 nm GNPs and 26 nm PS NPs in up to 20 mM PBS solution. In 30 mM PBS solution, we hardly see any directional movement of NPs towards the CNE because the weaker AC DEP force cannot overcome other opposing factors, including electrostatic force, entropy cost, concentration gradient, and electrothermal flow.[43]

After AC DEP trapping, the 'blob' gradually reduces in size and brightness but remains distinguishable near the nanopipette tip for more than 30 minutes. The size reduction of blob happens slowly and smoothly, no dramatic changes are observed in the DFM images. Meanwhile, electrochemical signals of individual NP-CNE collision events appear at a high event rate. Therefore, the recorded collision events in *i-t* and *V-t* traces are from the NPs within the blob. The NPs at the inner frontier of the blob are highly dynamic and collide with the CNE continuously.

4.3.2: Detecting Single-NP Collision Events in a Crowded Environment.

Now we describe the electrochemical recordings of NP collision events at the CNE. We can tell if the signals are from the NP translocation events through the nanopore, the NP

collision events at the nanopore circumference during translocation, or the NP-CNE collision events, using the current changes in the simultaneously recorded *i-t* traces. A typical NP-CNE collision event induces obvious potential changes of CNE but no or very small current changes of the nanopore. Comprehensive studies have been carried out by two nanopipettes P2 and P4 (see chapter 2 section 2.2.1). We compare the potential changes induced by single-NP collision events at the CNE surface in a crowded environment between PS NPs and GNPs. Although translocation events still appear from time to time in the recorded data (see Figure 4.2), we only discuss the collision events at the CNE surface.

Figure 4.3(a) shows the event rate (/s) and potential baseline change as a function of time for 60 nm PS NPs in the first 35 minutes following the AC DEP trapping. From the Nernst equation, the overall potential baseline change reflects the local NP concentration change near the CNE, which is the collective contribution from all the NPs nearby. In the first 10 minutes, the potential baseline continued to drop. However, the individual collision event is rarely detected. Therefore, the concentrated NP assembly slowly moves toward the CNE driven by V_{pore}. Between 10-30 minutes, multiple peaks appear in the event rate plot. The arrival of accumulated NPs triggers continuous single-NP collision events. Without pre-accumulating NPs, we rarely observe these events even at a large V_{pore}. Therefore, the increased local NP concentration gradient and the electrostatic repulsion between NPs should be the leading causes for the increased NP-CNE collision events. Indeed, we found that the maxima event rate is mainly determined by the AC DEP trapping time, but not by the V_{pore} after the trapping. The shape of the transient potential change signal is also

strongly correlated to the event which also reflects the real-time NP concentration close to the potential sensing zone of CNE. Because of the varying event rate, the effect of V_{pore} to the shape of potential signals is uncertain and inconclusive.

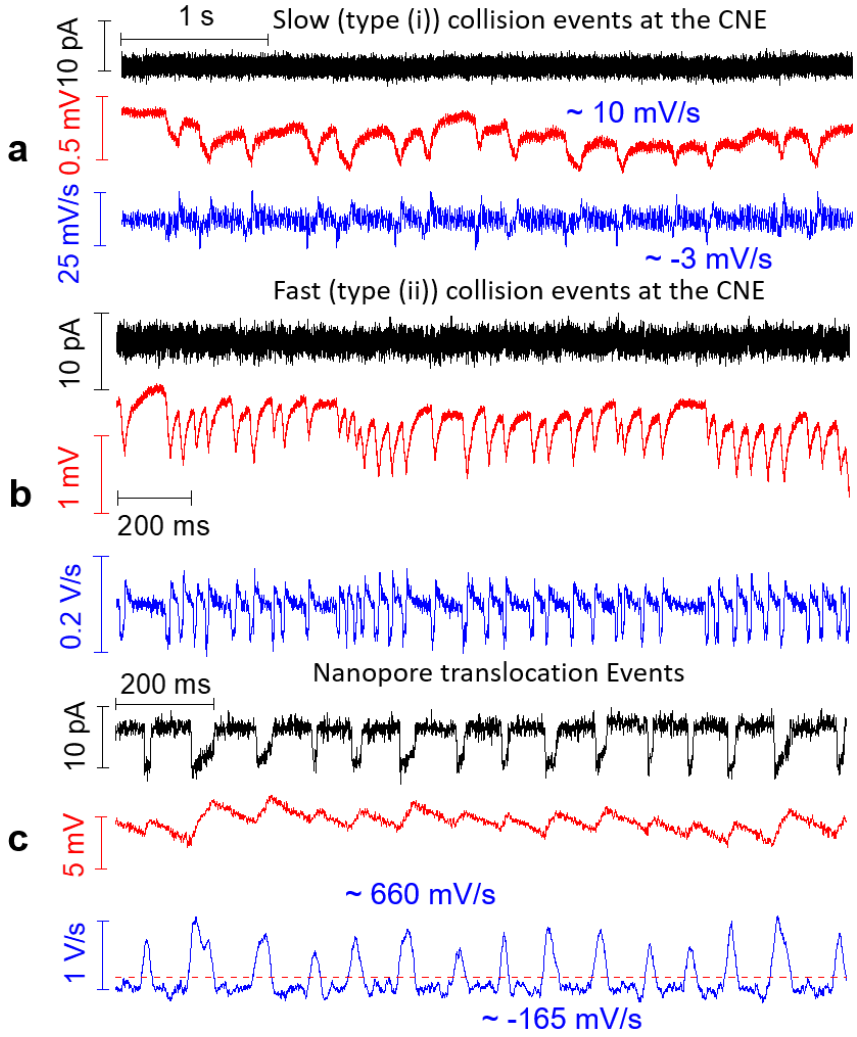

Figure 4.2: The time traces of current (black color), potential (red color), and the first derivative of potential (blue color) of 40 nm GNP collision events at the CNE at V_{pore} = 800 mV. Typical time traces show type (ii) (a) and type (i) (b) CNE-GNP collision events and (c) the nanopore translocation events. The concentration of 40 nm GNP was 10 pM in 10 mM PBS. For type (i) events, 10 ms (*i.e.*, 500 points) and for type (i) events 2 ms (*i.e.*, 100 points) smooth is used for dV/dt. The dV/dt magnitude revealed that the nanopore translocation is faster than collision at the CNE. We used the nanopipette P6 for this experiment and 3 minutes of AC DEP was applied before the measurement.

This is different from the translocation signals, where both current spikes and potential signals are affected by V_{pore}.[40]

Figure 4.3(b) presents the typical time traces for 60 nm PS NP near the maximum event rate (denoted by a red arrow in Figure 4.3(a)). More data can be found in the online version of the article Supplementary Figure S4 (a).[1] The baseline of *i-t* trace (the gray color trace) is stable and featureless, suggesting no translocation events. In contrast, continuous small potential dips appear in the *V-t* trace (the red color trace). Each potential dip represents an NP-CNE collision event. The potential dip features a gradual decrease (more negative) and then a sharp increase in potential. The black color dash line represents the baseline of the *V-t* trace. The potential baseline is usually stable but can become dramatically more negative and unstable when a big NP cluster moves toward the CNE as shown in the potential baseline plot in Figure 4.3(a). As indicated in the zoom-in trace, there are two types of potential dips, (i) and (ii), from their shapes. The comparison of the two is illustrated in Figure 4.3(c). In general, the approach time (t_A) is significantly longer (~5 times) than the rebounding time (t_R) for the type (i) dip. A flattened bottom (green shaded region) appears in type (i) dip, which is named waiting time (t_W). The duration time (t_d) of type (i) dip decreases with the increase of event rate (see Figure 4.4), mainly as a result of the decrease of t_W. For type (ii) dip, points 2 and 3 overlap and the t_W fully disappears. Compared with the shape of type (i) dip, the type (ii) dip has a shorter t_d and a smaller potential amplitude (ΔV). Therefore, the types (i) and (ii) dips are from the events with slow and fast approaching motions, respectively. The type (ii) dips appear only when the

event rate is high (typically > 2 for PS NP) and is rare when the event rate is low. Instead, type (i) dip dominates at low event rates but is still abundant at high event rates.

Figure 4.3(d) shows the statistical analysis of 1101 potential dips arose between 10 and 25 minutes. The histograms of t_d and ΔV are shown at the top and right sides of the t_d-ΔV scatter plot, respectively. Two peaks appear in both histograms, attributing to types (i) and (ii) potential dips. The mean t_d and ΔV of the type (i) potential dip are about 98.8 ± 49.6 ms and 1.14 ± 0.65 mV, respectively. The mean t_d and ΔV of the type (ii) potential dip are about 25.4 ± 6.7 ms and 0.56 ± 0.20 mV, respectively. Because the measured ΔVs is much smaller than the measured zeta potential of 60 nm PS NP, the PS NP should be still at some distance away from the CNE surface during the collision. Only the double layer of the PS NP overlaps with the double layer of the CNE.

As illustrated in Figure 4.3(e), in a typical type (i) potential dip (also see Figures 4.3(b) and 4.3(c)), a 60 nm PS NP enters the potential sensing zone of the CNE at time point 1. As the NP moves closer to the CNE, the potential of CNE decreases gradually to become more negative. The decrease of potential is as a result of the negative charge carried by the PS NP.[41] Because of charge screening, the detected potential change is exponentially dependent on the distance between the NP and the CNE surface. From points 2 to 3, the potential amplitude remains approximately the same which suggests that the NP stops and stays near the closest distance to the CNE. At point 3, the potential quickly jumps back, indicating the PS NP bounces back. At point 4, the potential returns to its baseline, and the NP should move out of the CNE sensing zone at this time.

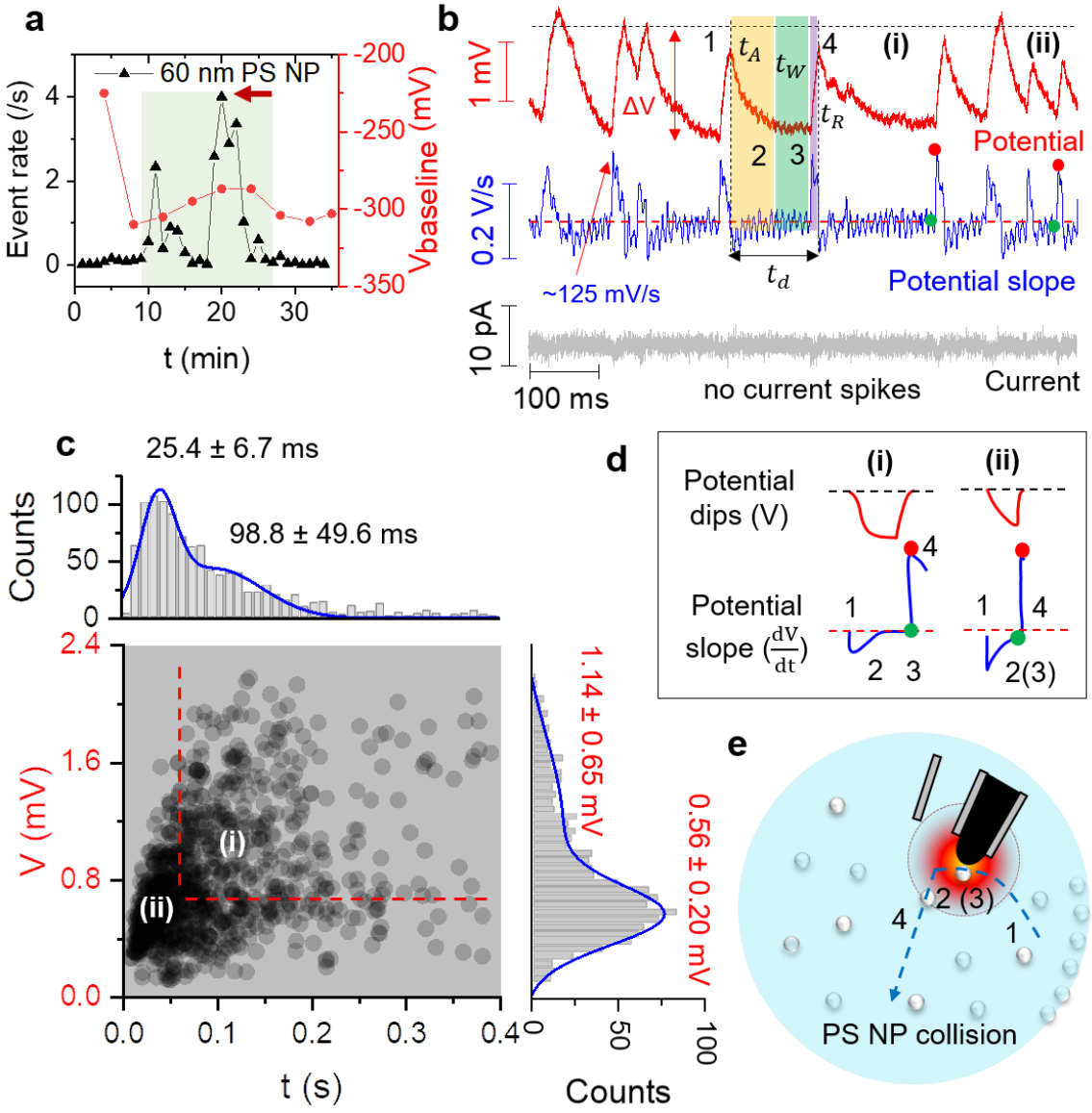

Figure 4.3: NP-CNE collision events of 60 nm PS NP in a crowded environment. (a) The collision event rate and potential baseline as a function of time resulted from N = 1289 collision events after AC DEP trapping. Each event rate and $V_{baseline}$ points are averaged over 1-minute and 4-min data, respectively. (b) Current (gray), Potential (red) and derivative of potential (dV/dt) (blue) time traces at V_{pore} = 200 mV and about 20 minutes (denoted by the red arrow in (a)) after AC DEP trapping. Slow and fast events are labelled as type (i) and (ii) respectively. The t_d is divided into t_A, t_W, and t_R. ΔV denotes the amplitude of the potential dip. (c) Schematic of the shapes of potential dips and their derivatives for types (i) and (ii) events. (d) The scatter plot and histograms of t_d and ΔV for N = 1101 collision events. Dashed lines in the scatter plot separate types (i) and (ii) events. Solid lines in the histograms are two-peak Gaussian fits. (e) A schematic to show the type (i) event in four steps. The dashed line denotes the motion trajectory of the PS NP. The red region indicates the potential sensing zone of CNE.

The time trace of the first derivative of potential (dV/dt) (blue color trace) can qualitatively reveal the NP speed during the collision motion. A higher dV/dt value indicates a larger speed. A negative (positive) dV/dt value indicates the forward (backward) motion to (from) the CNE. A large positive dV/dt value peaks at ~125 mV/s during t_R, suggesting the fast rebounding speed of the PS NP from the CNE. In contrast, the negative dV/dt value is very small (~-11 mV/s) during approaching (t_A) and becomes almost zero during t_W. The retardation of the PS NP as it approaches the CNE can be attributed to the hindered diffusion[46] and the increased electrostatic repulsion between the negatively charged NP and CNE surface. It is intriguing for the appearance of waiting time in the type (i) dip. The NP is likely transiently trapped near the CNE surface under a delicate and dynamic balance between all the forces.

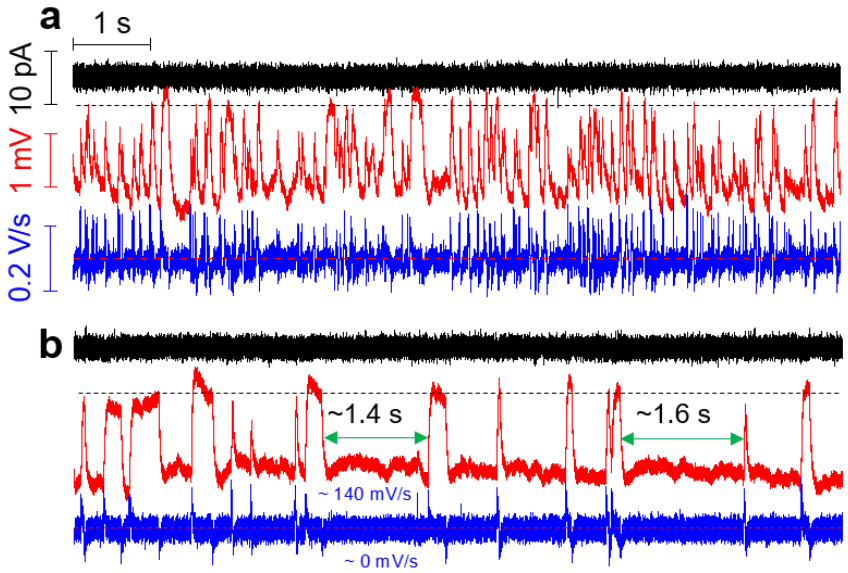

Figure 4.4: The time traces of current (black), potential (red), and the first derivative of potential (blue) of 60 nm PS NP collision to the CNE at V_{pore} = 200 mV. (a) 20 minutes After the AC DEP when the event rate is high. (b) 25 minutes after the AC DEP when the event rate is much lower. The waiting time (t_W), denoted by green arrows, is obvious in many potential dips and its magnitude varies from few milliseconds to 1.6 s. We used the nanopipette P2 for this experiment and an AC DEP was applied for 2 minutes. The concentration of 60 nm PS NP in 10 mM PBS is 100 pM.

The sudden bouncing back of NP can be triggered by thermal fluctuation or the influence of other NPs. At the high event rate, another potential dip always appears immediately after point 4 in the V-t trace. Therefore, the approach of the second NP should be mainly responsible for the release of the trapped one when the event rate is high. At a low event rate (see Figure 4.4), we sometimes observed the potential value returns to the baseline at point 4 after a long t_W (more than 1.6 s). In such an event, the trapped NP may only escape as a result of thermal fluctuations.

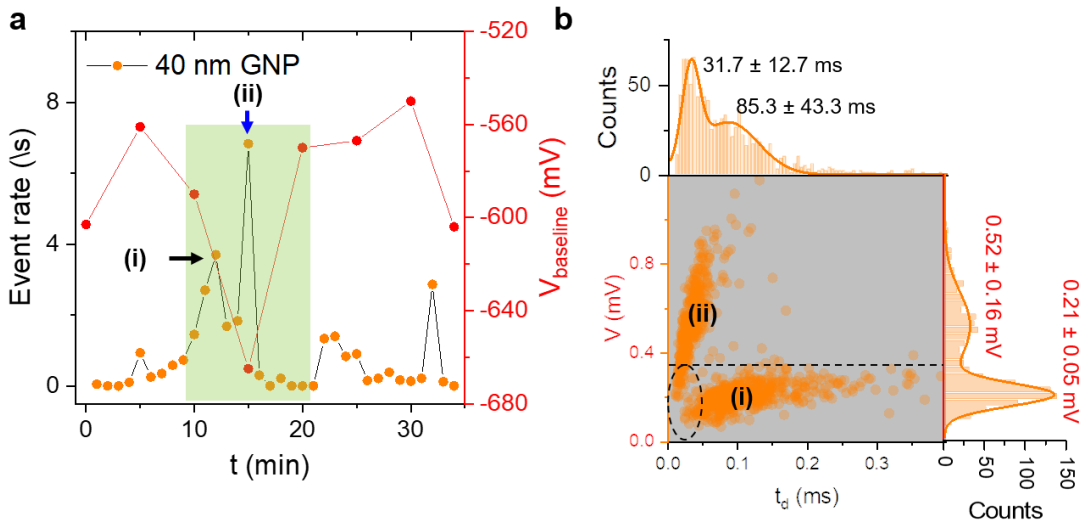

Figure 4.5: (a) The collision event rate and potential baseline as a function of time. About 1819 collisions are counted in 35 minutes after AC DEP trapping. Each event rate and potential baseline points are averaged over 1-minute and 4-minute data, respectively. Blue and Black arrows denote the event rates at which two type events dominate. (b) t_d-ΔV scatter plot for 1009 collision events collected from the green shaded region in (a). Type (i) dips are shown in (a) of Figure S5b and typical type (ii) dips are shown in (b) of Figure S5b. Dashed straight line in the scatter plot separate two types of dips. Dashed oval denotes the events at the transition phase (*i.e.*, from type (i) to type (ii)).

For comparison, we also investigated the collision events by polarizable GNPs. Figure 4.5 shows the collision event rate (/s) and potential baseline as a function of time for 40 nm GNPs in the first 35 minutes following AC DEP trapping. The event rate peak at ~6.5

(events/s) appears between 10-20 minutes. Compared with the plot in Figure 4.3 (a), the higher peak value of GNPs suggests the density of accumulated GNP assembly is higher at the same DEP trapping condition. This is also supported by the significant drop in the potential baseline at the same time.

Figure 4.6(a) shows the typical results of 40 nm GNP collision events at the CNE near the highest event rate. Statistical analysis of 1009 GNP potential dips collected between 10 and 20 minutes is shown in Figure 4.5. Two well-separated data sets appear in the t_d-ΔV scatter plot. Same as the results of PS NP, we attribute the two data sets to types (i) and (ii) potential dips. The general features of both types are illustrated in the inset of Figure 4.6(b). The type (i) dips (see Figure 4.2), mainly appear at low event rates (typically <3 for GNP). They are from the GNPs with slow approaching motions. In contrast, the type (ii) dips, as shown in Figure 4.6(a), dominate the signal when the event rate is high (typically >3 for GNP). They are from the GNPs with fast approaching motions. For type (ii) dips, the approaching time t_A is short, with almost no retardation during approaching and no t_W. However, it is interesting to note the obvious retardation appears during the rebounding of GNP, which may be attributed to the stronger repulsion by the denser GNP assembly nearby. It should be noted that the shape characteristics of type (ii) dip remain the same at lower V_{pore}, *i.e.,* at zero bias (see Figure 4.7). Therefore, the fast approaching motion of GNP is mainly driven by the high local GNP concentration.

Now we investigate the first derivative of potential dips. In Figure 4.6(a), the dV/dt of the type (ii) dip has a bigger negative peak value (~ -95 mV/s at the green dot) and a smaller

positive peak value (~ +68 mV/s at the red dot). Both the positive and negative dV/dt peak values are similar for most of the events.

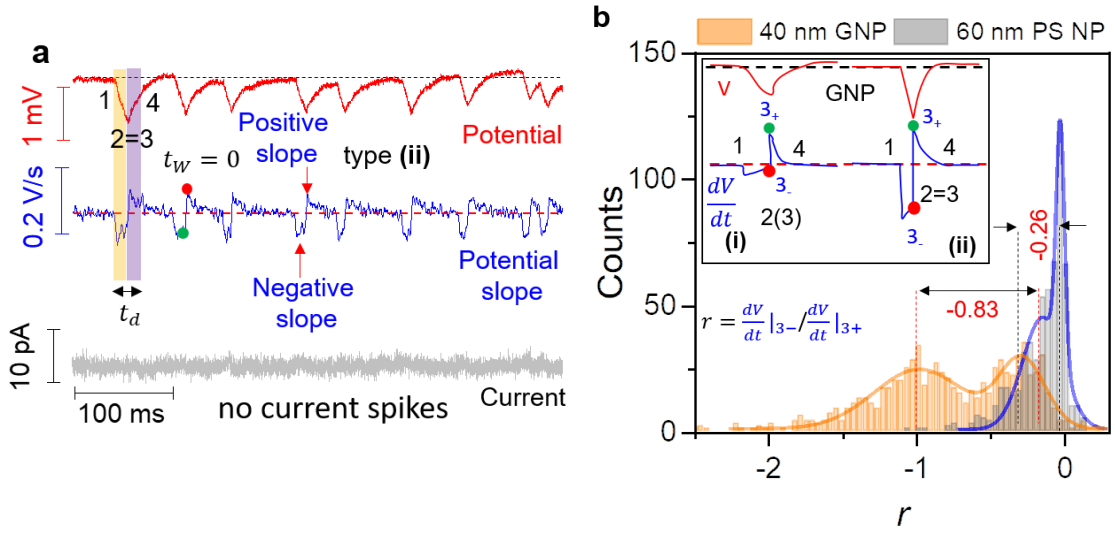

Figure 4. 6: The NP-CNE collision events of 40 nm GNP in a crowded environment. (a) Typical current (gray), potential (red), and the first derivative of potential (blue) time traces. The data are collected when V_{pore} = 800 mV is applied. (b) The histograms of *r* for PS NP (N = 586) and GNPs (N = 788) with Gaussian fits (solid lines). Inset illustrates of shapes of types (i) and (ii) potential dips of GNP and their derivatives. Parameter *r* is defined using dV/dt peaks. Green and red dots denote the dV/dt value just before (*i.e.,* at 3_-) and after (*i.e.,* at 3_+) the point 3.

The relatively small positive dV/dt peak also reflects the retardation during GNP rebounding. The negative dV/dt peak is close to a rectangular shape, which reflects the uniform approaching speed. The retardation is very small when GNP approaching the CNE surface, which is very different from the approaching behavior of the PS NP. The origin of this difference is attributed to the different polarizability, leading to the faster motion of the GNP. When the event rate is low, the approaching speed of GNP is noticeably reduced. As shown in Figure 4.7b and Figure 4.6(b) inset, the negative dV/dt peak of type (i) dip is much smaller and the retardation during approach is also observed, leading to a triangle type negative dV/dt peak.

As illustrated in Figures 4.3(c) and 4.6(b) inset, the differences in the collision motions of the PS NP and GNP are reflected in the shapes of potential dips and their time derivatives. These differences can be employed to differentiate NPs. To quantify the differences, we define a dimensionless parameter *r*. As shown in Figure 4.6(b), *r* is the ratio between the dV/dt values at the base and peak of the positive dV/dt peak near point 3 (which is the turning point from the approaching motion to rebounding motion), indicated by the green and red dots. In other words, *r* is the ratio of the potential slopes right before (3_-) and after (3_+) the point 3. A bigger *r* value reflects the higher approaching speed of the NP and vice-versa. For PS NP, because the approaching motion is slowed down (for type (ii) dip) or fully stopped (for type (i) dip), the $dV/dt|_{3-}$ value is approximately zero. Therefore, *r* for PS NP is very small for both types of dips. In contrast, because the retardation is not obvious in GNP approaching motion for both types of dips, the $dV/dt|_{3-}$ is relatively bigger, resulting in larger *r*.

The histograms of *r* for both 60 nm PS NP and 40 nm GNP collision events are shown in Figure 4.6(b). The mean values of *r* for 60 nm PS NPs are -0.02 ± 0.03 for the peak and -0.14 ± 0.13 for the shoulder. The almost zero peak value reflects the severe retardation or transiently trapped state of the PS NP near the CNE during the approach. The shoulder is contributed by a fraction of type (ii) fast events with less retardation. Two well-separated peaks appear in the histogram of *r* for 40 nm GNP. The two peaks are at -0.97 ± 0.31 and -0.28 ± 0.15, from fast type (ii) dips (mainly appear at high event rates) and slow type (i)

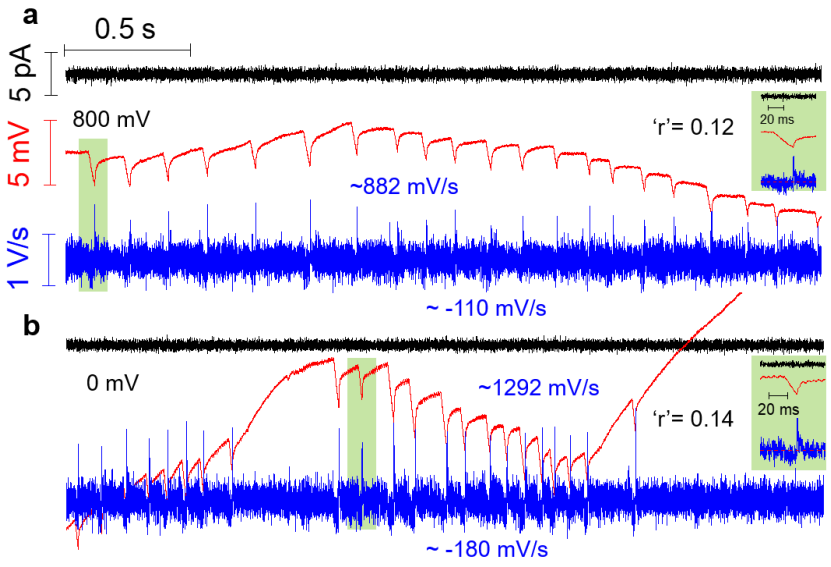

Figure 4. 7: Current (black) and potential (red) and derivative of potential (dV/dt) time traces showing the NP-CNE collision events of 40 nm GNPs. Nanopipette P1 was used to acquire these time traces at V_{pore} = 800 mV (a) and V_{pore} = 0 mV (b). The nanopore bias has no obvious effect on the shape of the potential dips. 10 pM GNP was used in the experiment.

dips (appear at low event rates), respectively. The difference of *r* between two types of NPs is much bigger (0.83) for fast events (type (ii)) at high event rates, suggesting we can differentiate the NPs in a crowded environment just from *r*.

4.2.3: Real-Time Discrimination of GNP and PS NP in a Mixture.

To further demonstrate the capability of differentiating metallic and insulating NPs in aqueous solutions using potentiometric measurement of the NP-CNE collisions, a mixture sample of 40 nm GNP and 26 nm PS NP in 1:5 molar concentration ratio (10 pM vs. 50 pM) was used. We used a lower GNP concentration in the mixture because of a higher trapping efficiency for the GNPs than for the PS NPs. The nanopipette P1 was used to acquire the results.

The cumulative collision event rate (/s) (produced by both NPs) and potential baseline as a function of time are displayed in Figure 4.8(a). 1-min of AC DEP was first applied to produce 30-min of data. Then 3-min of AC DEP trapping is applied again to generate more collision events in the following ~35 minutes. The collision event rate becomes significantly higher following the second AC DEP application. Accordingly, the potential baseline drops around 10 minutes and drops further around 35 minutes. The baseline returns around 70 minutes, suggesting the almost full dissipation of the NP accumulations. About 7000 total collision events are observed in the experiment. As we will show later, the PS NP and GNP signals can be distinguished from the shape of potential dip and the corresponding dV/dt peaks. The GNPs generate about 49% collision signals and the PS NPs generate the rest. This percentage is very different from the initial ~16.7% of GNPs in the mixture. The significant percentage change confirms the bigger DEP force experienced by the GNPs in the solution.

Multi-peak features are obvious in the event rate plot in Figure 4.8 (a). Therefore, the density of accumulated NP mixtures near the nanopipette apex is heterogeneous. Interestingly, the PS NPs and GNPs always separate from each other to form their clusters (see Figure 4.9). Even at a low event rate (<3 for mixture), the NPs of the same type like to form small clusters. The detected GNP cluster size varied from 2 to ~9 particles at a low event rate and 12 to ~720 particles at high event rates. In contrast, the cluster size for the PS NPs ranged from 6 to ~9 at a low event rate and 6 to ~66 at high event rates.

Figure 4.8(b) shows the data at the low event rate ~3 events/min (indicated by the light red shaded region in Figure 4.8(a)). Two different types of potential dips are observed in the

V-t trace corresponding to PS NP and GNP collision events. Different from the pure NP sample, the events in the mixture appear in small clusters and the shapes of dips in a cluster are similar. From the shapes of potential dips and their first derivatives, the signals from 26 nm PS NP are indicated by a light gray bar, and from 40 nm GNP are indicated by a light-yellow bar. The t_d of the GNP-CNE collision event is much shorter than the PS NP-CNE collision event. Using the shapes of these dips, they are type (ii) dips of PS NPs and GNPs. This is surprising, considering that type (ii) dips only appear at high event rates in pure NP samples. The small cluster form likely speeds up the motion of individual NPs because of the stronger inter-particle interaction in a cluster. As we discussed for the pure PS NP sample, at a low event rate, the slower PS can be trapped near the CNE. Here, t_W does not show up in the clustered potential dips of PS NPs. The t_W is only obvious in the last collision event of a PS NP cluster and before the arrival of a GNP cluster. This also reflects a smaller inter-particle distance and a bigger inter-cluster distance. Also, both the positive and negative dV/dt peaks are higher. So the motion of individual PS NP in a cluster is much faster even at a low event rate.

We further analyzed the ratio *r* for the potential dips of both NPs at low event rates. The histogram of *r* is shown in Figure 4.8(c). Two peaks are well-separated. The left peak is from GNP and the right peak is from PS NP. It is apparent from the histogram that more than 95% of the PS NP collision events have an *r* value more positive than -0.1. $r = -0.1$ can be used as a parameter to separate two types of NPs using the recorded potential dips. Compared with the histograms in Figure 4.6(b), the mean *r* value for type (ii) dips of GNPs reduces about 65%, which is attributed to the relatively high rebounding speed. This

difference suggests that the NP-CNE collision event is strongly affected by the cluster formation in the NP mixture.

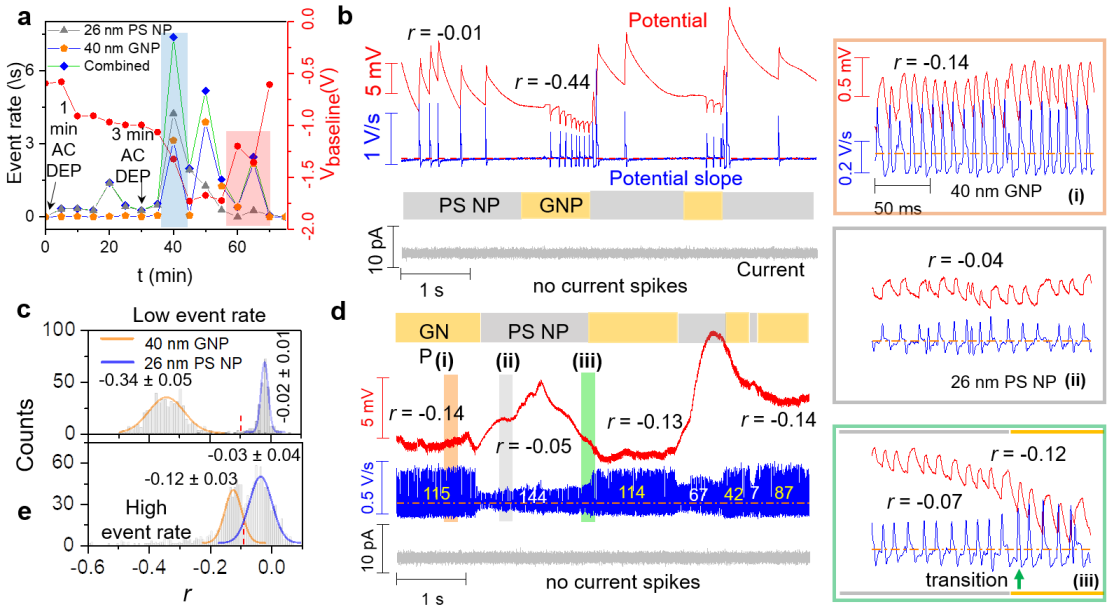

Figure 4. 8: NP-CNE collision events of a mixture of 40 nm GNP and 26 nm PS NP. (a) Single-NP collision event rate and $V_{baseline}$ (red) as a function of time from N = 6791 events in about 75 minutes after AC DEP trapping. The event rate and $V_{baseline}$ data points are averaged over 5 minutes. The light red and blue shaded regions denote the time window at which collision events are shown in (b) and (d) occurred, respectively. (b) I (gray), V (red) and dV/dt (blue) time traces at V_{pore} = 800 mV. The dV/dt trace is smoothed with a moving average window of 0.4 ms. (c) The histogram of *r* collected at low event rates for PS NPs (N = 252) and GNPs (N = 523). (d) NP collision events at high event rates. The numbers on the dV/dt time trace denote the number of collision events. At the right panel, the zoom-in of regions (i) and (ii) are of GNPs and PS NPs collisions respectively. Region (iii) is where the transition from PS NP to GNPs collision occurs. A green arrow denotes the transition point. (e) The histograms of *r* at the high event rates (N = 1201 combined).

Figure 4.8(d) presents the typical data at a high event rate, as indicated by the light blue shaded region in Figure 4.8(a). The potential baseline fluctuates significantly, which is mainly as a result of the arrival and departure of large GNP clusters near the CNE. The change induced by PS NP cluster is much smaller and is overshadowed by the neighboring GNP cluster movement. Considering the slightly bigger surface potential of 26 nm PS NP,

the difference stems from the different cluster structures.[40] The GNP cluster is highly compact with a higher volume charge density and thus has a larger impact on the CNE potential. Along with the potential baseline change, the clustered potential dips from GNP and PS NP collision events appeared alternately. Compared with the data at low event rates in Figure 4.8(b), the cluster size here is much bigger.

Three zoom-in time traces are shown at the right panel of Figure 4.8(d). The potential dips of GNPs (trace (i)) appear much denser (~125 dips/s) than the dips of PS NP (~90 dips/s) (trace (ii)). These dips are also like type (ii) dips of pure GNP samples. The dV/dt peaks of GNPs are uniform in shape, reflecting the ordered GNP cluster structure. In contrast, it is less uniform for PS NPs. Both types (i) and (ii) dips appear in the trace. The retardation is obvious in the approaching motion of PS NP collision events. In addition, the potential dips of PS NP are affected by the neighboring GNP clusters, with varying dV/dt peak heights. Here, both positive and negative dV/dt peak heights are reduced compared with the peak heights at the low event rate (Figure 4.8(b)). The positive dV/dt peak amplitude is reduced by more than half. So the rebounding speed of the PS NP after the collision is also greatly hindered by the high local NP density.

Figure 4.8(e) presents the histogram of r of events at high event rates. The magnitude of r for GNP is further reduced. At high event rates, the approaching speed of GNP decreases more than its rebounding speed, leading to a smaller magnitude of r. In contrast, the magnitude of r for PS NP is slightly increased. As shown in zoom-in trace (iii), the approaching speed of PS NP is slightly faster with less retardation, affected by neighboring GNPs. The mean value of r for the GNPs and PS NPs collisions are -0.12 ± 0.03 and -0.03

± 0.04, respectively. Therefore, the separation of *r* values between the two types of NPs at high even rates is smaller than that at low even rates (Figure 4.8(d)). This is opposite to the change of *r* in pure NP sample (Figure 4.6(b)). The cluster formation of NP in a mixture altered the collision motion of individual NPs. It is important to note that over 90% of the *r*-value of the PS NPs collision is still more positive than ~-0.1. Thus, the condition *r* = -0.1 can still be applied to separate GNPs from PS NPs.

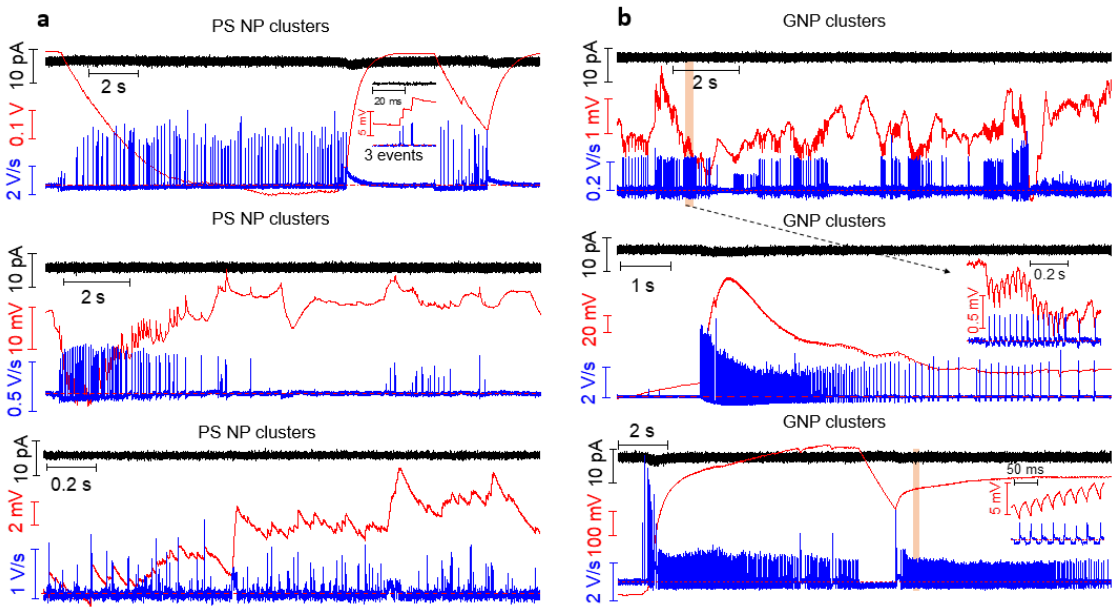

Figure 4. 9: The formation of the 26 nm PS NP and 40 nm GNP clusters. Current (black), potential (red), and the first derivative of potential (blue) time traces at V_{pore} = 800 mV. The three-time traces in (a) reveal the PS NP cluster formation. The inset in (a) shows the potential changes induced by a cluster of 3 PS NPs collision events at the CNE. The three-time traces in (b) reveal the GNP clusters formation. The insets show the zoom-in of the highlighted regions.

Finally, we should mention that the proximity of the nanopore next to the CNE demonstrates several advantages although nanopore is not directly used as the detector in the NP-CNE collision events. i) Right after AC trapping, the DC bias applied at the nanopore barrel helps to drive the accumulated NPs to move closer to nanoelectrode to trigger the continuous potentiometric detection of collision events by individual NPs at the

CNE. The V_{pore} also helps to retain the accumulated NPs and prevents them to move in random directions during measurements. ii) Surprisingly, few NP adsorption events are detected in these events. The contamination-free CNE surface is critical for long-time measurements. We speculate that the focused electric field and electroosmotic flow in/out of the nanopore likely prevent the NP to stay at the CNE surface. iii) The simultaneously recorded ionic current signal still provides important information regarding the type of NP events at the nanopipette apex.

4.4: Conclusions

In summary, we reported the effective generation and detection of single-NP collision events at the nanoelectrode in solutions using a nanopore-nanoelectrode nanopipette. By applying the AC DEP force through the CNE at the nanopipette apex, we can accumulate a large number of NPs near the CNE in a few minutes and produce NP-CNE collision events with a high event rate for tens of minutes. Between GNPs and PS NPs, the AC DEP trapping is most effective for GNPs. Using potentiometric measurements using the CNE, we reveal the key differences in the approaching motion between metallic and insulating NPs. The approaching motion of PS NP toward the CNE is slowed down or fully stopped near the CNE, resulting in a distinct change in transient potential change and its first derivative. The individual NP-CNE collision events induced potential changes can also be employed to differentiate the NPs in a mixture. As a result of different polarizability, the PS NPs and GNPs separate from each other and form clusters in the concentrated NP mixture. Structural information of these dynamic NP assembly structures can be probed. By integrating the nanopore and nanoelectrode based single-entity electrochemical

methods, we expect that the multifunctional nanopipettes have practical applications in biomedical, energy, and environmental studies.

4.5: References

1. Pandey, P., et al., *Differentiation of metallic and dielectric nanoparticles in solution by single-nanoparticle collision events at the nanoelectrode.* Nanotechnology, 2019. **31**(1): p. 015503.

2. Pandey, P. and J. He, *Nanopore-Nanoelectrode for Potential Sensing of Single Nanoparticle Collision Events.* Biophysical Journal, 2019. **116**(3): p. 444a-445a.

3. Wang, W. and N. Tao, *Detection, Counting, and Imaging of Single Nanoparticles.* Analytical Chemistry, 2014. **86**(1): p. 2-14.

4. Kleijn, S.E.F., et al., *Electrochemistry of Nanoparticles.* Angewandte Chemie International Edition, 2014. **53**(14): p. 3558-3586.

5. Dykman, L. and N. Khlebtsov, *Gold nanoparticles in biomedical applications: recent advances and perspectives.* Chemical Society Reviews, 2012. **41**(6): p. 2256-2282.

6. Wang, Y., X. Shan, and N. Tao, *Emerging tools for studying single entity electrochemistry.* Faraday Discussions, 2016. **193**(0): p. 9-39.

7. Baker, L.A., *Perspective and Prospectus on Single-Entity Electrochemistry.* Journal of the American Chemical Society, 2018. **140**(46): p. 15549-15559.

8. Howorka, S. and Z. Siwy, *Nanopore analytics: sensing of single molecules.* Chemical Society Reviews, 2009. **38**(8): p. 2360-2384.

9. Kasianowicz, J.J., et al., Proc. Natl. Acad. Sci. U.S.A., 1996. **93**: p. 13770.

10. Shi, W., A.K. Friedman, and L.A. Baker, *Nanopore Sensing.* Analytical Chemistry, 2017. **89**(1): p. 157-188.

11. Harrer, S., et al., *Label-free screening of single biomolecules through resistive pulse sensing technology for precision medicine applications.* Nanotechnology, 2015. **26**(18): p. 182502.

12. Lin, X., A.P. Ivanov, and J.B. Edel, *Selective single molecule nanopore sensing of proteins using DNA aptamer-functionalised gold nanoparticles.* Chemical Science, 2017. **8**(5): p. 3905-3912.

13. Steinbock, L.J., et al., *Detecting DNA folding with nanocapillaries.* Nano letters, 2010. **10**(7): p. 2493-2497.

14. Tiwari, P.B., et al., *Quantitative study of protein–protein interactions by quartz nanopipettes.* Nanoscale, 2014. **6**(17): p. 10255-10263.

15. Zhou, K., et al., *Characterization of Hepatitis B Virus Capsids by Resistive-Pulse Sensing.* Journal of the American Chemical Society, 2011. **133**(6): p. 1618-1621.

16. Sze, J.Y.Y., et al., *Fine tuning of nanopipettes using atomic layer deposition for single molecule sensing.* Analyst, 2015. **140**(14): p. 4828-4834.

17. Yusko, E.C., et al., *Real-time shape approximation and fingerprinting of single proteins using a nanopore.* Nature Nanotechnology, 2016. **12**: p. 360.

18. Qiu, Y., et al., *Role of Particle Focusing in Resistive-Pulse Technique: Direction-Dependent Velocity in Micropores.* ACS Nano, 2016. **10**(3): p. 3509-3517.

19. Terejánszky, P., et al., *Calibration-Less Sizing and Quantitation of Polymeric Nanoparticles and Viruses with Quartz Nanopipets.* Analytical Chemistry, 2014. **86**(10): p. 4688-4697.

20. Quinn, B.M., P.G. van't Hof, and S.G. Lemay, *Time-Resolved Electrochemical Detection of Discrete Adsorption Events.* Journal of the American Chemical Society, 2004. **126**(27): p. 8360-8361.

21. Xiao, X. and A.J. Bard, *Observing Single Nanoparticle Collisions at an Ultramicroelectrode by Electrocatalytic Amplification.* Journal of the American Chemical Society, 2007. **129**(31): p. 9610-9612.

22. Peng, Y.-Y., et al., *Stochastic Collision Nanoelectrochemistry: A Review of Recent Developments.* ChemElectroChem, 2017. **4**(5): p. 977-985.

23. McKelvey, K., et al., *Nanopipettes as a tool for single nanoparticle electrochemistry.* Current Opinion in Electrochemistry, 2017. **6**(1): p. 4-9.

24. Couto, R.A.S., et al., *Detection of Escherichia coli Bacteria by Impact Electrochemistry.* Analyst, 2018. **143**: p. 4840-4843.

25. Oja, S.M., M. Wood, and B. Zhang, *Nanoscale Electrochemistry.* Analytical Chemistry, 2013. **85**(2): p. 473-486.

26. Pumera, M., *Impact Electrochemistry: Measuring Individual Nanoparticles.* ACS Nano, 2014. **8**(8): p. 7555-7558.

27. Rees, N.V., *Electrochemical insight from nanoparticle collisions with electrodes: A mini-review.* Electrochemistry Communications, 2014. **43**: p. 83-86.

28. Anderson, T.J. and B. Zhang, *Single-Nanoparticle Electrochemistry through Immobilization and Collision.* Accounts of Chemical Research, 2016. **49**(11): p. 2625-2631.

29. McKelvey, K., et al., *Single Ag nanoparticle collisions within a dual-electrode micro-gap cell.* Faraday Discussions, 2018. **210**: p. 189-200.

30. Ma, W., et al., *Single Ag Nanoparticle Electro-oxidation: Potential-Dependent Current Traces and Potential-Independent Electron Transfer Kinetic.* The Journal of Physical Chemistry Letters, 2018. **9**(6): p. 1429-1433.

31. Chen, C.-H., et al., *Impact of Surface Chemistry on Nanoparticle–Electrode Interactions in the Electrochemical Detection of Nanoparticle Collisions.* Langmuir, 2015. **31**(43): p. 11932-11942.

32. Stuart, E.J.E., et al., *Electrochemical Observation of Single Collision Events: Fullerene Nanoparticles.* ACS Nano, 2014. **8**(8): p. 7648-7654.

33. Dasari, R., et al., *Electrochemical Monitoring of Single Nanoparticle Collisions at Mercury-Modified Platinum Ultramicroelectrodes.* ACS Nano, 2014. **8**(5): p. 4539-4546.

34. Zhou, Y.-G., et al., *Electrode-nanoparticle collisions: The measurement of the sticking coefficients of gold and nickel nanoparticles from aqueous solution onto a carbon electrode.* Chemical Physics Letters, 2012. **551**: p. 68-71.

35. McKelvey, K., M.A. Edwards, and H.S. White, *Resistive Pulse Delivery of Single Nanoparticles to Electrochemical Interfaces.* The Journal of Physical Chemistry Letters, 2016. **7**(19): p. 3920-3924.

36. Kang, M., et al., *Time-Resolved Detection and Analysis of Single Nanoparticle Electrocatalytic Impacts*. Journal of the American Chemical Society, 2015. **137**(34): p. 10902-10905.

37. Zhou, M., et al., *Collisions of Ir Oxide Nanoparticles with Carbon Nanopipettes: Experiments with One Nanoparticle.* Analytical Chemistry, 2017. **89**(5): p. 2880-2885.

38. Kleijn, S.E.F., et al., *Landing and Catalytic Characterization of Individual Nanoparticles on Electrode Surfaces.* Journal of the American Chemical Society, 2012. **134**(45): p. 18558-18561.

39. Zhou, H., et al., *Observation of Single Metal Nanoparticle Collisions by Open Circuit (Mixed) Potential Changes at an Ultramicroelectrode.* Journal of the American Chemical Society, 2012. **134**(32): p. 13212-13215.

40. Pandey, P., et al., *Probing Dynamic Events of Dielectric Nanoparticles by a Nanoelectrode-Nanopore Nanopipette.* ChemElectroChem, 2018. **5**(20): p. 3102-3112.

41. Panday, N., et al., *Simultaneous Ionic Current and Potential Detection of Nanoparticles by a Multifunctional Nanopipette.* ACS Nano, 2016. **10**(12): p. 11237-11248.

42. Tanaka, S., et al., *Tailoring particle translocation via dielectrophoresis in pore channels.* Scientific Reports, 2016. **6**: p. 31670.

43. Freedman, K.J., et al., *Nanopore sensing at ultra-low concentrations using single-molecule dielectrophoretic trapping.* Nature communications, 2016. **7**: p. 10217.

44. Freedman, K.J., et al., *On-Demand Surface- and Tip-Enhanced Raman Spectroscopy Using Dielectrophoretic Trapping and Nanopore Sensing.* ACS Photonics, 2016. **3**(6): p. 1036-1044.

45. Chen, D., H. Du, and C. Tay, *Rapid Concentration of Nanoparticles with DC Dielectrophoresis in Focused Electric Fields.* Nanoscale Research Letters, 2010. **5**(1): p. 55-60.

46. Eloul, S. and R.G. Compton, *General Model of Hindered Diffusion.* The Journal of Physical Chemistry Letters, 2016. **7**(21): p. 4317-4321.

CHAPTER 5: SINGLE-ENTITY APPROACH TO INVESTIGATE SURFACE CHARGE ENHANCEMENT IN MAGNETOELECTRIC NANOPARTICLES INDUCED BY AC MAGNETIC FIELD STIMULATION

Magneto-electric nanoparticles (MENPs), composed of a piezoelectric shell and a ferromagnetic core, exhibited enhanced cell-uptake and controlled drug release as a result of the enhanced localized electric field (surface charge/potential) and the generation of acoustics, respectively, upon applying alternating current (AC)-magnetic (B)-field stimulation. This research, for the first time, implements an electrochemical single-entity approach to probe AC B-field induced strain mediated surface potential enhancement on MENP surface. The surface potential changes at the single-NP level can be probed by the open circuit potential changes of the floating carbon nanoelectrode (CNE) during the MENP-CNE collision events. The results confirmed that the AC B-field (60 Oe) stimulation caused localized surface potential enhancement of MENP. This observation is associated with the presence of a piezoelectric shell whereas magnetic nanoparticles were found unaffected under identical stimulation. The contents in Chapter 5 are adapted from my recently published peer-reviewed article.[1]

5.1: Introduction

Contribution of stimuli-responsive smart multi-functional nano-systems in biomedical science is emerging to enable investigation of novel theranostics of desired performance.[2] Most of such nano-systems need external stimulation to exhibit desired performance. During the process of stimulation, these nano-systems showed altered intrinsic properties which may cause beneficial or adverse effects in biological systems. Among various stimuli-responsive nano-systems explored for biomedical applications,

magnetoelectric nanoparticles (MENPs) are emerging as a multi-functional multiferroic nano-system. The MENPs exhibited unique aspects suitable for biomedical science as a result of controllable coupling between magnetic and electronic properties.[3-5] This nano-system is a core-shell nanostructure comprised of a magnetostrictive core of cobalt ferrite ($Co_2Fe_2O_4$ *i.e.*, CFO) and ferroelectric shell of barium titanate ($BaTiO_3$ *i.e.*, BTO).[5-7] The MENP acts as a multifunctional material on applying alternating current (AC) magnetic field as a result of the presence of the magnetic core and piezoelectric shell.[3, 5, 8] Upon inducing the AC B-field, the MENP core went through the strain deformation which was further absorbed by the shell to produce a magneto-elastic wave.[5] The surface potential of MENPs is also altered to cause a change in polarization. As a result of the controlled magneto-electric nature, in addition to biological applications, the MENP is also an ideal candidate for several other applications. Some of these include magnetic-field sensors, miniature antennas, high-density data storage, spintronics, energy harvesters, and micro-electromechanical systems where a magneto-electro-elastic coupling is an essential requirement.[9-13]

We have explored MENP as a potential bio-compatible drug nanocarrier to deliver a targeted therapeutic agent across the blood-brain barrier.[6, 14] On-demand release of bio-actives (anti-HIV drug, siRNA, and edited gene Cas9/gRNA) from MENPs based nanomedicine on applying AC B-field stimulation have also been recently demonstrated.[15-17] The finding of our research suggests that the MENP based nanomedicine exhibited an enhanced therapeutic effect. The mechanism behind the rapid cell-uptake and on-demand drug release is likely related to the rotation motion, the

magneto-elastic wave, and the generation of localized tunable/reversible surface charge change of MENPs under AC B-field stimulation.

While theoretically formulated, an experimental demonstration of the mechanism, along with quantification of this scientific reasoning, has not been accomplished yet.

Ultrasensitive detection of surface properties is essential in the fields of surface science,[18] colloid science,[19-22] mineralogy,[23-25], and understanding of chemical/biological processes at the nanoparticle(NP)-biological system interfaces. [18, 19, 26-33] Methodologies such as zeta potential and potentiometric titration are in practice to estimate the average surface charge density change of a nano-system suspended in solution.[34-36] Recently, single-entity electrochemistry techniques[37-40] are emerging as potential solutions that can effectively probe the physicochemical properties, including surface charge, of the single entities in the electrolyte. These single-entity approaches can also provide more fundamental and technological information than conventional ensemble methodologies.[38, 39]

Here, we are demonstrating the detection of surface charge enhancement of individual MENPs under AC B-field through collision events of MENPs at the carbon nanoelectrode (CNE) of a nanopore-nanoelectrode nanopipette.[41, 42] The collision events of individual NPs at the CNE are detected by an open-circuit potential (OCP) detection method, which has been validated using gold NPs and polystyrene NPs.[42] The AC B-field stimulation is generated by electromagnetic coils. The majority of the measurements were made at 60 Oe. The previous studies confirm the stimulation at this magnitude is optimized and safe, which causes effective cell-uptake *via* nano-electroporation[6] and release of therapeutic

agents (SiRNA and Cas9/gRNA) from the surface of MENPs-based nano-formulation.[15, 16] Noticeable differences in the induced potential signal changes during MENP-CNE collision events were observed only in the case of AC B-field stimulation as a result of localized surface potential increment on the surface of MENP. In contrast, the surface potential enhancement was not observed in the absence of AC B-field stimulation or when magnetic nanoparticles (MNP) were used.

5.2 Experimental Methods

The experimental methods used to accomplish this project are described in Chapter 2. Section 2.1 and its subsections provide an overview of multi-functional nanopipette fabrication and its electrical/optical characterization. Section 2.3 and its subsections describe the electrical and electrochemical measurements, dark field microscopy, theoretical estimation of net forces acting on the nanoparticles, theoretical estimation of potential change on a MENP surface, diffusion-limited events rates from Stokes-Einstein relationship, salinization, AC-B field stimulation, and data analysis method. The reagents and solutions used in the project are described in the subsection below.

5.2.1 Materials and Reagents.

ACS grade chemicals (e.g., Phosphate Buffer Saline (PBS) for pH 7.3-7.5) were purchased from Fisher Scientific and used without any further purification. The MENPs utilized in this research were synthesized and characterized using our established and published protocol.[6] Iron oxide nanoparticles (~50-100 nm) as magnetic nanoparticles (MNPs) were purchased from Sigma Aldrich. Gold nanoparticles (GNP) of 40 nm were purchased from BBI Solutions Inc. The 3-cyanopropyldimethlychlorosilane for nanopipette surface

modification was obtained from Fisher Scientific. Redox molecule Hexaaammineruthenium (III) chloride [Ru $(NH3)_6Cl_3$] (98 % pure) was purchased from Sigma-Aldrich. All solutions were prepared using DI water (~18 MΩ) (Ultra Purelab System, ELGA/Siemens).

5.3: Results and Discussions

5.3.1: The MENP and the Setup to Detect Single-MENP by a Nanopore-CNE Nanopipette.

The transmission electron microscope (TEM) image of MENP is shown in Figure 5.1a. The MENP has irregular spherical-like morphology with an average size of 25 ± 5 nm. The XRD analysis of the MENP further confirms that MENPs are crystalline and composed of CFO and BTO.[6, 14] For each MENP, the magnetostrictive CFO core is surrounded by a piezoelectric BTO shell. The mean zeta potential of MENPs was estimated to be -23.5 ± 5.8 mV using dynamic light scattering (DLS) based zeta potential measurements in 10 mM PBS (pH 7.1) solution. It has been reported that the zeta potential of MENP becomes more negative after applying a DC B-field.[5, 14] When the magnitude of the B-field increases to 100 Oe, up to 30% increase in the zeta potential was observed. For comparison, the larger (~50-100 nm size) MNP has a smaller mean zeta potential of about -15.4 ± 4.6 mV.

Figure 5.1b illustrates the mechanism of the detected surface charge increase of the MENP stimulated by an AC B-field. Under an AC B-field, a directional strain (ε) is produced in the magnetostrictive CFO core and transferred to the BTO shell as the mechanical stress. The mechanical stress leads to the charge redistribution on the piezoelectric BTO shell and the generation of additional net charges.

The general relationship between the applied strain (ε) and the generated electric potential (V) of piezoelectric material (e.g., BTO) is given as

$$\varepsilon = d \times \frac{V}{l} \tag{5.1}$$

where d is the magnetoelectric coefficient and l is the thickness of the material. Assuming the CFO (core) and BTO (shell) has no gap at the interface and the strain generated along the same direction of the applied B field (60 Oe), the induced electric potential on the BTO shell of ~6 nm thickness is estimated to be ~ -1.30 mV (See Chapter 2 section 2.3.5). Here, we are interested in detecting the surface charge increase of the individual MENPs under an AC B-field.

The schematic of the experimental setup is illustrated in Figure 5.1c. The nanopore-CNE nanopipette utilized during this research has a long-taper geometry with pore diameter ranging from 50 to 90 nm. The average effective surface area of CNE is estimated to be 0.21 μm^2. All the experiments were conducted using eight well-characterized nanopipettes (P1-P8, See Chapter 2 section 2.3.1). A constant bias V_{pore} is applied through the nanopore barrel. Before adding MENPs in the bath solution, both the current-time (*i*-t) and potential-time (*V*-*t*) traces acquired respectively through the nanopore and CNE were stable and featureless. After adding MENPs, small *i* and *V* changes appeared in the time traces. These transient changes are as a result of the interactions between NPs and the nanopipette apex and most are at a single-NP level.[41] As illustrated in Figure 5.1d, two types of NP-nanopipette interaction events may be observed: (i) translocation through the nanopore and (ii) collision near the CNE surface.

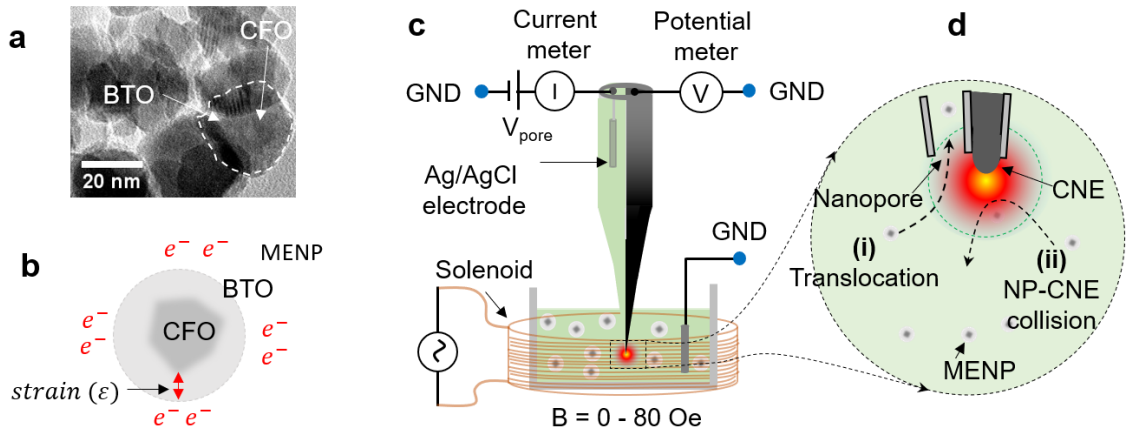

Figure 5. 1: (a) The TEM image of the MENP showing (CFO) core and (BTO) shell (dotted region). (b) Schematic illustration of the CFO-BTO MENPs' strain mediated localized surface charge enhancement in the presence of AC B-field. Strain (ε) denotes the directional strain generated at the CFO core. The redistribution of charge is indicated by the electrons. (c) The experimental setup for the detection of the surface potential of single NP by using the CNE nanopore nanopipette. V_{pore} is the applied bias. Potential (V) is measured by using a high impedance differential amplifier. The gradient red-colored region around the nanopipette apex represents the potential sensing zone of the nanoelectrode. MENPs are suspended in the bath solution. The yellow coil around the vial is a solenoid to apply AC B-field. (d) Zoomed-in of the nanopipette apex in (a) (not to scale). The curved dashed arrows represent the nanopore translocation and MENP-CNE collision events under AC B-field stimulation.

5.3.2: The Detection of AC B-Field Induced Surface Potential Change by MENP-CNE Collision Events.

To understand the detected signals, let us first discuss the motion of the NPs in solution under various forces. In our experiment, the NP may experience 3 types of forces. First, the electric forces. The electric forces include the driving force by the applied positive nanopore bias and the repulsive electrostatic force by the negative surface charges of both glass and NPs. The estimated force induced by V_{pore} of +0.4 V is ~ 100 pN (See Chapter 2 section 2.3.4). Second, the Stokes drag force which results from the solution's viscosity and is of the order of 0.001 pN (See Chapter 2 section 2.3.4). Third, the magnetic force as a result of the external B-field. Since the magnetic field is uniform at the center of the solenoid, magnetic NP does not experience magnetic force but only magnetic torque.

Therefore, the B-field only induces the rotational motion but not the translational motion of the magnetic NPs. The estimated magnitudes of angular velocity and the corresponding tangential linear velocity of MENP at 60 Oe AC B-field are 1032 rad/s and 6.5 μm/s respectively (See Chapter 2 section 2.3.4). For comparison, the corresponding values for MNP are 433 rad/s and 25.5 μm/s.

We imaged the movement of individual MENPs in solution by DFM under the same experimental conditions. No visible differences can be noticed from the MENPs' motion with and without the AC B-field (See the attached DFM video S1a). The MENPs maintained their random motions and did not oscillate with the applied AC frequency (various frequencies have been tested), confirming that no magnetic force is applied on the MENPs. It is also the same for MNPs (See the attached DFM video S1b).

The simultaneous measurements of current and potential *via* the nanopore and CNE can help to separate types (i) and (ii) events. A typical NP-CNE collision event induces obvious changes of V of the CNE but a negligible change of *i* of the nanopore. However, the NP translocation events through the nanopore produce obvious and correlated *i* and *V* changes. From the observed current and potential changes, translocation events of MENPs through the nanopore only happen occasionally both with and without the B-field (See Figure 5.2). The low translocation event rate is attributed to the high entrance barrier of nanopore for MENPs. The entrance barrier arises from the surface charge of the quartz surface and the entropy penalty. In contrast, we detected a large number of collision events from the CNE. It should be noted that the NPs do not need to physically touch the CNE surface to be detected in the NP-CNE collision events. Most events are actually detected when the NP

double layer and the CNE sensing zone overlap. This is reflected from the facts (See below) that most of the detected surface potentials are much smaller than the zeta potential of NP. With a larger detection distance range, more collision events are observed. Below we will focus on the type (ii) NP-CNE collision events.

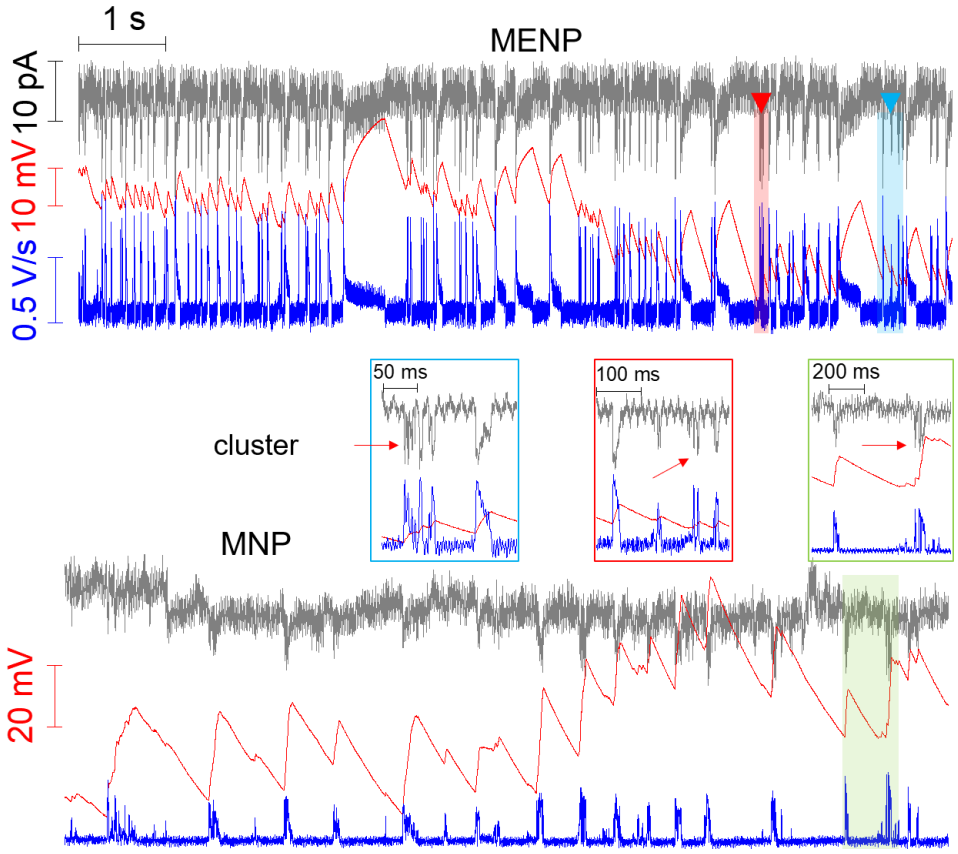

Figure 5. 2: Typical time traces of current (gray), potential (red), and potential first derivative (blue) for the MENP (top panel) and MNP (bottom panel) nanopore translocation events at 60 Oe (V_{pore} = 400 mV) AC B-field. Nanopipettes P5 and P6 have been used to obtain the MENP and MNP translocation data, respectively. Occasionally, clustered events (highlighted in the zoomed-in windows) were observed in both MENP and MNP experiments. The red arrows denote the clustered translocation events. The dV/dt curves were smoothed by the moving average method using a 2 ms time window.

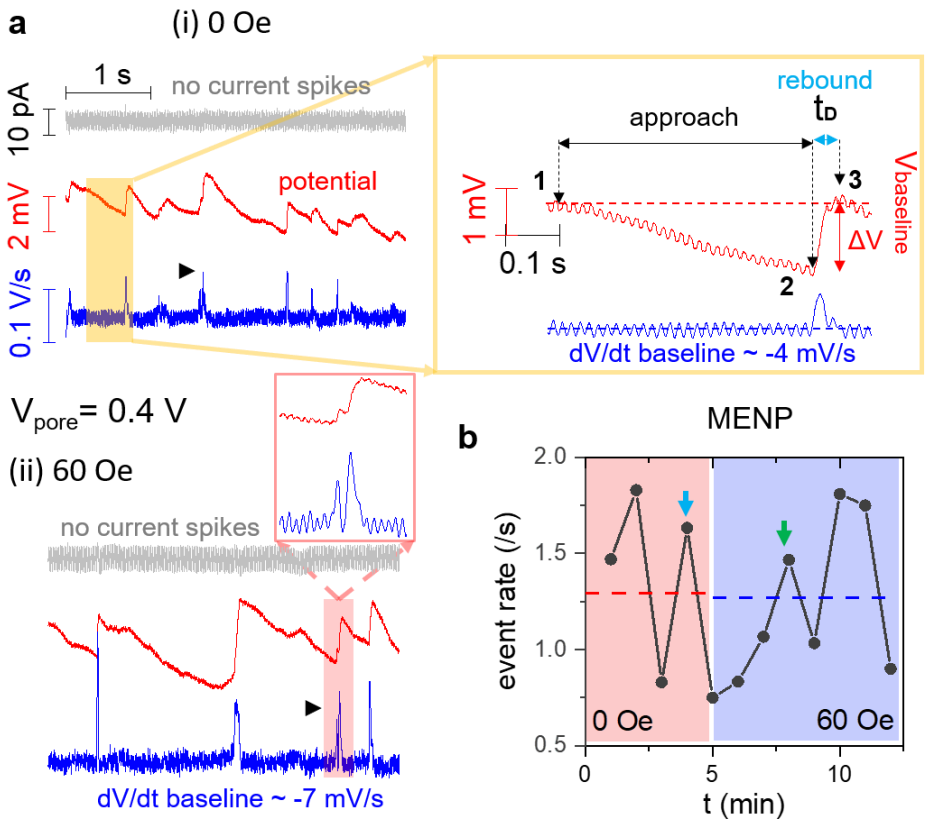

Figure 5. 3: (a) Typical time traces of current (gray), potential (red) and the first derivative of potential (blue) at V_{pore} = 0.4 V (i) without and (ii) with an AC B-field. The zoom-in of a potential dip illustrating the collision event in 2 steps, approach (1-2) and rebound (2-3). ΔV denotes the amplitude of the potential dip. The t_D is the time duration of the rebounding. The black arrows and zoom-in of a potential dip in (ii) denote a collision event as a result of two clustered MENPs. (b) The MENP collision event rate as a function of time without (light red region) and with (light blue region) a 60 Oe AC B-field stimulation. Each point is averaged over 1-minute data. The blue and green arrows denote the time at which time traces (i) and (ii) are recorded, respectively.

Figure 5.3a (i) shows a typical *V-t* trace (red color) with continuous potential changes when no AC B-field is applied. More data is shown in Figure S3a. This data was collected by nanopipette P1 at V_{pore} = 400 mV. There are no corresponding current changes in the current trace (gray color). Therefore, these potential changes are induced by MENP-CNE collision events. The shape of the potential dips suggests most of them are single-NP events. The small clustered NPs often generate a staircase increase in the rebounding section of the potential dip and multiple peaks in the dV/dt trace. Two such events are

indicated by the black arrows in Figure 5.3a (i) and (ii) traces, with more examples showing in Figure S3b. The right side of Figure 5.3a (i) shows the zoom-in of a potential dip from a single-NP event. The general feature of which reveals the approach (points 1 to 2) and rebounding (points 2 to 3) motions during a MENP-CNE collision event. From the dV/dt magnitude (the blue color trace), the speed of approach is significantly smaller than the speed of rebounding. When an AC B-field is applied (See Figure 5.3a (iii)), the magnitude ΔV of a large fraction of potential dips increases obviously. Correspondingly, both the approaching and rebounding dV/dt magnitudes of these potential dips are increased obviously. We believe the observed increases are as a result of the increased surface charge of MENPs under an AC B-field stimulation.[3, 5, 8]

To confirm, we performed control experiments using MNP at the same experimental conditions. As shown in Figure 5.5b inset, the observed potential dips induced by the single MNP-CNE collision events show similar shape at V_{pore}= 0.4 V with zero or 60 Oe AC B-field. No obvious difference is noticed in the ΔV and dV/dt magnitudes of the potential dips when the B-field is changed from zero to 60 Oe. The insensitivity to the AC B-field stimulation is expected because the MNPs lack the magneto-electric property.

Figure 5.3b shows the event rate of potential dips as a function of time for MENPs with zero and 60 Oe AC B-field. At both B-fields, the event rate varies between ~0.5 and ~2 events/s with an average value of ~1.2 events/s over 5 mins. The fluctuations of the event rate reveal the dynamic changes of MENP local concentration near the CNE, which are induced by the dynamic accumulations and dispersion of NPs near the apex. In the control

experiments with MNPs, the event rate as a function of time without/with an AC B-field are presented in Figure 5.4. The average event rate is ~0.24 events/s.

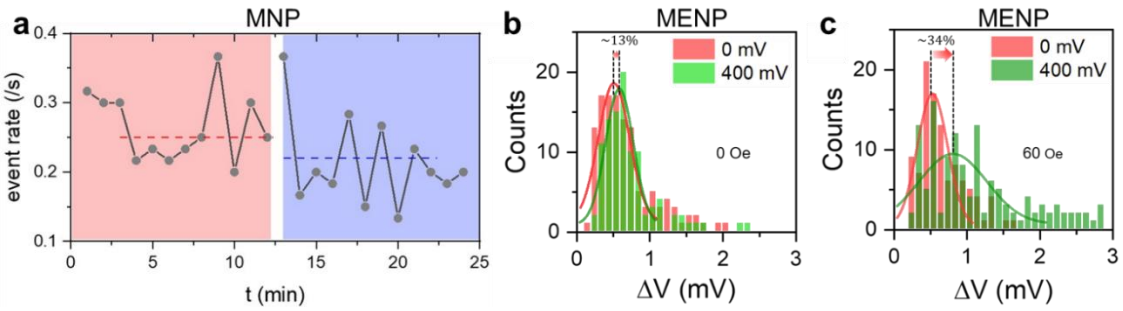

Figure 5. 4: (a) The event rate of MNP-CNE collision event without (light red region) and with a 60 Oe (light blue region) AC B-field as a function of time. The average event rates over 10 minutes at 0 and 60 Oe AC B-field are 0.25 and 0.22 events/s, respectively. The nanopipette P2 was used to acquire the data at 400 mV nanopore bias. The concentration of MNP in 10 mM PBS was 1 nM. Effect of the nanopore bias (V_{pore}) on the potential dip amplitude ΔV during the MENP-CNE collision without (b) and with (c) the presence of a 60 Oe AC B-field using the nanopipette P8. The radius of the nanoelectrode of a nanopipette P8 is 89±24 nm. The most probable values of ΔV for MENP-CNE collision events at 0 mV and 400 mV nanopore biases are 0.51 ± 0.21 mV and 0.59 ± 0.19 mV respectively. The most probable values of ΔV for MNP-CNE collision events at 0 mV and 400 mV nanopore biases are 0.54 ± 0.21 mV and 0.82 ± 0.47 mV respectively. The solid lines in the histograms are the Gaussian fits.

From the Stokes-Einstein relationship using bulk concentration, we estimate the diffusion-limited event rates are 8.45 events/s and 1.26 events/s for MENP and MNP, respectively (See Chapter 2 section 2.3.6). The smaller theoretical event rate of MNP is as a result of its larger size. For MENP, the theoretical value is about 18 times higher than the experimental value (0.46 /s) at zero V_{pore}. Similarly, for MNP, the theoretical value is ~ 6 times higher than the experimental value (0.21 /s) at zero V_{pore}. One possible reason for the lower experimental value is attributed to the smaller actual bulk concentration of NP considering the loss of NPs as a result of surface adsorption and aggregation. Between MENP and MNP, the MENPs are less stable at the zero B-field. However, the stimulation

of AC B-field can effectively improve the stability of the MENPs, which is attributed to their increased surface charge and the rotation motion. Another possible reason for the lower event rate in experiments is attributed to the electrostatic repulsion between negatively charged NPs and the nanopipette apex, which prevents some NPs from moving closer to the CNE. We noticed that the event rate is typically higher at 0.4 V than at 0 V. The applied positive V_{pore} helps to compete with the repulsive force, thus boosting the event rate. For MENP, the V_{pore}-dependent event rate increase is more obvious under a stronger B-field (see Figure 5.4b, c). Therefore, the B-field induced surface change enhancement amplifies the V_{pore} effect.

Statistical analysis results of the potential dips without/with AC B-field for MENP are presented in Figure 5.5a. Only potential dips that are clearly separated and less affected by the adjoining MENPs were analyzed. The ΔV *vs.* t_D scatter plots and the corresponding ΔV histograms of the MENP potential dips at zero and 60 Oe AC B-field are shown in Figure 5.5a. In the scatter plots, the distribution of data with 60 Oe AC B-field (blue color) is much broader with more points showing bigger ΔV and t_D. At zero B-field, the red color ΔV histogram shows one peak with the mean ΔV ~0.77 ± 0.37 mV. At 60 Oe B-field, a shoulder peak appears near the main peak in the blue color ΔV histogram. The width of the shoulder peak is broader and with contributions from about 45% of the total events. The main peak of the blue color histogram is very close to the peak of the red color histogram. However, the two-peak Gaussian fit to the histogram gives a mean ΔV ~1.95 ± 0.79 mV for the shoulder peak. It is an increase of ~2.5 times in magnitude from -0.77 mV to -1.95 mV. The broad distribution likely reflects the heterogeneous response of the MENPs to the stimulation of the AC B-field.[5] A previous study showed that the surface charge

enhancement is proportional to the strain deformation of the BTO shell.[5] The structural heterogeneity between MENPs, such as size, shape and surface curvature variations, may produce different surface charge increase on the MENPs-shell surface.

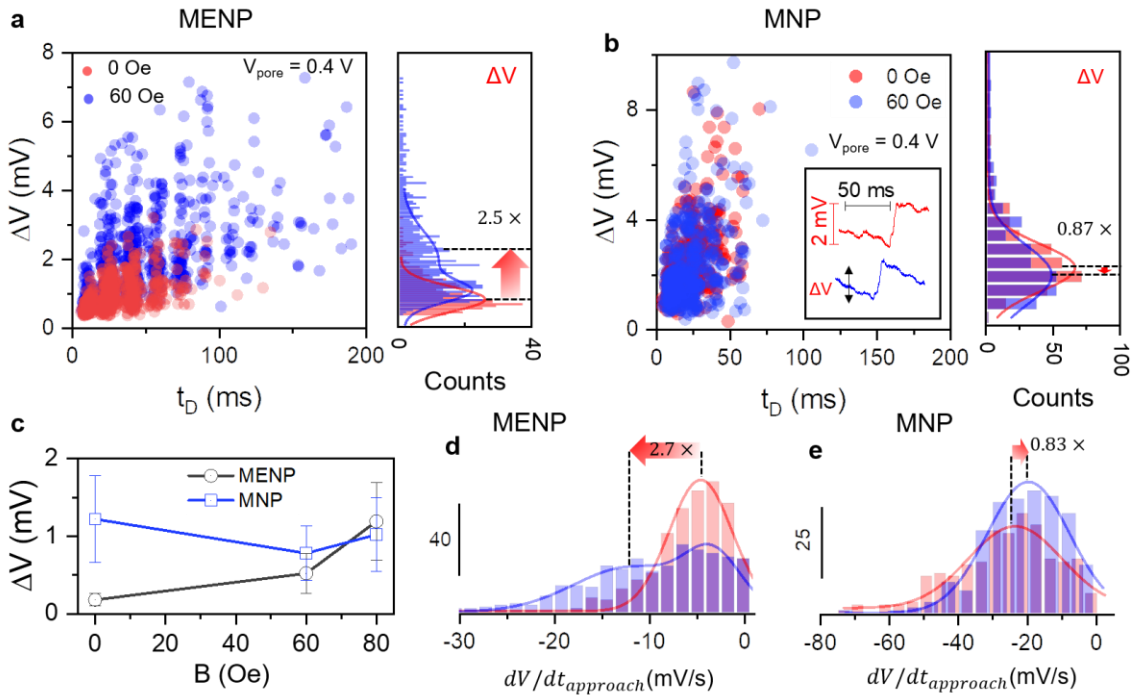

Figure 5. 5: The statistics of collision events of MENP and MNP detected by the nanopipette at V_{pore} =0.4 V. (a) The scatter plot of ΔV- t_d for the MENP-CNE collision events without (blue, N = 427) and with (red, N = 628) the AC B-field using nanopipette P1. The histograms at the right side show potential dip amplitude (ΔV). (b) The scatter plot of ΔV- t_d for the MNP-CNE collision events without (N = 316) and with (N = 302) the AC B-field using a nanopipette P2. The histograms at the right show potential dip amplitude (ΔV). The inset denotes the typical nanoimpact events without (i) and with (ii) an AC B-field. (c) ΔV *vs.* AC B-field intensity plot for the MENP and MNP using nanopipettes P3 and P4 respectively. The y-error bars are the standard deviation from the mean value. The distributions of $dV/dt_{approach}$ of the MENP-CNE (d) and MNP-CNE (e) collision events at zero (red color) and 60 Oe (blue color) AC B-field. Solid lines in the histograms are Gaussian fits.

For comparison, the statistical analysis results of the potential dips of control experiment MNPs are shown in Figure 5.5b. The distributions of data points in the ΔV *vs.* t_D scatter plots are similar at both zero and 60 Oe AC B-field. Both ΔV histograms only show one

peak, which can be fitted by the one peak Gaussian function. The mean ΔV values are 2.07 ± 0.86 mV at zero Oe and 1.80 ± 1.08 mV at 60 Oe, respectively. The ΔV of MNPs with 60 Oe AC B-field is slightly smaller than with zero AC B-field. This is contrary to the results of MENPs in Figure 5.5a.

Previous DLS measurements have shown that with the increase of the applied DC B-field strength, the zeta potential of the MENPs increases.[14] We further checked the ΔV change at 80 Oe B-field. The plot in Figure 5.5c shows the ΔV of MENP increases with the increase of the AC B-field amplitude. The mean ΔV values of the shoulder peak at 60 and 80 Oe are used in the plot. The overall trend of the charge enhancement is similar to the previous report. In contrast, the ΔV of MNPs does not show the increasing trend with the increase of the AC B-field (blue color) (See Figure 5.6).

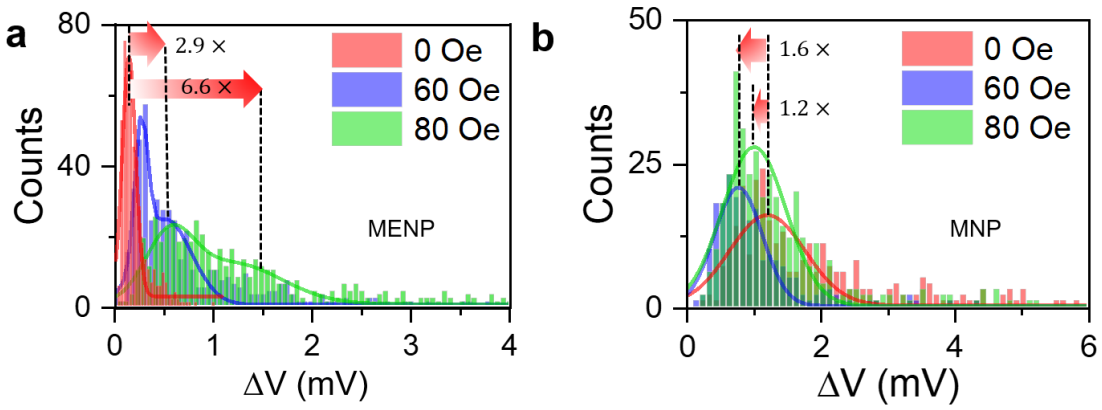

Figure 5. 6: The changes of ΔV as a function of the AC B-field magnitude. (a) The histograms of ΔV of the potential dip of the MENP-CNE collision events at 0, 60, and 80 Oe. The most probable values are 0.18 ± 0.07, 0.52 ± 0.26 and 1.19 ± 0.50 mV, respectively. (b) The histograms of the ΔV of the potential dip of MNP-CNE collision events at 0, 60, and 80 Oe. The most probable values are 1.22 ± 0.56, 0.78 ± 0.35 and 1.02 ± 0.47 mV, respectively. The solid lines in the histograms are the Gaussian fits.

The MENP results in Figure 5.5 are acquired at V_{pore}= 0.4V. At zero V_{pore} bias, the ΔV of the potential dip is smaller. When the V_{pore} is increased from zero to 400 mV, the ΔV

increases by 13% at zero Oe but by 34% at 60 Oe B-field (See Figures 5.4b, c). The V_{pore} induced ΔV increase is bigger with the AC B-field, which also originated from the B-field induced surface charge enhancement of MENPs. The same V_{pore} can produce a bigger electric force on the approaching MENP with the increased surface charge, leading to a smaller MENP-CNE distance during the collision and thus an increased ΔV in the potential dip.

We further compared the mean approach slope ($dV/dt_{approach}$) of potential dips for MENPs at 0.4 V with and without a 60 Oe B field. The distribution of $dV/dt_{approach}$ is shown in Figure 5.5d. The mean $dV/dt_{approach}$ at zero and 60 Oe AC B-field are ~-4.3 ± 3.2 mV/s and ~-11.7± 6.1 mV/s, respectively. The dV/dt value is ~2.7 times larger when the AC B-field is increased from zero to 60 Oe. The increase of $dV/dt_{approach}$ suggests the increase of the approaching speed of the MENP, which is induced by the increased electric force on the MENP with the B-field. In contrast, in the MNP control experiment, the $dV/dt_{approach}$ value is slightly reduced by ~13% with the 60 Oe AC B-field (Figure 5.5e). MNPs slow down slightly as they approach the CNE in presence of the AC B-field. This observation is consistent with the slightly reduced ΔV for the MNP in the presence of AC B-field. The small change may be attributed to the rotation motion of the MNP in a B-field.

Between MENPs and MNPs, the mean ΔV and $dV/dt_{approach}$ are both bigger for MNPs under the same 60 Oe B-field and 0.4 V V_{pore} bias. Because the motion of NP is mainly driven by the electric forces instead of diffusion, the differences can be attributed to the bigger size of MNP, which induced a bigger floating potential change at the CNE when both the NP-CNE distance and CNE size are the same. In addition, the smaller electrostatic

repulsion experienced by the MNP (smaller zeta potential) also helps the MNP be closer to the CNE with a bigger approaching speed.

5.3.3: The Changes of Potential Dips of MENP-CNE Collision Events by Chemically Modified Nanopipette.

The high negative surface charge of the nanopipette apex slowed down the approaching motion of MENP and prevented it from getting closer to the CNE surface. To suppress the surface charge effect, we also chemically modified the quartz surface with a neutral molecule (See Chapter 2 section 2.3.7). Indeed, the average event rate increased by 32% after the chemical modification in both the cases (Figure 5.7a) using the nanopipette with very similar characteristics as before. Figure 5.7b shows the statistical analysis of the potential dips at V_{pore} = 0.4 V and with zero or 60 Oe AC B-field. More data can be found in Figure S7. Before applying the AC B-field, the potential distribution is a single peak with the mean value ΔV of ~3.35 ± 2.30 mV. With the 60 Oe AC B-field, the ΔV distribution is much broader and bimodal, with two average ΔV values at ~3.10 ± 1.10 mV and ~12.90 ± 3.65 mV. The value of the first ΔV is close to the one measured without AC B-field. After surface modification, the overall increase in the detected MENPs surface potential in the absence of an AC B-field is expected as the electrostatic repulsion is weaker between the MENPs and the nanopipette apex. Stimulated by 60 Oe AC B-field, the ΔV is increased by ~3.8 times.

We further analyzed the approach slope of the potential dip to derive the approaching speed of the MENP towards the CNE (Figure 5.7c). The average value of the slope is –7.2 ± 5.1 mV/s without the AC B-field stimulation. With the AC B-field, we detected two values – 6.1 ± 4.2 mV/s and –84.6 ± 11.2 mV/s. The first one is also attributed to the MENPs without

surface charge increase. The latter one is about 11.8 times higher than the measured value without the presence of AC B-field. Therefore, compared with the data of non-modified nanopipette, the data using modified nanopipette reveal the same trend of change triggered by the applied AC B-field. However, the increase of both ΔV and dV/dt of the potential dip signals is more obvious and bigger. The difference is attributed to the smaller electrostatic repulsion by the nanopipette surface charge. Therefore, the NPs can be closer to the CNE. These bigger changes better illustrate the surface charge/potential increase of MENP under the stimulation of AC B-field.

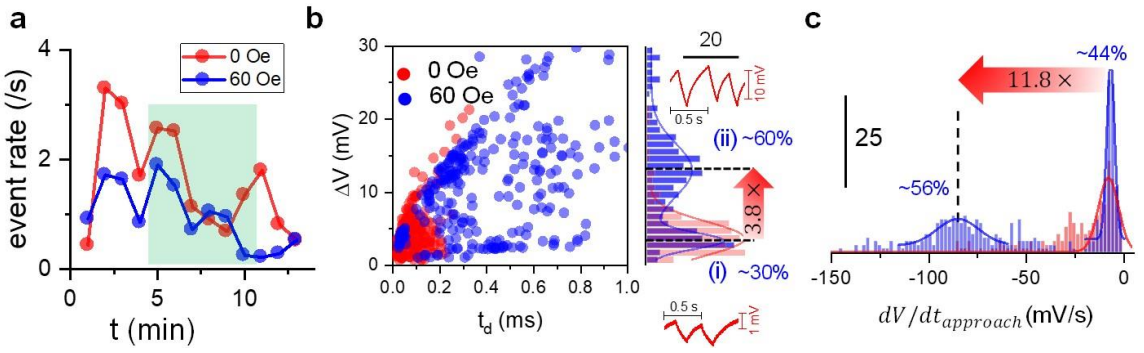

Figure 5. 7: The statistics of MENP-CNE collision events from the surface-modified nanopipette P7 without (red) and with (blue) AC B-field stimulation. (a) MENP-CNE collision events rate as a function of time. The events in the shaded regions are used for analysis. (b) Scatter plot of ΔV vs. t_d for the MENP-CNE collision events. The histograms on the right side show the potential amplitude distributions. The potential time trace in the inset of histogram presents the type (i) and type (ii) events that appeared in the ΔV histogram distribution. (c) The potential slope analysis of the MENP-CNE collision events without/with AC B-field. Solid lines in the histograms are Gaussian fits.

5.4: Conclusion

The AC B-field stimulated surface charge enhancement of MENPs was carefully examined at the single-NP level in this research by probing the OCP change of a floating nanoelectrode during the 'nanoimpact' events by individual MENPs. By analyzing the motion pattern of individual NPs during the collision events before and after the application

of an AC B-field, we can confirm the surface charge/potential enhancement of MENPs stimulated by the AC B-field. This study also suggests that in applying AC B-field stimulation, the surface potential increase in nanoparticle surface potential change is as a result of the presence of the piezoelectric shell of MENP. The proposed scientific reasoning was validated using a positive control of MNP wherein piezoelectric shell is absent. We also noticed the obvious heterogeneity in the response to the B-field stimulation, which may provide a convenient way to evaluate the uniformity of the synthesized MENP, the effects of MENP size, and surface curvature to the AC B-field stimulation or the aging of MENP with time.

The results of 'nanoimpact' based single-MENP analysis method have confirmed the effective remote tuning of the surface potential of MENP by the applied AC B-field. In the next step, we will use the same method to probe the magneto-elastic wave produced by the MENPs upon the stimulation of the AC B-field. The MENPs with tunable magneto-elasto-electric properties should have immediate biomedical applications. MENPs-supported therapies have the potential to be the most efficient nanoparticle-based therapies where targeted drug delivery, image-guided therapy, on-demand controlled release, and stimuli responsiveness-based treatments are the key requirements.[17, 43, 44] Such therapies can be the possible new treatment for central nervous system (CNS) diseases, cancer, brain stimulation, etc.., even in a personalized manner.

We also demonstrated the capability of the potentiometric single-entity 'nanoimpact' technique. Most of the current 'nanoimpact' methods relied on the electrochemical current signal. If the NP is not redox-active, additional redox mediators are needed in the solution.

The colliding NP also needs to be in the tunneling distance with the ultrasmall electrode surface to be detected. In contrast, no electron transfer process is needed for the OCP based measurement. The NP can be detected in a much larger distance. The single-NP OCP signal is also easy to be measured by the amplifier in the low gain and high bandwidth settings, allowing for higher sensitivity and faster detection. Therefore, the potentiometric single-entity 'nanoimpact' technique is suitable to detect non-electroactive biomolecules, such as nucleic acids and proteins, without adding redox mediators in the solution.

5.5: References

1. Pandey, P., et al., *Single-entity approach to investigate surface charge enhancement in magnetoelectric nanoparticles induced by AC magnetic field stimulation.* ACS Sensors, 2020.

2. Karimi, M., et al., *Smart micro/nanoparticles in stimulus-responsive drug/gene delivery systems.* Chemical Society Reviews, 2016. **45**(5): p. 1457-1501.

3. Hu, J.-M. and C.-B. Eom, *Magnetic-field control of ionic bonds on ferroelectric surfaces.* Applied Physics Letters, 2019. **114**(9): p. 091601.

4. Stimphil, E., et al., *Physics considerations in targeted anticancer drug delivery by magnetoelectric nanoparticles.* Applied Physics Reviews, 2017. **4**(2): p. 021101.

5. Betal, S., et al., *Magneto-elasto-electroporation (MEEP): In-vitro visualization and numerical characteristics.* Scientific Reports, 2016. **6**: p. 32019.

6. Kaushik, A., et al., *Investigation of ac-magnetic field stimulated nanoelectroporation of magneto-electric nano-drug-carrier inside CNS cells.* Scientific Reports, 2017. **7**: p. 45663.

7. Betal, S., et al., *BaTiO3 Coated CoFe2O4–Core-Shell Magnetoelectric Nanoparticles (CSMEN) Characterization.* Integrated Ferroelectrics, 2015. **166**(1): p. 225-231.

8. Sablik, M.J., et al., *Relationship between magnetostriction and the magnetostrictive coupling coefficient for magnetostrictive generation of elastic waves.* AIP Conference Proceedings, 2002. **615**(1): p. 1613-1620.

9. Ma, J., et al., *Recent Progress in Multiferroic Magnetoelectric Composites: from Bulk to Thin Films.* Advanced Materials, 2011. **23**(9): p. 1062-1087.

10. Wang, Y., et al., *Multiferroic magnetoelectric composite nanostructures.* Npg Asia Materials, 2010. **2**: p. 61.

11. Tang, X. and L. Kou, *Two-Dimensional Ferroics and Multiferroics: Platforms for New Physics and Applications.* The Journal of Physical Chemistry Letters, 2019. **10**(21): p. 6634-6649.

12. Domann, J., et al., *Strain-mediated magnetoelectric storage, transmission, and processing: Putting the squeeze on data.* MRS Bulletin, 2018. **43**(11): p. 848-853.

13. Palneedi, H., et al., *Status and Perspectives of Multiferroic Magnetoelectric Composite Materials and Applications.* Actuators, 2016. **5**(1).

14. Rodzinski, A., et al., *Targeted and controlled anticancer drug delivery and release with magnetoelectric nanoparticles.* Scientific Reports, 2016. **6**: p. 20867.

15. Kaushik, A., et al., *Magnetically guided non-invasive CRISPR-Cas9/gRNA delivery across blood-brain barrier to eradicate latent HIV-1 infection.* Scientific Reports, 2019. **9**(1): p. 3928.

16. Rodriguez, M., et al., *Electro-Magnetic Nano-Particle Bound Beclin1 siRNA Crosses the Blood–Brain Barrier to Attenuate the Inflammatory Effects of HIV-1 Infection in Vitro.* Journal of Neuroimmune Pharmacology, 2017. **12**(1): p. 120-132.

17. Nair, M., et al., *Externally controlled on-demand release of anti-HIV drug using magneto-electric nanoparticles as carriers.* Nature Communications, 2013. **4**(1): p. 1707.

18. Cuesta, A., *Measurement of the Surface Charge Density of Co-Saturated Pt (111) Electrodes as a Function of Potential: The Potential of Zero Charge of Pt (111).* Surf. Sci., 2004. **572**: p. 11.

19. Hirsch, V., et al., *Surface Charge of Polymer Coated Spions Influences the Serum Protein Adsorption, Colloidal Stability and Subsequent Cell Interaction.* Nanoscale, 2013. **5**: p. 3723.

20. Tufenkji, N. and M. Elimelech, *Breakdown of Colloid Filtration Theory: Role of the Secondary Energy Minimum and Surface Charge Heterogeneities.* Langmuir, 2005. **21**: p. 841.

21. Ohshima, H., T.W. Healy, and L.R. White, *Accurate Analytic Expressions for the Surface Charge Density/Surface Potential Relationship and Double-Layer*

Potential Distribution for a Spherical Colloidal Particle. J. Colloid Interface Sci., 1982. **90**: p. 17.

22. Chan, D.Y., R.M. Pashley, and L.R. White, *A Simple Algorithm for the Calculation of the Electrostatic Repulsion between Identical Charged Surfaces in Electrolyte.* J. Colloid Interface Sci., 1980. **77**: p. 283.

23. Lin, N.H., et al., *Crystallization of calcium sulfate on polymeric surfaces.* J Colloid Interface Sci, 2011. **356**(2): p. 790-7.

24. Bodhak, S., S. Bose, and A. Bandyopadhyay, *Role of Surface Charge and Wettability on Early Stage Mineralization and Bone Cell–Materials Interactions of Polarized Hydroxyapatite.* Acta Biomater., 2009. **5**: p. 2178.

25. Sahın, Ö. and A. Nusret Bulutcu, *Effect of Surface Charge Distribution on the Crystal Growth of Sodium Perborate Tetrahydrate.* J. Cryst. Growth, 2002. **241**: p. 471.

26. Manzini, M.C., et al., *Peptide:Lipid Ratio and Membrane Surface Charge Determine the Mechanism of Action of the Antimicrobial Peptide Bp100. Conformational and Functional Studies.* Biochim. Biophys. Acta, Biomembr., 2014. **1838**: p. 1985.

27. Bakhti, M., et al., *Loss of Electrostatic Cell-Surface Repulsion Mediates Myelin Membrane Adhesion and Compaction in the Central Nervous System.* Proc. Natl. Acad. Sci. U. S. A., 2013. **110**: p. 3143.

28. Xiao, K., et al., *The Effect of Surface Charge on in Vivo Biodistribution of Peg-Oligocholic Acid Based Micellar Nanoparticles.* Biomaterials, 2011. **32**: p. 3435.

29. Dobrovolskaia, M.A., et al., *Nanoparticle Size and Surface Charge Determine Effects of Pamam Dendrimers on Human Platelets in Vitro.* Mol. Pharmaceutics, 2011. **9**: p. 382.

30. Chen, L., et al., *The Role of Surface Charge on the Uptake and Biocompatibility of Hydroxyapatite Nanoparticles with Osteoblast Cells.* Nanotechnology, 2011. **22**: p. 105708.

31. Asati, A., et al., *Surface-Charge-Dependent Cell Localization and Cytotoxicity of Cerium Oxide Nanoparticles.* ACS Nano, 2010. **4**: p. 5321.

32. Ghosh, P.S., et al., *Efficient Gene Delivery Vectors by Tuning the Surface Charge Density of Amino Acid-Functionalized Gold Nanoparticles.* ACS Nano, 2008. **2**: p. 2213.

33. Chung, T.H., et al., *The Effect of Surface Charge on the Uptake and Biological Function of Mesoporous Silica Nanoparticles in 3t3-L1 Cells and Human Mesenchymal Stem Cells.* Biomaterials, 2007. **28**: p. 2959.

34. Szekeres, M. and E. Tombácz, *Surface Charge Characterization of Metal Oxides by Potentiometric Acid–Base Titration, Revisited Theory and Experiment.* Colloids Surf., A, 2012. **414**: p. 302.

35. Gibson, G.T.T., et al., *Potentiometric Titration of Metal Ions in Ethanol.* Inorg. Chem., 2006. **45**: p. 7891.

36. Sánchez, J. and M. del Valle, *Determination of Anionic Surfactants Employing Potentiometric Sensors—a Review.* Crit. Rev. Anal. Chem., 2005. **35**: p. 15.

37. Lu, S.-M., et al., *Electrochemical Sensing at a Confined Space.* Analytical Chemistry, 2020.

38. Baker, L.A., *Perspective and Prospectus on Single-Entity Electrochemistry.* Journal of the American Chemical Society, 2018. **140**(46): p. 15549-15559.

39. Wang, Y., X. Shan, and N. Tao, *Emerging tools for studying single entity electrochemistry.* Faraday Discussions, 2016. **193**(0): p. 9-39.

40. Crooks, R.M., *Concluding remarks: single entity electrochemistry one step at a time.* Faraday Discussions, 2016. **193**(0): p. 533-547.

41. Pandey, P., et al., *Probing Dynamic Events of Dielectric Nanoparticles by a Nanoelectrode-Nanopore Nanopipette.* ChemElectroChem, 2018. **5**(20): p. 3102-3112.

42. Pandey, P., et al., *Differentiation of metallic and dielectric nanoparticles in solution by single-nanoparticle collision events at the nanoelectrode.* Nanotechnology, 2019. **31**(1): p. 015503.

43. Guduru, R., et al., *Mapping the Brain's electric fields with Magnetoelectric nanoparticles.* Bioelectronic Medicine, 2018. **4**(1): p. 10.

44. Kaushik, A., et al., *MRI-Guided, Noninvasive Delivery of Magneto-Electric Drug Nanocarriers to the Brain in a Nonhuman Primate.* ACS Applied Bio Materials, 2019. **2**(11): p. 4826-4836.

CHAPTER 6: FINITE ELEMENT METHOD (FEM) BASED NUMERICAL SIMULATIONS TO UNDERSTAND NANOIMPACT EVENTS

This chapter presents the finite element based numerical simulations to understand the nanopipette experimental results as presented in Chapter 6. The contents in the chapter are from the manuscript under preparation for a peer-reviewed publication.[1]

6.1: Introduction

Charged solid-state nanopores such as nanopipettes exhibit an electrical response similar to the biological nanopores.[2, 3] Under an applied nanopore bias, the flow of ions *via* nanopore of a nanopipette generates ion current. Owing to the double layer overlap and counter ion depletion at the nanopore orifice, an interesting phenomenon, ion current rectification (ICR) is observed in the conical nanopipettes.[3-5] The ICR explains the asymmetric current-voltage (*i*-*V*) relationship for the ion transport. ICR is the deviation of *i*-*V* measurements from the ohmic behavior. In other words, the magnitude of the ion current is very different for the same voltage magnitude but opposite polarity. Importantly, the understanding ion transport mechanism is crucial in single-entity detection, manipulation, and analysis. For this, a theoretical understanding of the mechanisms that govern mass transport processes (*via* numerical simulation) under externally applied nanopore bias is very helpful.

FEM simulation solves the problems that cannot be solved using analytical solutions. There are several through simulation research reports that describe mass transport *via* nanopore of a nanopipette.[5-9] Recently, we reported the OCP detection *via* multifunctional nanopipette during the translocation of charged Gold nanoparticle through the nanopore.[10] The proteins are much smaller than the NPs and have large mobilities.

Therefore it is necessary to optimize the nanopipette geometry of quantitative measurement of OCP change at the CNE. How the NP/CNE size, bath concentration, NP/quartz surface charge densities, NP surface charge distribution, taper length, presence of nanopore near CNE, E-field distribution within the nanopore affects the local potential change on the CNE during translocation of charged GNP was computed by using coupled Poisson-Nernst-Planck equation. The Nernst-Planck equation was used for modeling the nature of ion fluxes and potential distribution with the assumption of assuming electro-neutrality and no convection.[7, 10] The Nernst-Plank equation 6.1 explains the physical properties of transport of ionic species whereas the relationship of ion concentrations with electric potential is given by Poisson's equation 6.2.

$$\boldsymbol{J_j}(x) = -D_j \nabla C_j - \frac{z_j F}{RT} D_j C_j \nabla \boldsymbol{\phi} + C_j \boldsymbol{v} \tag{6.1}$$

$$\nabla^2 \emptyset = -\frac{F}{\varepsilon} \sum_j z_j C_j \tag{6.2}$$

Where J_j, D_j , C_j , and z_j are, respectively, the flux, diffusion constant, concentration, and charge of the species j. $\boldsymbol{\phi}$ is the local electric potential. F, R, and T are the Faraday's constant, the gas constant, and the absolute temperature, respectively. The coupled Poisson-Nernst-Plank (PNP) equation together with the Naiver-Stokes equation describes the flux of charged species in the nanochannel.[5, 11]

I use finite element based numerical simulations to optimize the nanopipette geometry for single biomolecule detection and to understand the fundamental charge sensing mechanism

during nanoimpact events at the CNE and the nanopore translocations. The results presented in this section support the discussions presented in Chapter 6.

6.2: Methods

6.2.1: Simulation Geometry and Mesh Distribution

Figures 6.1 a, b present the SB and DB nanopipette FEM simulation geometry and mesh distribution. The whole simulation geometry was discretized into free triangular elements and through mesh, refinement was applied with the maximum and minimum mesh sizes were 11.11 nm and 0.08 nm, respectively.

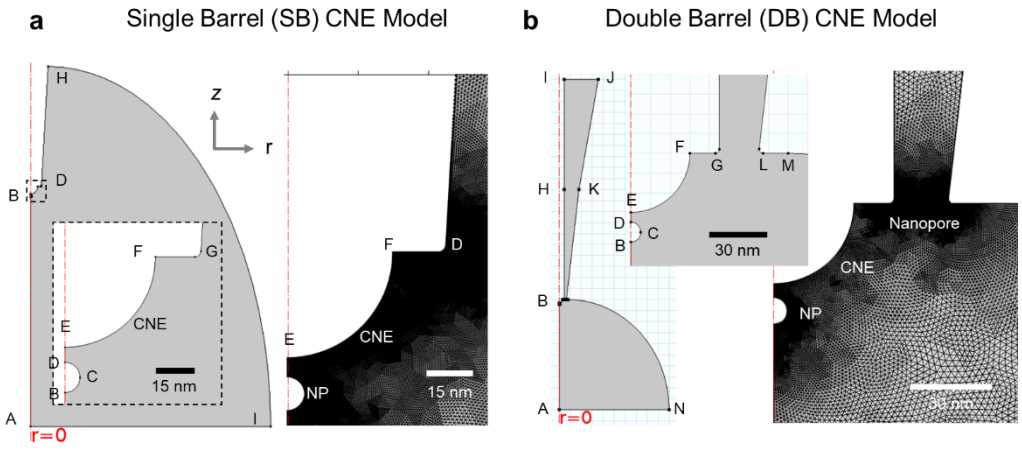

Figure 6. 1: Screenshot of FEM simulation computational domain for the NP-CNE collision (a) SB Model and (b) DB Model. The surface to surface distance from CNE and 10 nm diameter insulating NP was kept fixed at 5 nm. The zoom-in of the nanopipette apex is presented in the inset. The red vertical lines in both the geometry denote the 2D axial symmetry. The right side of each simulation geometry denotes a triangular mesh distribution near the nanopipette apex.

The FEM simulation geometry of nanopipette in this work consists of two types. First, single barrel (SB) nanopipette with carbon nanoelectrode (CNE) at the nanopipette apex (see Figure 6.1a). Second, double-barrel (DB) multi-functional nanopipette with nanopore and CNE at the nanopipette apex (see Figure 6.2 b). The potentiometric based single-entity

nanoimpact events at the CNE was monitored for both simulation geometry by varying CNE/NP sizes, quartz nanopipette/NP surface charges, nanopore bias, and bath/nanopipette electrolyte concentration.

6.2.2: Simulation Parameters and Boundary Conditions

Table 6.1 shows the FEM simulation parameters used to perform the calculation for both geometries. For both simulation geometry, the CNE (modeled as protruded hemisphere), nanopore, and NP radii were kept fixed at 30 nm, 15 nm, and 5 nm respectively unless stated otherwise. These values are used to represent the experimental conditions for protein detection. The NP and nanopipette surface charges were fixed at – 37 mC/m^2 and – 5 mC/m^2 unless mentioned otherwise. The CNE surface was allowed to float. The half cone angle was used as 6.5º for both geometries. To simplify the simulation, an electrolyte containing only two ions such as KCl is used at a concentration of 10 mM. The following table provides all the simulation parameters used and boundary conditions used for the analysis.

Table 6. 1: Simulations Parameters

Parameters	Value
Relative permittivity (ε_r)	80
Temperature (T)	298 K
Diffusion coefficient (K^+)	1.957×10^{-9} (m^2s^{-1})
Diffusion coefficient (Cl^-)	2.032×10^{-9} (m^2s^{-1})
Charge number (Z_{K^+})	1
Charge number (Z_{Cl^-})	-1
Concentration (C_{K^+})	0.01 M
Concentration (C_{Cl^-})	0.01 M
Maximum element (mesh) size	11.11 nm
Minimum element (mesh) size	0.08 nm
Maximum element growth rate	1.2
Resolution of curvature	0.3
Resolution of narrow regions	2
Number of refinements	2

Table 6. 2: Boundary Conditions (SB Model)

Surface	Poisson's Equation	Nernst- Plank Equation
AB	Axial symmetry	Axial symmetry
BCD (PSNP surface)	-37 mC/m^2 (or others), floating potential	No flux (insulation)
DE	Axial symmetry	Axial symmetry
EF (CNE surface)	No charge, floating potential	No flux (insulation)
FG (quartz)	-5mC/m^2 or 0	No flux (insulation)
GH (quartz)	-5mC/m^2 or 0	No flux (insulation)
HI	Zero charge	No flux (insulation)
IA (Ag/AgCl electrode)	Ground	Constant concentration

Table 6. 3: Boundary Conditions (DB Model)

Surface	Poisson's Equation	Nernst- Plank Equation
AB	Axial symmetry	Axial symmetry
BCD (PSNP surface)	-37 mC/m^2 or 0	No flux (insulation)
DE	Axial symmetry	Axial symmetry
EF (CNE surface)	No charge, floating potential	No flux (insulation)
FG (quartz)	-5mC/m^2 or 0	No flux (insulation)
GH (quartz)	-5mC/m^2 or 0	No flux (insulation)
HI (quartz)	Zero charge	No flux (insulation)
IJ (Ag/AgCl electrode)	Electric potential	Constant concentration
JK (quartz)	Zero charge	No flux (insulation)
KL (quartz)	-5mC/m^2 or 0	No flux (insulation)
LM (quartz)	-5mC/m^2 or 0	No flux (insulation)
MN	Zero charge	No flux (insulation)
NA (Ag/AgCl electrode)	Ground	Constant concentration

6.2.3: FEM Simulation

I carried out finite element based numerical simulations using the software package COMSOL Multiphysics 5.2a with chemical reaction engineering and AC/DC modules using Poisson-Nernst-Planck (PNP) equations. From the previous literature [9, 10, 12], we performed steady-state simulation and ignored the fluidic flow term (*i.e.*, last term $C_j\boldsymbol{v}$ in equation 6.1) for the simplifications. Though the simulation is less precise with these

simplifications, the simulation results still help us to understand the effectiveness of the potential sensing between SB and DB nanopipettes.

6.3: Results and Discussions

6.3.1: Effect of CNE and NP Size on Local Potential Change at the CNE

To understand the CNE and NP size effect on the potential change, I performed a numerical simulation using an SB nanopipette geometry. The radii of the CNE hemisphere was varied from 30 nm to 180 nm. The surface to the surface distance between NP and CNE was kept at 5 nm and 700 nm. The difference in potential (*i.e.*, $\Delta V = V_{700\ nm} - V_{5\ nm}$) was measured. Figure 6.2a presents the CNE size effect on the potential change for both geometries. We take the area ratio of NP and CNE (A_{NP}/A_{CNE}) and plotted against the potential change. The CNE with a small size was found to be more sensitive to potential change than the larger CNE size. The potential change is fairly the same for both the geometries with only 6% larger magnitude for SB than the DB geometry. This observation helped us to optimize the CNE geometry for biomolecule detection (Chapter 7). The potential change vs. the area ratio of NP and CNE (A_{NP}/A_{CNE}) is presented in Figure 6.2b. The CNE radius was kept fixed at 130 nm and the NP size was varied by keeping the surface charge density of the NP fixed at -37 mC/m^2. The potential change was found to increase with the increasing NP radius. In addition, the simulated electric field distribution vs. CNE radii in Figure 6.2c further confirms that with the increase of the CNE area, the electric field drops exponentially. Therefore, especially for protein detection, smaller CNE sizes are better for their higher potential sensitivity.

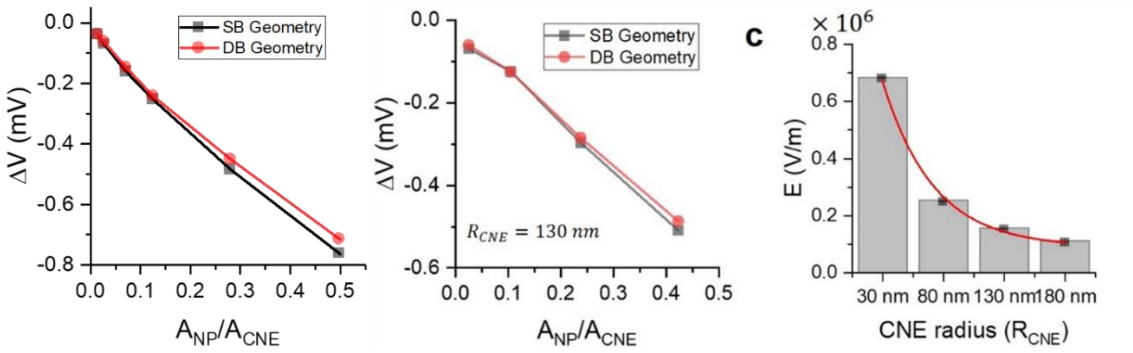

Figure 6. 2: (a) The CNE size effect on the potential change at the CNE for SB and DB geometries. The NP radius was kept fixed at 15 nm and the CNE radius was varied. (b) The NP size effect on the measured potential change. The CNE radius was kept fixed at 130 nm and NP size was varied. (c) Box plot showing E-field distribution vs. CNE radius for SB FEM model. The red solid line denotes an exponential fit to the data. In both cases, the NP and glass charge density was fixed at -37 mC/m^2 and -5 mC/m^2 respectively. For DB geometry, the nanopore bias of 0 mV was applied.

6.3.2: Effect of Nanopipette and Nanoparticle Surface Charge Density

In order to understand the nanopipette and nanoparticle surface charge density on the potential change, I performed numerical simulations on SB nanopipette geometry. Figure 6.3 shows the simulation result for DB and SB FEM models.

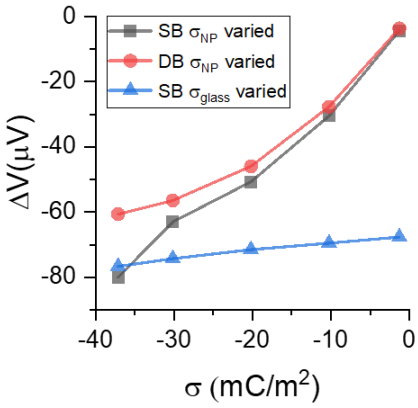

Figure 6. 3: (a) Nanopipette and NP surface charge density effect on the potential change for SB and DB nanopipette geometries. The NP was kept at 5 nm and 700 nm away from the CNE surface and the difference in potential (ΔV) was measured. The red curve is for fixed glass surface charge density (σ_{glass}) and varied NP surface charge density (σ_{NP}) for DB geometry while the black curve is for fixed σ_{NP} and varied σ_{glass} for SB geometry. The NP and CNE radius was kept fixed at 15 nm and 130 nm. The blue curve is for fixed σ_{NP} and varied σ_{glass} for SB geometry.

The ΔV found to be more sensitive to the NP surface charge density (σ_{NP}) than the glass surface charge density (σ_{glass}). With the increase of (σ_{NP}), the ΔV increased (*i.e.*, more negative) significantly (red and black curves). We attributed this increase to the double layer interaction of the NP and CNE. In contrast, the σ_{glass} was found to have a very small effect on the ΔV (blue curve). This observation is important in protein detection where the pH change of the medium is expected to change the overall σ_{glass}. We can argue that the pH-induced variation of the σ_{glass} have a negligible effect on the ΔV and that the ΔV change is mainly as a result of the σ_{NP}.

6.3.3: Advantages of DB over SB Model

The NP-CNE collision events observed in SB nanopipette geometry entirely depend on the diffusion process. The manipulation of the single entities for SB geometry is not straightforward. However, the use of DB nanopipette geometry solves these issues. In the DB model, the NP motion is governed by diffusion and migration. Additionally, the single NP events can easily be manipulated by using nanopore bias or DEP at the CNE.

Figure 6.4 presents the simulated E-field distribution results for SB and DB nanopipette geometries. The SB and DB (V_{pore} = 0 mV) models show very similarly ($\sim 1.5 \times 10^5\ V/m$) E-field distributions near the CNE apex. While on applying the 200 mV bias at the nanopore, the E-field found to increase by at least an order magnitude (Figures 6.4 b and c). The single entity motion is strongly affected by the E-field distributions near the nanopipette apex. The charged entities move opposite to the E-field direction. For negatively charged nano entities, positive nanopore bias significantly increases the motion of the single entities towards the CNE enabling high-throughput detection and analysis.

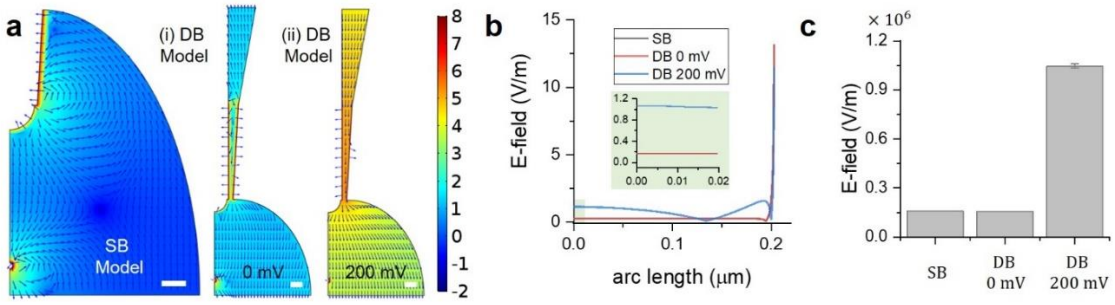

Figure 6. 4: (a) Simulated electric field (E) distribution in logarithmic scale for SB and DB ((i)V_{pore} = 0 mV and (ii)V_{pore} = 200 mV)) FEM model. The arrows in the FEM model denote the E-field directions. The scale bar is 130 nm. (b) Simulated electric field (E) distribution as a function of arc length along the CNE curvature. The E-field minimum observed in DB geometry is as a result of the interaction of the E-field produced by charged glass and NP. The maximum E-field was observed when CNE meets the charged glass surface. The inset shows the zoom-in of the 20 nm highlighted region. The average E-Field (within the highlighted region) is measured at the top of the CNE in each of the FEM models. (c) Box plot showing the E-field magnitudes at the CNE apex for SB and DB geometries. The NP and CNE radii are 15 and 130 nm respectively.

Additionally, in an experiment with DB nanopipette, CNE found to be sensitive for a prolonged time than SB nanopipette. This can also be attributed to the presence of nanopore at the CNE proximity.

6.3.4: Effect of Bath KCl Concentration

To understand the bath KCl concentration effect on the local potential change (ΔV) at the CNE, I performed simulations on SB and DB nanopipette geometries. Figure 6.5a denotes the simulation results for SB and DB models. In both the geometries, ΔV was found to have a larger magnitude at 10 mM KCl concentration than at 150 mM KCl concentration. The large ΔV at low salt concentration is as a result of a small charge screening effect (See potential distributions in Figure 6.5 b and c). The charge screening effect is higher at a high salt concentration which significantly reduces the sensitivity of the potential detection (See potential distribution in Figure 6.5 b(ii)). To confirm our simulation results, I performed experiment with 26 nm PSNP at two different KCl salt concentrations. Similar to

simulation result, the PSNP-CNE collision has large (-0.49 ± 0.13 mV) ΔV at 10 mM than at 50 mM (-0.15 ± 0.06 mV) bath KCl concentration. Owing to the higher potential sensitivity at low bath salt concentration, in the protein detection experiments, we mainly use 10 mM KCl concentration.

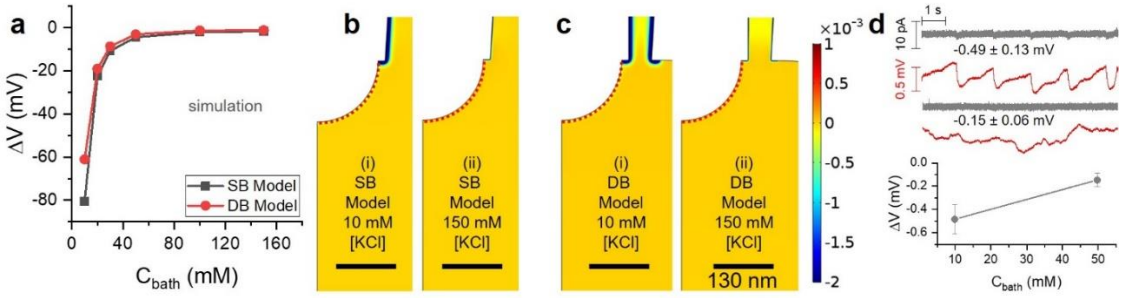

Figure 6. 5: (a) The effect of bath KCl concentration on the ΔV for SB (gray) and DB (red) nanopipette geometries. For the DB model, the KCl concentration inside the nanopipette was kept fixed at 10 mM and the nanopore bias was 0 mV. The electric potential (V) distributions for (b) SB model and (c) DB model along the CNE surface(red dotted sector) for 10 and 150 mM bath KCl concentration. The NP and CNE radii are 15 nm and 130 nm respectively. The quartz and NP surface charge densities are -5 mC/m^2 and -37 mC/m^2 respectively. The nanopore diameter of the DB model was 50 nm. (d) The experimental current (gray) and potential (red) time traces of 26 nm PSNP-CNE collsion events from a multifunctional DB nanopipette (nanopore diameter 38 nm and CNE area 0.8 μm^2).

6.3.5: Effect of Single Entity Surface Charge Distribution on Potential Change

The modal NPs such as GNPs and PS NPs have identical and uniformly distributed charged species. Owing to their uniformity in size and charges, the detection and analysis of these NPs are much simpler. The biomolecules such as proteins, in contrast, have non uniformly distributed charged groups called amino acid (AA) residues. The surface of a typical protein consists of exposed positive, negative, hydrophobic, and polar AA residues. The number of total positive and/or negative exposed AA residues determines the protein net charge in the aqueous solution.

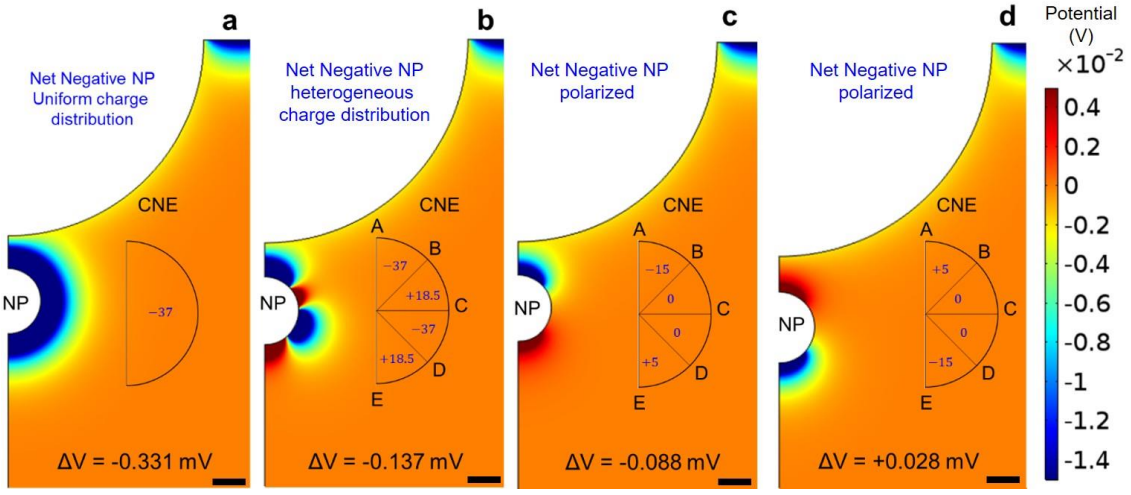

Figure 6. 6: The effect of NP surface charge distribution on the potential change ($\Delta V = V_{700\ nm} - V_{5\ nm}$) for the SB model. (a) Electric potential distribution along the CNE surface when (a) net negative, uniformly charged NP (b) net negative, non-uniformly charged NP (c) net negative and polarized NP facing negatively charged side to the CNE (d) net negative and polarized NP facing positively charged side to the CNE. The scale bar is 5 nm. The NP is at 5 nm away for the CNE in all the cases. The NP and CNE radii were kept fixed at 5 nm and 30 nm. The inset shows the simulated charge density distributions on the NP surface in mC/m^2.

To understand the heterogeneous charge distribution on potential change, I performed FEM simulation with SB nanopipette geometry (R_{CNE}=30 nm and r_{NP}=5 nm). The CNE and the NP sizes were reduced to mimic the experimental condition. The NP is modeled to have a uniform and non-uniform charge densities on its surface as shown in the insets in Figures 6.6. In Figure 6.6 a, entire NP has uniform -37 mC/m^2 charge density. For model 6.6 b, c and d, the entire NP was divided into four 45 degree sectors containing different charge densities as shown in the figure. Figures 6.6 a, b, c, and d respectively present the electric potential distribution at the CNE periphery as a result of uniform negatively charged, heterogeneous negatively charged, polarized with negatively charged side facing the CNE and polarized with positively charged side facing the CNE.

The ΔV for uniform negatively charged (-37 mC/m^2) NP was found to be larger than the heterogeneous negatively charged (-37 mC/m^2) (see Figure 6.6 a and b). This observation suggests that higher potential sensitivity can be achieved for NP with uniform surface charge density. Though NP has the same (-37 mC/m^2) charge density in Figures 6.6 a and b, the presence of a positively charged region on the NP significantly reduced the potential magnitude. Since proteins have heterogeneous charge distribution on their surfaces, these results will help us to understand the single proteins collision events at the CNE (see Chapter 7).

Figures 6.6 c and d present the electric potential distribution at the CNE vicinity when a polarized but net negatively charged (-10 mC/m^2) NP approach at 5 nm away from the CNE. In Figure 6.6 c the negative side of the NP was faced towards the CNE and in Figure 6.6 d, the positive side of the NP was faced towards the CNE. Simulation results suggest that when the negative side (-10 mC/m^2) of the NP faces the CNE, the polarity of the ΔV was negative (-0.088 mV) which confirmed that the NP has a net negative surface charge. However, when the positive side (+5 mC/m^2) of the NP faces the CNE, ΔV has a positive value (+0.028 mV) suggesting that the NP has a net positive charge. This result suggests that the mechanism of potential sensing entirely depends on the surface charge of the single entities. A small variation in the surface charge density can easily change the polarity of the ΔV. These results were very crucial in explaining why a net negatively charged protein at a constant pH show positive and negative potential changes during nanoimpact at the CNE (see Chapter 7).

6.3.6: Nanopipette Taper Length Effect on Potential Change During Nanopore Translocation Events

To understand the nanopipette taper length (length shown in double-headed black arrows in Figure 6.7) effect on the local CNE potential, I performed FEM simulation using a DB nanopipette geometry. The geometry of the short tapered (ST) and long tapered (LT) nanopipettes are shown in Figures 6.7 a, b. The

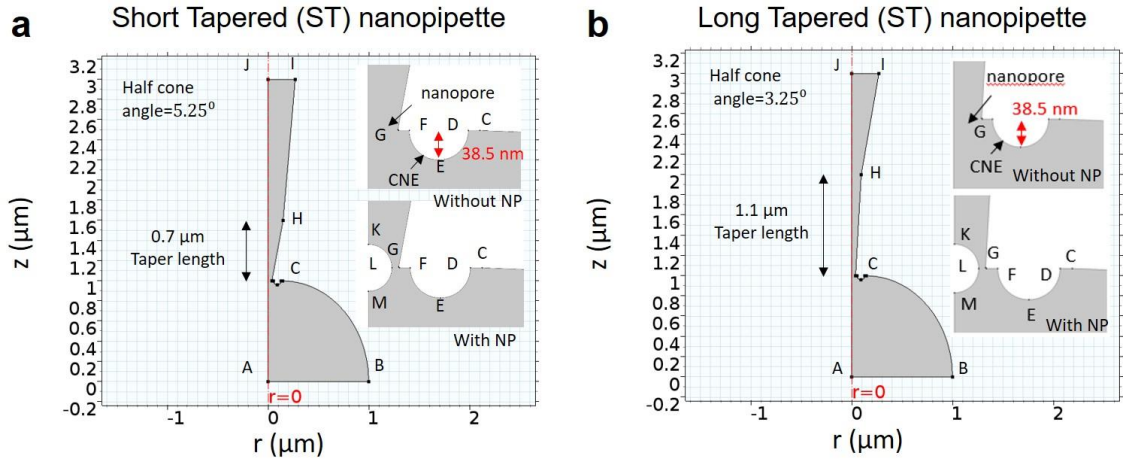

Figure 6. 7: (a) The ST and LT nanopipette simulation geometry. The ST and LT nanopipettes have 0.7 µm and 1 µm taper lengths and the half cone angles are 10.5 and 6.5 degrees respectively. The region near the nanopipette pore is shown in zoom in. A DB simulation geometry was used here.

CNE, NP, and the nanopore radii were fixed (see Figures 6.7) for both the geometries. The half cone angle and the taper lengths were different for ST and LT geometries.

The nanopipette taper length variation changes the net negative charge of the nanopipette. Similarly, change in half cone angle alters the length of the nanochannel where charged NPs interact with the charged nanopipette wall. Figure 6.8a denotes the electric potential distributions for an LT and ST nanopipette geometries with/without an NP at the nanopore mouth. The measured potential change for LT and ST nanopipette geometries was – 1.56

mV and -2.24 mV respectively. The ΔV for LT geometry was found to be ~30% higher than the ST geometry. This result suggests that higher potential sensitivity can be achieved using ST nanopipette than LT geometry. This can be attributed to the low surface charge screening effect of an ST than LT geometry as conformed by the extended potential distribution away from pore mouth for ST geometry (Figure 6.8 (iii) and (iv).

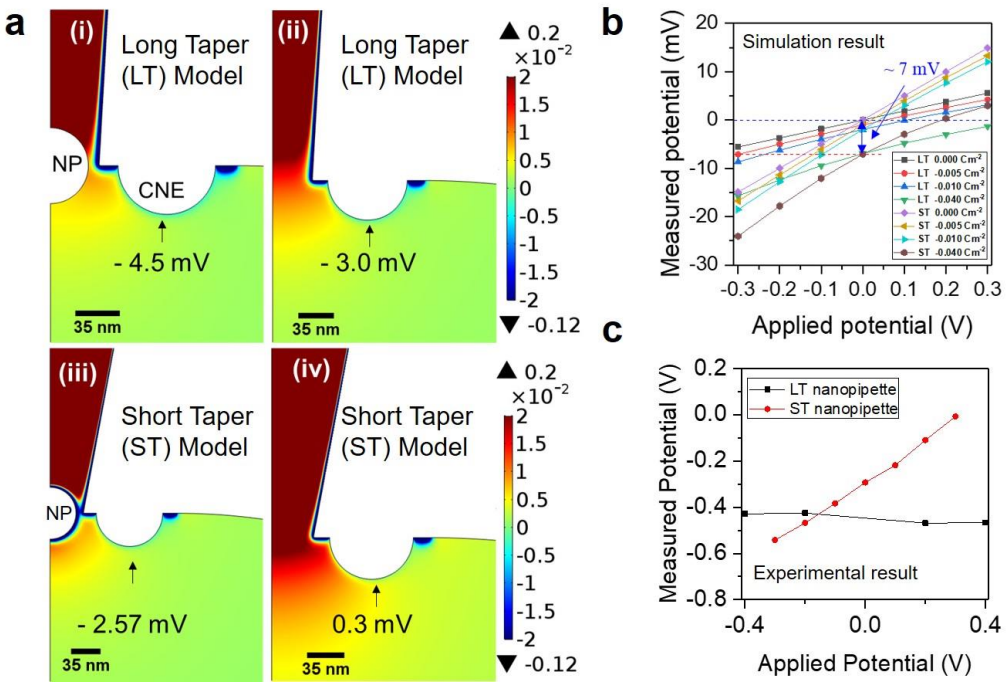

Figure 6. 8: (a) Nanopipette taper length effect on the CNE potential detection. Potential distribution maps presented in (i) and (ii) are from LT nanopipette and (iii) and (iv) are from ST nanopipette. LT and ST nanopipettes have 1 um and 0.7 um taper length respectively. The nanopore bias and is +200 mV and the glass and NP surface charge densities were -0.04 C/m^2 and -0.072 C/m^2 respectively. The PSNP, CNE, and nanopore respectively have 30 nm, 38.5 nm, and 38.5 nm radii. (b) Effect of taper length (glass surface charge variation) on potential change for ST and LT simulation geometry. (c) The experimental result showing applied *vs.* measured potential baseline change for ST and LT nanopipette geometry.

Figure 6.8 b shows the simulation result for LT and ST nanopipettes with varied glass surface charge density. The result suggests that the electric potential is more sensitive to the applied nanopore bias for ST geometry than LT geometry owing to the small charge

screening effect. This simulation result is supported by the experimental result shown in Figure 6.8c.

Owing to the ST geometry, it has a small glass surface charge density and nanopore bias extends to a much larger region away from the pipette apex as a result of poor glass surface charge screening effect. Thus capture radius is larger and hence NPs can be effectively accumulated near the nanopipette apex. Thus, NP events can be acquired easily, within <5 minutes after addition of the NPs and do not require DEP trapping. Under nanopore bias alone, the ST geometry nanopipette produces dominant nanopore translocation events with higher event rates than CNE collision events. This is because the electrophoresis is much stronger than the Coulomb repulsion force. However, as a result of rapid NP accumulation near the apex, ST geometry nanopipette often shows complicated collision and translocation events.

In contrast, LT nanopipette geometry has a long narrow channel, more glass surface charge effect, and effective glass surface charge screening. This makes LT nanopipettes less sensitive to applied nanopore bias and thus have a small capture radius. Therefore, the NP accumulation process is slow and usually take > 30 minutes to observe first Single NP events. The advantage of LT geometry is that it allows us to detect single entities with less interference with the neighboring NPs. We will continue to use LT geometry of smaller nanopore and CNE sizes for single protein detection (see Chapter 7).

6.4: Conclusions

The numerical simulation results showed that the open circuit potential (OCP) change at the CNE during nanoimpact was affected by factors such as NP/CNE size, nanopipette/NP

surface charge, electrolyte concentration, and externally applied bias. The numerical simulation results were very useful to understand the fundamental charge sensing mechanism for both SB and DB nanopipette geometry. Additionally, the simulation results were also useful in optimizing the nanopipette (especially the CNE) geometry for the small biomolecule detection.

6.5: References

1. Pandey, P. and J. He, *Understanding potentiometric nanoimpact events via finite elelment method based numerical simulation.* 2020.

2. Ho, C., et al., *Electrolytic transport through a synthetic nanometer-diameter pore.* Proceedings of the National Academy of Sciences of the United States of America, 2005. **102**(30): p. 10445.

3. Siwy, Z., et al., *Conical-Nanotube Ion-Current Rectifiers: The Role of Surface Charge.* Journal of the American Chemical Society, 2004. **126**(35): p. 10850-10851.

4. Siwy, Z.S., *Ion-Current Rectification in Nanopores and Nanotubes with Broken Symmetry.* Advanced Functional Materials, 2006. **16**(6): p. 735-746.

5. White, H.S. and A. Bund, *Ion Current Rectification at Nanopores in Glass Membranes.* Langmuir, 2008. **24**(5): p. 2212-2218.

6. Perry, D., et al., *Characterization of Nanopipettes.* Analytical Chemistry, 2016. **88**(10): p. 5523-5530.

7. Sa, N., et al., *Rectification of Ion Current in Nanopipettes by External Substrates.* ACS Nano, 2013. **7**(12): p. 11272-11282.

8. German, S.R., et al., *Controlling Nanoparticle Dynamics in Conical Nanopores.* The Journal of Physical Chemistry C, 2013. **117**(1): p. 703-711.

9. Lan, W.-J., et al., *Nanoparticle Transport in Conical-Shaped Nanopores.* Analytical Chemistry, 2011. **83**(10): p. 3840-3847.

10. Panday, N., et al., *Simultaneous Ionic Current and Potential Detection of Nanoparticles by a Multifunctional Nanopipette.* ACS Nano, 2016. **10**(12): p. 11237-11248.

11. Lan, W.-J., et al., *Effect of Surface Charge on the Resistive Pulse Waveshape during Particle Translocation through Glass Nanopores.* The Journal of Physical Chemistry C, 2014. **118**(5): p. 2726-2734.

12. Snowden, M.E., et al., *Scanning Electrochemical Cell Microscopy: Theory and Experiment for Quantitative High Resolution Spatially-Resolved Voltammetry and Simultaneous Ion-Conductance Measurements.* Analytical Chemistry, 2012. **84**(5): p. 2483-2491.

CHAPTER 7: POTENTIOMETRIC DETECTION OF SINGLE PROTEIN MOLECULES IN SOLUTION VIA NANOIMPACT METHOD

This chapter demonstrates the use of a multifunctional nanopipette as a highly versatile and sensitive nanoscale tool for probing single biomolecules. This work implements two highly emerging electrochemical nanodetectors (nanopore and nanoelectrode) to simultaneously monitor the ionic current and local potential changes at the nanopore and the nanoelectrode when a protein translocates through the nanopore or collides with the nanoelectrode. This chapter presents a facile potentiometric method of detecting protein at the single-molecule level in solution using the nanoimpact events of proteins at the nanoelectrode, which will be further supported by molecular dynamics (MD) simulation. The proposed methodology is the simplest yet highly sensitive technology developed to study interactions at the single molecular level. The contents presented in this chapter are from my manuscript which is currently under preparation.[1, 2] Only ferritin-CNE and cytochrome-c-CNE nanoimpact events have been briefly discussed here to demonstrate the sensing capability and to validate the method.

7.1: Introduction

Proteins are ubiquitous and play a critical role in all aspects of life. The structure and composition of the protein molecules determine its functions.[3, 4] Therefore a thorough investigation of protein molecules at a single molecule level is essential to characterize them in aqueous solution. However, facile, cost-effective, and versatile multi-mode detection of proteins at a molecular level in aqueous solution remains challenging, and highly sensitive and efficient sensing approaches are still limited.[5, 6] There are several bio-sensing platforms available to detect and characterize the single biomolecules.[7]

Various nanopore and nanoelectrode based sensing platform,[8-16] optical microscopy methods,[17] optical/magnetic tweezers,[18, 19] atomic force microscopy (AFM),[20-22] nanomaterial functionalized nanopores/nanoelectrodes, have shown remarkable performance and therefore have widely used in protein sensing and characterization. The beauty of the single entity measurement is that it requires a very small sample volume and provides single-molecule information one at a time, unlike the traditional ensemble measurement. Besides, the single-molecule study provides insight into molecular mechanisms, molecular heterogeneity within the sample and gives opportunities to develop protein-based molecular diagnostics for biomedical applications. Among these techniques, nanopore and nanoelectrodes based electrochemical methods are at the forefront.

In recent years, nanopores and nanoelectrode based electrochemical single entity detection and analysis methods have become increasingly popular as a versatile yet simple tool in the field of nanoscience for probing biomolecules at the nanoscale.[6, 9, 23-25] By monitoring ionic current change induced by the single-entity translocation event, the shape, charge, and even dynamic orientation of NP can be revealed.[26-30] Similarly, the electrochemical nano impact method enables us to detect, characterize, and quantify the various single-entities including biomolecules.[31-34] Besides, nanoimapct method provides rich single-entity information about the inter-particle interactions and the aggregation of NPs in the solution/nanoelectrode surface, the redox reaction kinetics of catalytic NPs and electroactive species at the surface of NPs, and the surface chemistry of NPs.[24, 35, 36]

Owing to the ease in the manipulation of the nanoelectrode potential, the majority of the reported single-entity nanoimpact experiments implement the amperometric method. The electrochemical current produced during amperometric nanoimpact experiments are very small and often require redox-active molecules and/or catalytically active NPs for signal amplification.[37-42] As the amperometric nanoimpact experiments are often performed in the presence of the foreign molecules, there is more contamination and biomolecules/nanoelectrode deactivation/passivation issues. It has been demonstrated that the single metallic nanoparticle nanoimpact events can also be sensed by the open-circuit potential (OCP) change (potentiometric method) at the UME.[41] Our group has also demonstrated the effective generation and potentiometric detection of single-NP nanoimpact events at the nanoelectrode in solutions using a nanopore–nanoelectrode nanopipette.[43] The potentiometric method of single-entity detection is a facile and versatile single entity measurement method that does not require extra signal amplification method, has less contamination and single-entity deactivation issues, and small electrical noise. Given these advantages of the potentiometric method over an amperometric method, it is worth to be utilized in single biomolecules investigation.

In this work, we demonstrate we demonstrate the facile potentiometric method of detecting electrochemically inactive single bio-macromolecules, such ferritin, and cytochrome-c protein, by sensing open circuit potential (OCP) change when they approach towards and/or collides with and/or scatter away from the carbon nanoelectrode of the multifunctional nanopipette. These collision events were characterized by Hit-and-Run type of collisions of the biomolecules onto the nanoelectrode surface. By inducing high throughput collisions of biomolecules on the CNE (radius < 20-180 nm), time-resolved,

discrete collision events can be unambiguously differentiated from the background. Besides, by analyzing the shape and magnitude of the potential and its time derivative, qualitative information on the proteins' motion and net charge contained by a single protein can be obtained. We further demonstrated the charge sensing capability of the multifunctional nanopipette by studying the pH-induced variation of the net charge content of a single protein molecule. Ultimately, the OCP based sensing methodology is the simplest yet highly sensitive single-molecule detection technology developed to study the biomolecules at the single molecular level.

7.2: Experimental Methods

The nanopipette fabrication and characterization, electrical measurement, and data analysis method for the single biomolecule detection is presented in method Chapter 2, section 2.4. The nanopipette was optimized for protein detection using Finite Element based numerical simulation (see Chapter 6).

7.2.1: Materials and Reagents

ACS grade chemicals (e.g., Phosphate Buffer Saline (PBS) for pH 7.3-7.5, Potassium Chloride (KCl)) were purchased from Fisher Scientific and used without any further purification. All the proteins used in the experiment were purchased from the millipore sigma. The high (~10), medium (~7), and low (~4) pH of the solution is adjusted using carbonate, phosphate, and acetic acid buffer (see subsection 7.2.3 for more detail). All the buffer ingredients were bought from Fisher scientific. The 3-cyanopropyldimethlychlorosilane for nanopipette surface modification is obtained from

Fisher Scientific. Redox molecule Hexaaammineruthenium (III) chloride [Ru $(NH3)_6Cl_3$] (98 % pure) was purchased from Sigma-Aldrich.

7.2.2: Molecular Dynamics (MD) Simulation

The cubic X-ray crystal structure for horse spleen apo-ferritin was taken from Protein Data Bank (PDB ID: 1IER) which exists in monomeric form. The cadmium ions and water present in the crystal structure were not considered for the simulation process. The structure consists of a total 174 residues. Similarly, the structures for two heme proteins cytochrome C and bovine hemoglobin were also extracted from Protein Data Bank (PDB ID: Cyt C: 1HRC, Bhgb: 2QSP). For both, the proteins heme group were taken into consideration for simulation. Three different systems were set up using the Solution builder plugin under *Charmm-gui* webserver. We performed all-atom molecular dynamics simulation using NAMD 2.12[44] along with the CHARMM36 force field and in explicit water. Particle Mesh Ewald (PME) was used to treat electrostatic interactions and the SHAKE algorithm was employed to constrain the covalent bonds. Before performing production run all three systems were well minimized and equilibrated for 100,000 steps. The simulation time step was set to 2 fs for the production runs. To control pressure, the Nose-Hoover Langevin-piston method with a piston period of 50 fs and decay of 25 fs was used. The temperature was controlled using Langevin temperature coupling with a friction coefficient of 1 ps-1. The production run was performed for 500 ns and the images were rendered using VMD software.

7.2.3: Preparation of Different pH Buffer Solution

The 10 mM KCl used in the study was adjusted to have different final pH using corresponding buffer solutions. To prepare pH 3.8, 7.2 and 10.9, acetic acid (pKa = 4.76), phosphate (pKa = 7.20) and carbonate (pKa=10.25) buffer was used respectively. First, dilute ~100 mM concentration of all buffer solution was prepared. Then, the pH of 10 mM KCl was adjusted by pipetting a small amount of buffer solution step by step until the pH meter reads the desired value. The prepared buffer maintains the same pH for about 2 days. Afterward, the pH of the buffer needs recalibration.

7.3: Results and Discussions

7.3.1: Experimental Setup and Mechanism of Probing Net Charge of Protein Molecules

The long taper nanopipette is used intentionally to create a large entrance barrier at the nanopore apex. By tuning the entrance barrier of the nanopore, different types of single entity signals (translocations or collisions) can be generated. The big entrance resistance of nanopore allows biomolecules to spend a longer time near the nanopipette apex resulting in high throughput single-molecule events while single-molecule event throughput significantly reduced for nanopipette with small entrance barrier.

Though we occasionally observe the single protein translocation events through the nanopore of diameter $d<20$ nm, here we mainly focus on the dominant event type: proteins collision at the CNE for $20\text{ nm} > d > 180\text{ nm}$. As we have reported earlier, the net charge contained by the analyte of interest plays a major role in the detected potential characteristics.[43, 45, 46] The sample with net negative surface charge often increases (more negative) the potential as it approaches the negatively charged CNE.

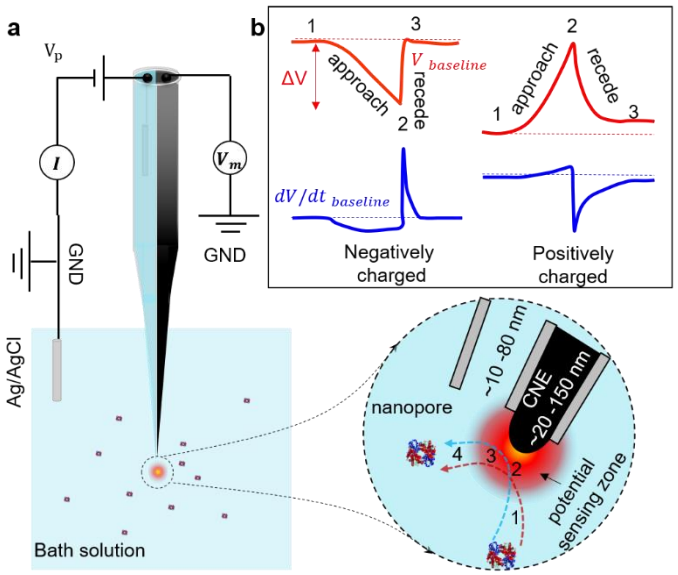

Figure 7. 1: (a) The schematic experimental setup of nanopore-CNE nanopipette used for simultaneous measurement of current (*i*) and potential (V) during the protein's motion in the bath solution.[43] The bath solution is grounded and V_p is the bias applied to the nanopore barrel filled with 10mM PBS solution. A high impedance differential amplifier connected to CNE is used to measure potential (V_m). The gradient red-colored region around the nanopipette apex represents the potential sensing zone of the nanoelectrode. Proteins are suspended in the bath solution. (b) The single protein net positive and negative charge sensing mechanism *via* nanoimpact method. Red and blue curves represent the potential and its derivative.

The experimental setup and cartoon picture of the 3-step potential shape are presented in Figures 1a and b respectively. The protein enters the potential sensing zone at position 1 and it gets accelerated by the large electric field to the position 2. The region 1-2 is defined as the approach section of the protein-CNE collision. The analysis of the slope of this potential provides qualitative information on the approach speed of the protein towards the CNE. Position 2 is the closest distance at which protein reaches to the CNE. The protein then scatters away (no physical contact) from the CNE as a result of electrostatic repulsion at position 2-3. The potential amplitude (ΔV) gives qualitative information about the net charge carried by the protein. Finally, at position 3, the protein escapes the potential sensing zone and the potential baseline returns the initial value.

What will be the motion of an entity if it has a net positive charge? The schematic of the 3-step potential characteristics for a positive single entity colliding at the CNE is presented in Figure 1b. At position 1, the protein is just at the boundary of the sensing zone and the potential baseline is constant. As it enters the sensing zone, the potential decreases (less negative) gradually. This is as a result of the oppositely charged particle approaching the CNE. In the region 1-2, the protein deaccelerates as it approaches the CNE as a result of the repulsive force of nearby proteins. After that, the protein gradually scatters away (no physical contact) from the CNE (region 2-3) and the potential baseline reaches the initial value. For net positive proteins, protein at the vicinity of the CNE likely repel the incoming proteins or as a result of constant ionic flux through the nanopore, the path of the protein deviates. In addition, for the small nanopore, electroosmosis also plays a role to scatter away from the proteins from the CNE.

7.3.2: Dynamic Variation of Protein Surface Charge at pH 7.0: MD Simulation

Proteins are complex biological entities. In solution, the amino acid residues exposed on the surface of the proteins determines its net charge.[3, 4] It has been reported that the charge distribution on the protein surface is heterogeneous. The net positive/negative charge in the protein arises as a result of the net exposed positive/negative amino acid (AA) residues on the surface of the proteins. If the number of the exposed negative AA residues are more than positive AA residues, then the protein is negatively charged. Since the variation of the surface charge of the protein is related to its function, it is very crucial to probe these variations.

To probe the single protein surface charge fluctuation dynamics in solution, we use molecular dynamics (MD) simulation. Figure 2a presents the electrostatic potential map of the two proteins used in the study. The distribution of the charged residues is not uniform throughout the surface of the protein for both the proteins. An electrostatic potential map of a ferritin monomer shows distinct positive and negative AA residues patches on the surface. Similarly, cytochrome-c (Cyt-c) has more positive AA residues (blue) exposed on the surface but also has a few negative AA residues (red). This heterogeneous distribution of AA residues on the protein's surface affects the nanoimpact events (see Chapter 6 and section 7.3.4).

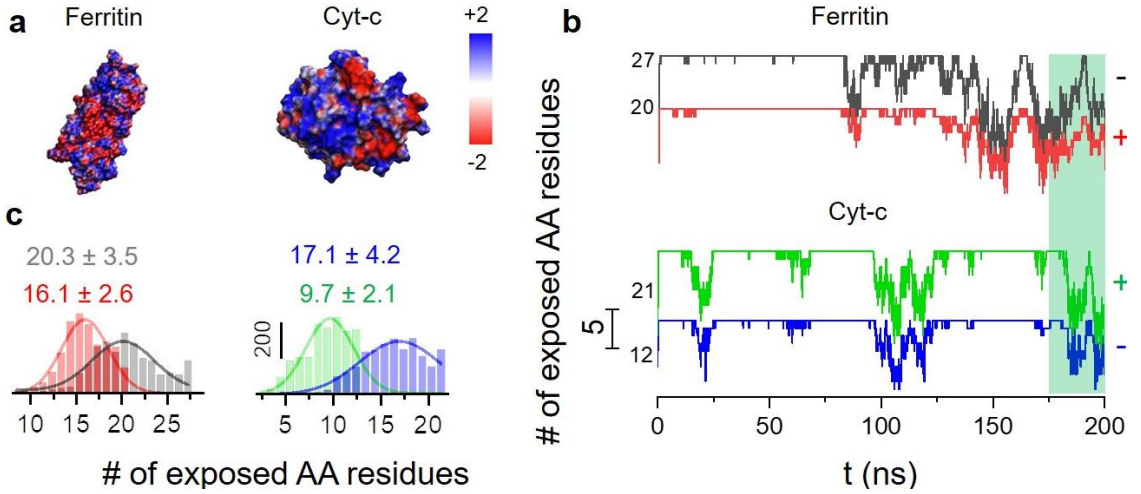

Figure 7. 2: Computational analysis of the net surface charge contained by the proteins. (a) Electric potential map of the ferritin and cytochrome-c proteins. The blue and red color denotes the positive and negative amino acid (AA) types (b) The dynamic variation of the number of exposed AA residues on the protein surface. The (+) and (-) symbol denote the positive and negative AA residues. (c) The histograms of the number of exposed AA residues on the protein surface from last (green highlighted region in b) 25 ns of the simulation. The solid lines in the histograms are the Gaussian fits.

Figure 2b shows the fluctuation of the number of exposed positive and negative AA residues for ferritin and Cyt-c protein over 200 ns time. There is a fluctuation of at least 8 AA residues for both ferritin and Cyt-c. To quantify this, we analyze the last 25 ns of data

(green highlighted region) and present as histograms. Figure 2c shows corresponding histograms for each protein. On average, a ferritin monomer has an excess of 4 negative AA residues exposed on their surface while Cyt-c has an excess of 7 positive AA residues exposed on their surface. Thus, 44% of exposed AA residues are positive for ferritin and 63% of exposed AA residues are positive for Cyt-c. We further use Protein Calculator *v3.4* for the theoretical estimation of net charge of the proteins at different pH of the surrounding medium. The ferritin is very negative at pH 7 with a charge of ~-5.7e (1 of 24 monomers) while the Cyt-c exhibits positive (~+9.6e) charge at pH 7.0. Note that these values are estimated from the full structure of Cyt-c and just 1of 24 monomers of ferritin. Thus, considering the full structure of the proteins, the ferritin is highly negative and Cyt-c is positive at pH 7.

7.3.3: Single Ferritin Protein-CNE Collision at pH 7.2

To validate the nanoimpact based potentiometric detection of single ferritin protein using a multifunctional nanopipette, we first studied the negatively charged ferritin-CNE nanoimpact events at V_{pore}= 0 mV. Ferritin is the globular protein of ~11 nm diameter in size and has an isoelectric point of 5.41. Under neutral pH conditions, ferritin acquires a net negative charge (see MD simulation section 7.3.2).

Figure 7.3a shows the typical negatively charged ferritin-CNE nanoimpact (collision) events at pH 7.2. The collision events are characterized as a fast approach (downward) and rebound (upward) motion with no current (gray) changes. While the translocation event (Figure 7.3b) often has an obvious current spike and much larger potential dip amplitude (ΔV) and at least 2 times larger potential slope. The potential and its derivative (dV/dt)

have features similar to the schematic shown in Figure 7.1b. Figure 7.3c and d denote the event rate (/s) as a function of time and diffusion coefficient plot. The event rate has a maximum at ~22.5 events/s and the corresponding diffusion coefficient from the experiment is ~85.22 cm^2/s which is at least an order magnitude larger than the theoretical diffusion coefficient (~2 cm^2/s). Therefore, in addition to the diffusion, migration of protein as a result of the electrophoresis may have contributed to the increased event rate. The ionic flux *via* nanopore further manipulates the proteins near the CNE yielding more collision events. The statistical analysis of the ΔV is shown in Figure 7.2e. The mean potential amplitude of the ferritin protein-CNE collision at pH 7.2 is ~1.78 ± 0.97 mV. The majority (~95%) of the collision events observed have a downward potential dip (as shown in schematic Figure 7.1b) which is attributed to the large negative surface charge of the ferritin protein.

Now, to observe the collision events as a result of a net positively charged protein, we use cytochrome-c (Cyt-c). Cyt-c is a globular protein of ~3.1 nm in diameter and has a pI of 10.2. At pH 7.2, it has a net positive charge (see MD simulation section 7.3.2).

Figure 7.3 presents a typical Cyt-c-CNE nanoimpact events at the CNE at V_{pore}= 0 mV and 7.2 pH. The shape of the potential and its slope is very different than that of the negatively charged ferritin protein. The approach section of the collision event is gradually decreasing

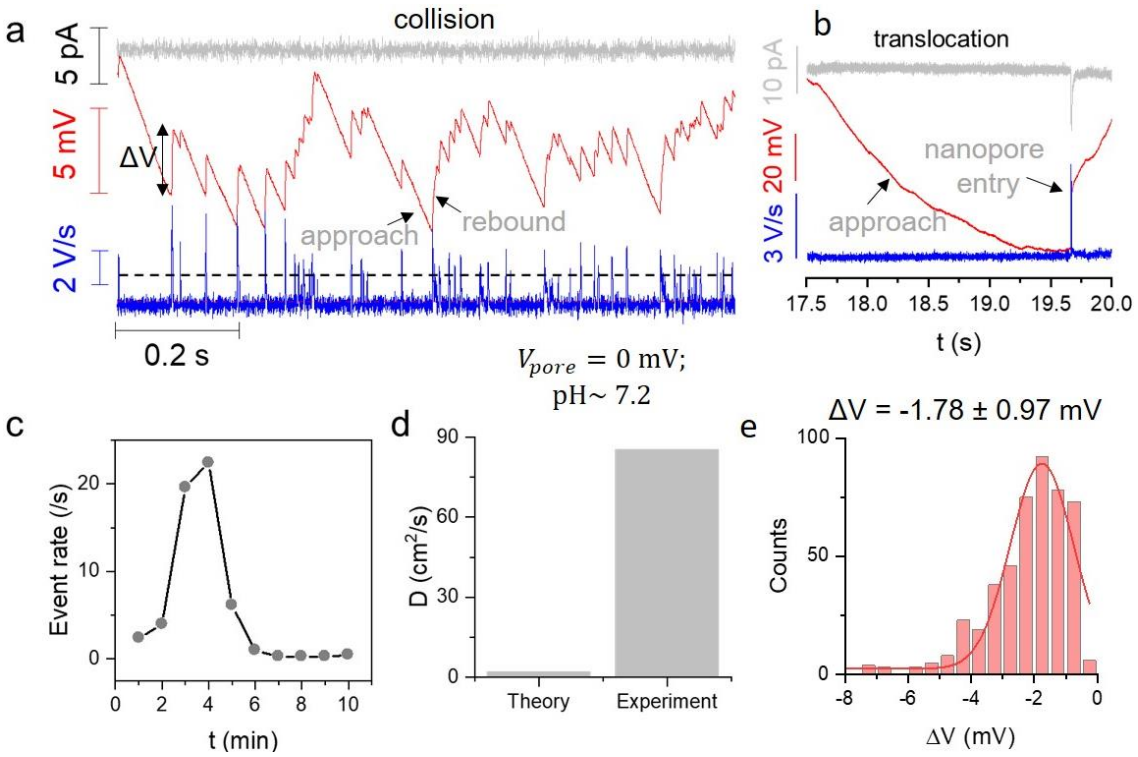

Figure 7. 3: The ferritin-CNE collision events at pH 7.2 and V_{pore} = 0 mV. (a) Current (gray), potential (red) and potential slope (dV/dt) (blue) time traces of ferritin-CNE collision. (b) Single ferritin nanopore translocaton event. The two gray arrows in a and b denote the approach and rebound motion of the protein. (c) Event rate (/s) as a function of time. Each data points are averaged over 1 minute. (d) The bar graph showing the experimental and theoretical diffusion constant (D). (e) The potential dip histogram of ferritin-CNE collision event. The solid lines in the histograms are the Gaussian fits.

(less negative) while the rebound section is gradually increasing (more negative). This behavior is exactly opposite to that of the ferritin protein. The potential amplitude analysis is shown in Figure 7.4b. The mean amplitude is ~1.01 ± 0.44 mV which is positive. The majority (~65%) of the potential amplitudes are positive nature. The rest showed a negative nature. Using these potential and dV/dt shapes and amplitudes we can acquire the qualitative information about the net charge of the impacting biomolecules in the solution. Here, the potential change is mainly as a result of the net charge of the proteins and not as a result of the charge of the nanopipette wall (see Chapter 6).

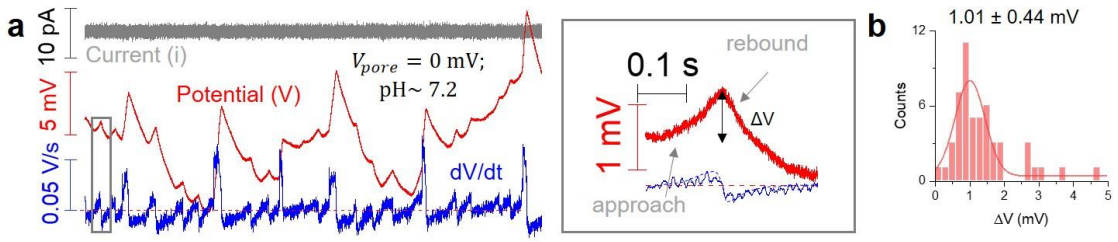

Figure 7. 4: The Cyt-c-CNE collision events at pH 7.2. (a) Current (gray), potential (red) and potential slope (dV/dt) (blue) time traces of Cyt-c-CNE collision. The zoom-in of a single collision event is shown in right. The two black arrows in zoom-in denotes the approach and receding motion of the protein. (b) The Cyt-c-CNE collision event histogram. The solid lines in the histograms are the Gaussian fits. The nanopore bias was 0 mV and bath pH was maintained at 7.2. ΔV denotes the potential amplitude. The CNE has 133 nm radius.

Figure 7.3 presents a typical Cyt-c-CNE nanoimpact events at the CNE at V_{pore}= 0 mV and 7.2 pH. The shape of the potential and its slope is very different than that of the negatively charged ferritin protein. The approach section of the collision event is gradually decreasing (less negative) while the rebound section is gradually increasing (more negative). This behavior is exactly opposite to that of the ferritin protein. The potential amplitude analysis is shown in Figure 7.4b. The mean amplitude is ~1.01 ± 0.44 mV which is positive. The majority (~65%) of the potential amplitudes are positive nature. The rest showed a negative nature. Using potential and dV/dt shapes and amplitudes we can acquire the qualitative information about the net charge of the impacting biomolecules in the solution. Here, the potential change is mainly as a result of the net charge of the proteins and not as a result of the charge of the nanopipette wall (see Chapter 6).

7.3.4: pH Effect on Net Charge of Protein Molecules

The ferritin-CNE and Cyt-c-CNE collision events respectively provide us an understanding of the potential change when a net charge of the protein is negative and positive. To further

demonstrate the capability of the nanoimpact based potentiometric detection of the biomolecules, we changed the pH of the bath solution

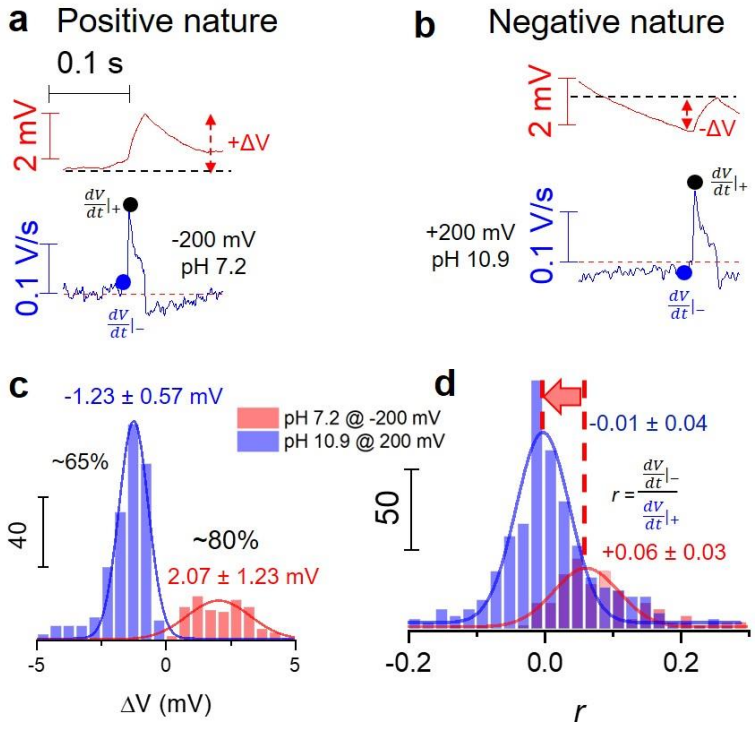

Figure 7. 5: The Cyt-c-CNE collision events at pH 7.2 and 10.9. Current (gray), potential (red) and potential slope (dV/dt) (blue) time traces of Cyt-c-CNE collision at (a) pH 7.2 (b) pH 10.9. The ΔV denote the potential amplitude. The balck and blue dots denote the dV/dt values at the approach and rebound section of the potential. (c) The histograms showing the potential dip amplitude at pH 7.2 and 10.9. The mean potential amplitudes at pH 7.2 and 10.9 are 1.23 ± 0.57 mV and -2.07 ± 1.23 mV respectively. (d) The histograms showing the ratio (*r*) between approach potential slope $\frac{dV}{dt}|_{-}$ and rebound potential slope $\frac{dV}{dt}|_{+}$. The r values for Cyt-c-CNE collision at pH 7.2 and 10.9 are -0.01 ± 0.04 and 0.06 ± 0.03 respectively. The solid lines in the histograms are the Gaussian fits.

and monitor the potential change. We use Cyt-c at pH 7.2 and pH 10.9 conditions. The pH of the bath solution is adjusted by adding a buffer solution (see Section 7.2.3) At pH 7.2 Cyt-c has a net positive charge and at pH 10.9 Cyt-c has a net negative charge.

Figure 7.5a shows a Cyt-c-CNE collision event at pH 7.2 and V_{pore} = -200mV. The shape of the potential and its slope are positive. Similarly, Figure 7.5b shows a Cyt-c-CNE

collision event at pH 10.9 and V_{pore} = +200mV. The shape of the potential and its slope are negative. We further analyze the potential change induced at pH 7.2 and pH 10.9. Figure 7.5 c presents the histogram of potential dip amplitudes at these bath pH values. At pH 7.2 ~80% of the events are of a positive type and rest are of a negative type. While at pH 10.9, ~65% of the events are of a negative type, and rest is of positive type. Observation of positive and negative types of potential dips at the same pH can be attributed to the inhomogeneous surface charge distribution in the proteins. In addition, we observe ~40% smaller potential dip magnitude at pH 10.9 than at pH 7.2. This is attributed to the large Colomb repulsion between protein and the CNE at pH 10.9. The potential slope analysis at pH 7.2 and 10.9 are presented in Figure 7.5d. The parameter *r* is defined in Figure 7.5d. Larger negative *r* value suggests the faster approaching motion and larger positive *r* value suggests the faster rebounding motion of the protein. The *r*-value has positive (0.06 ± 0.03) value for positive nature potential dips and negative (-0.01 ± 0.04) for the negative type of potential dips. The motion of the protein reversed from a slow approach to a fast approach motion when pH was changed from 7.2 to 10.9 (see red arrow in Figure 7.5d). Therefore, the analysis of shape and magnitude of the potential and its slope provides qualitative information about the proteins' charge and motion behavior in the solution.

7.4: Conclusions

In summary, we demonstrated the nanoimpact based potentiometric detection of single protein molecules in solution using their net surface charge using a multifunctional nanopipette. The potentiometric detection of single protein collision events is relied on the surface charge distribution of the protein molecules. Owing to the heterogeneous surface

charge distribution on the surface of proteins, either negative or positive type potential signals were observed. Ferritin being highly negative at pH 7.2, ~95% of the potential change signals are of the negative type. While Cyt-c being positive at pH 7.2, ~80% of the potential change signals are of positive type. In addition, the Cyt-C-CNE collision at pH 7.2 (~ 80 % of events are positive) and 10.9 (~ 65 % of events are negative) further demonstrated the charge sensing capability of the multifunctional nanopipette. The potentiometric method of single-entity detection is a facile yet highly sensitive and versatile single entity measurement method. It acquires the analyte properties using the floating potential change at the CNE upon non-contact collision. This method is mainly useful for NP characterization and to understand the sample heterogeneities (such as size, charge, shape). Owing to its facile experimental setup, large unamplified potential signal, fewer contamination issues, and small electrical noise, this nanopipette based novel potentiometric detection method provides new opportunities to study various biological entities at a single-entity level with close to physiological conditions.[2]

7.5: References

1. Pandey, P. and J. He, *Nanoimpact Based Single-Entity Detection of Proteins using a Nanopore-Nanoelectrode Nanopipette.* Biophysical Journal, 2020. **118**(3, Supplement 1): p. 472a.

2. Pandey, P. and J. He, *Potentiometric Detection of Single Protein Molecules in Solution by Nanoimpact Method.* Bulletin of the American Physical Society, 2020.

3. Alberts B, Johnson A, and e.a. Lewis J, *Molecular Biology of the Cell.* Garland Science, 2002.

4. Whitfield, D., *Proteins: Structure and Functions.* John Wiley & Sons Ltd,, 2005.

5. Wang, Y., X. Shan, and N. Tao, *Emerging tools for studying single entity electrochemistry.* Faraday Discussions, 2016. **193**(0): p. 9-39.

6. Oja, S.M., et al., *Nanoscale Electrochemistry Revisited.* Analytical Chemistry, 2016. **88**(1): p. 414-430.

7. Gooding, J.J. and K. Gaus, *Single-Molecule Sensors: Challenges and Opportunities for Quantitative Analysis.* Angewandte Chemie International Edition, 2016. **55**(38): p. 11354-11366.

8. Robertson, J.W.F. and J.E. Reiner, *The Utility of Nanopore Technology for Protein and Peptide Sensing.* PROTEOMICS, 2018. **18**(18): p. 1800026.

9. Shi, W., A.K. Friedman, and L.A. Baker, *Nanopore Sensing.* Analytical Chemistry, 2017. **89**(1): p. 157-188.

10. Freedman, K.J., et al., *Nanopore sensing at ultra-low concentrations using single-molecule dielectrophoretic trapping.* Nature Communications, 2016. **7**: p. 10217.

11. Li, W., et al., *Single Protein Molecule Detection by Glass Nanopores.* ACS Nano, 2013. **7**(5): p. 4129-4134.

12. Raillon, C., et al., *Nanopore Detection of Single Molecule RNAP–DNA Transcription Complex.* Nano Letters, 2012. **12**(3): p. 1157-1164.

13. Gu, L.-Q. and J.W. Shim, *Single molecule sensing by nanopores and nanopore devices.* Analyst, 2010. **135**(3): p. 441-451.

14. Dick, J.E., C. Renault, and A.J. Bard, *Observation of Single-Protein and DNA Macromolecule Collisions on Ultramicroelectrodes.* Journal of the American Chemical Society, 2015. **137**(26): p. 8376-8379.

15. Waduge, P., et al., *Nanopore-Based Measurements of Protein Size, Fluctuations, and Conformational Changes.* ACS Nano, 2017. **11**(6): p. 5706-5716.

16. Venkatesan, B.M. and R. Bashir, *Nanopore sensors for nucleic acid analysis.* Nature Nanotechnology, 2011. **6**(10): p. 615-624.

17. Walt, D.R., *Optical Methods for Single Molecule Detection and Analysis.* Analytical Chemistry, 2013. **85**(3): p. 1258-1263.

18. Kim, K. and O.A. Saleh, *A high-resolution magnetic tweezer for single-molecule measurements.* Nucleic acids research, 2009. **37**(20): p. e136-e136.

19. Neuman, K.C. and A. Nagy, *Single-molecule force spectroscopy: optical tweezers, magnetic tweezers and atomic force microscopy.* Nature methods, 2008. **5**(6): p. 491-505.

20. Hinterdorfer, P. and Y.F. Dufrêne, *Detection and localization of single molecular recognition events using atomic force microscopy.* Nature Methods, 2006. **3**(5): p. 347-355.

21. Lee, G.U., D.A. Kidwell, and R.J. Colton, *Sensing Discrete Streptavidin-Biotin Interactions with Atomic Force Microscopy.* Langmuir, 1994. **10**(2): p. 354-357.

22. Kuzuya, A., et al., *Nanomechanical DNA origami 'single-molecule beacons' directly imaged by atomic force microscopy.* Nature Communications, 2011. **2**(1): p. 449.

23. Varongchayakul, N., et al., *Single-molecule protein sensing in a nanopore: a tutorial.* Chemical Society Reviews, 2018. **47**(23): p. 8512-8524.

24. Anderson, T.J. and B. Zhang, *Single-Nanoparticle Electrochemistry through Immobilization and Collision.* Accounts of Chemical Research, 2016. **49**(11): p. 2625-2631.

25. Baker, L.A., *Perspective and Prospectus on Single-Entity Electrochemistry.* Journal of the American Chemical Society, 2018. **140**(46): p. 15549-15559.

26. Lin, X., A.P. Ivanov, and J.B. Edel, *Selective single molecule nanopore sensing of proteins using DNA aptamer-functionalised gold nanoparticles.* Chemical Science, 2017. **8**(5): p. 3905-3912.

27. Qiu, Y., et al., *Role of Particle Focusing in Resistive-Pulse Technique: Direction-Dependent Velocity in Micropores.* ACS Nano, 2016. **10**(3): p. 3509-3517.

28. Terejánszky, P., et al., *Calibration-Less Sizing and Quantitation of Polymeric Nanoparticles and Viruses with Quartz Nanopipets.* Analytical Chemistry, 2014. **86**(10): p. 4688-4697.

29. Zhou, K., et al., *Characterization of Hepatitis B Virus Capsids by Resistive-Pulse Sensing.* Journal of the American Chemical Society, 2011. **133**(6): p. 1618-1621.

30. Steinbock, L.J., et al., *Detecting DNA folding with nanocapillaries.* Nano letters, 2010. **10**(7): p. 2493-2497.

31. Couto, R.A.S., et al., *Detection of Escherichia coli Bacteria by Impact Electrochemistry.* Analyst, 2018. **143**: p. 4840-4843.

32. Yu, Y., et al., *Three-Dimensional Super-resolution Imaging of Single Nanoparticles Delivered by Pipettes.* ACS Nano, 2017. **11**(10): p. 10529-10538.

33. Xiao, X. and A.J. Bard, *Observing Single Nanoparticle Collisions at an Ultramicroelectrode by Electrocatalytic Amplification.* Journal of the American Chemical Society, 2007. **129**(31): p. 9610-9612.

34. Quinn, B.M., P.G. van't Hof, and S.G. Lemay, *Time-Resolved Electrochemical Detection of Discrete Adsorption Events.* Journal of the American Chemical Society, 2004. **126**(27): p. 8360-8361.

35. Rees, N.V., *Electrochemical insight from nanoparticle collisions with electrodes: A mini-review.* Electrochemistry Communications, 2014. **43**: p. 83-86.

36. Pumera, M., *Impact Electrochemistry: Measuring Individual Nanoparticles.* ACS Nano, 2014. **8**(8): p. 7555-7558.

37. McKelvey, K., M.A. Edwards, and H.S. White, *Resistive Pulse Delivery of Single Nanoparticles to Electrochemical Interfaces.* The Journal of Physical Chemistry Letters, 2016. **7**(19): p. 3920-3924.

38. Kang, M., et al., *Time-Resolved Detection and Analysis of Single Nanoparticle Electrocatalytic Impacts.* Journal of the American Chemical Society, 2015. **137**(34): p. 10902-10905.

39. Stuart, E.J.E., et al., *Electrochemical Observation of Single Collision Events: Fullerene Nanoparticles.* ACS Nano, 2014. **8**(8): p. 7648-7654.

40. Dasari, R., et al., *Electrochemical Monitoring of Single Nanoparticle Collisions at Mercury-Modified Platinum Ultramicroelectrodes.* ACS Nano, 2014. **8**(5): p. 4539-4546.

41. Zhou, H., et al., *Observation of Single Metal Nanoparticle Collisions by Open Circuit (Mixed) Potential Changes at an Ultramicroelectrode.* Journal of the American Chemical Society, 2012. **134**(32): p. 13212-13215.

42. Kleijn, S.E.F., et al., *Landing and Catalytic Characterization of Individual Nanoparticles on Electrode Surfaces.* Journal of the American Chemical Society, 2012. **134**(45): p. 18558-18561.

43. Pandey, P., et al., *Differentiation of metallic and dielectric nanoparticles in solution by single-nanoparticle collision events at the nanoelectrode.* Nanotechnology, 2019. **31**(1): p. 015503.

44. Phillips, J.C., et al., *Scalable molecular dynamics with NAMD.* Journal of Computational Chemistry, 2005. **26**(16): p. 1781-1802.

45. Pandey, P., et al., *Probing Dynamic Events of Dielectric Nanoparticles by a Nanoelectrode-Nanopore Nanopipette.* ChemElectroChem, 2018. **5**(20): p. 3102-3112.

46. Panday, N., et al., *Simultaneous Ionic Current and Potential Detection of Nanoparticles by a Multifunctional Nanopipette.* ACS Nano, 2016. **10**(12): p. 11237-11248.

CHAPTER 8: SUMMARY AND FUTURE RESEARCH

8.1: Summary of Results

In summary, my dissertation demonstrates the use of a multifunctional nanopipette for the various single entities detection and analysis including biomolecules. Multifunctional nanopipette was fabricated and characterized. The characterized nanopipette was tested for its sensing capability by detecting various modal NPs with different characteristics.

First, we reported the multimode detection of dynamic events of insulating PS NPs in a solution using the multifunctional nanopipette. We tested modal dielectric polystyrene (PS) nanoparticles because most of the biological samples are dielectric by nature. Because PS NPs are non-polarizable under the electric field and the long taper nanopipette geometry, high throughput detection of dielectric entities in solution is challenging. We applied hybrid AC-DC dielectrophoresis (DEP) force through the nanoelectrode which significantly helped to pre-concentrate large enough PS NPs at the nanopipette apex vicinity resulting in high throughput single NP analysis. We investigated the dynamic structures and motions of PS NPs inside the large assembly using the complementary and correlated the ionic current and potential signals from both the nanopore and the nanoelectrode. We also compared the difference in the dynamic events between polarizable metallic NPs and non-polarizable dielectric NPs during multi-NP structure formation and individual NP transport and translocation motions. Observed results revealed how the interactions between NPs and between the NPs and the nanopore surface affected the current and potential signals. Our results show that the nanopore-nanoelectrode nanopipette has the potential to be developed as both a nanoreactor and nanosensor to control and detect the motion and interactions between a few or a large number of charged

NPs (either conductive or insulating) and investigating in real-time the dynamic formation of interesting multi-NP structures, such as NP superstructures. Especially, this facile label-free method can be applied to study various nanoscale biological entities, *i.e.*, liposomes, proteins, and viruses.

Second, we use multi-functional nanopipette for the effective generation and detection of single-NP collision events at the nanoelectrode in solutions. Hybrid AC/DC DEP force was applied through the CNE at the nanopipette apex to accumulate a large number of NPs near the CNE in a few minutes which induces high-throughput NP-CNE collision events for tens of minutes. Between GNPs and PS NPs, the AC DEP trapping is most effective for GNPs as a result of its polarizable nature at the E-field gradient. The potentiometric measurements using the CNE revealed the key differences in the approaching motion between metallic and insulating NPs in the solution. Finally, we successfully demonstrated that this method can be employed to differentiate the two different NPs with different polarizabilities in a mixture. This nanopipette based integrated single-entity electrochemical methods have practical applications in biomedical, energy, and environmental studies.

Third, a multi-functional nanopipette was used to probe AC B-field stimulated surface charge enhancement on the surface of a single MENP in solution. The AC B-field stimulated surface charge enhancement of MENPs was carefully examined at the single-NP level in this research by probing the OCP change of a floating nanoelectrode during the 'nanoimpact' events by individual MENPs. Careful analysis of the individual NP motion pattern during the collision events before and after the application of an AC B-field

confirms the surface charge/potential enhancement of MENPs stimulated by the AC B-field. This study revealed that in applying AC B-field stimulation, the surface potential increase in the MENP surface is as a result of the presence of the piezoelectric shell. Since, 'nanoimpact' based single entity detection method is simple, unique and highly sensitive to the tiny change of surface charge/potential of individual NPs, the multi-functional CNE and MENPs have immediate applications in the field of biomedical science to confirm stimuli-responsive effects which may cause easy cell-uptake, deep brain stimulation, targeted transfection, and drug release, etc..

Finally, after successfully demonstrating the capability of the multi-functional nanopipette for detection and analysis variety of modal NPs, I used multi-functional nanopipette for the single protein molecule detection. The Finite element simulation was used to optimize the nanopipette geometry for the small biomolecule detection and to understand the nanoimpact events. The optimized nanopipette was used to detect proteins such as hemoglobin, cytochrome c, ferritin, etc. The ionic current at the nanopore and local potential changes at the nanoelectrode were simultaneously monitored when single protein translocates *via* nanopore or collides with the nanoelectrode. The protein-CNE collision results revealed the motion differences between different proteins, the net charge contained by the protein and qualitative information about the properties such as rigidity and flexibility which is further supported by molecular dynamics (MD) simulation. Compared with the ionic current changes, the OCP changes can be detected with better signal-to-noise ratio and higher time resolution and larger (several nm away from the CNE) sensing ranges thus high throughput detection which provides new opportunities to study various biological entities at a single-entity level with close to physiological conditions.

8.2: Future Research

8.2.1: Finite Element Based Numerical Simulations

Finite element based numerical simulation is a widely adopted method to interpret the single-entity collision at the nanoelectrode and translocation via a nanopore.[1-5] I will continue to implement the finite element based numerical simulations to interpret and manipulate the impact of the protein on the carbon nanoelectrode as well as translocation *via* a nanopore. I will use commercially available finite element numerical simulation software COMSOL for all calculations. The geometry and sensitivity of the multifunctional nanopipettes will be optimized for the detection of the small biomolecule. The taper length, nanopipette surface charge, salt concentration, nanopore bias, and electric field distribution at the vicinity of nanopipette apex will be systematically investigated. These numerical simulations will guide us to design highly sensitive multifunctional nanopipette and help interpret our experimental results.

8.2.2 Multifunctional Nanopipette to Study Different Types of DNA

The primary aim of my dissertation is to develop and optimize nanopipette based facile, label-free, versatile, and sensitive biosensing platforms. We showed the capability of multifunctional nanopipette for detecting single protein molecules in Chapter 7. Owing to the versatility of the multi-functional nanopipette I want to extend its application in deciphering structural differences of various DNA types (*i.e.*, +sc DNA, -sc DNA, relaxed DNA, nicked DNA and linear DNA) in solution. The DNA is a thread-like chain of nucleotides carrying the genetic instructions used in the growth, development, functioning, and reproduction of all known living organisms and many viruses. The DNA is one of the macromolecules that are essential for all known forms of life. The DNA (4482 kbp) used

in the study has an average length of DNA is 1.2 µm. The preliminary results obtained for linear DNA and +sc DNA are discussed below.

Figure 8.1 a, b shows the AFM images of sc-DNA and linear DNA. The AFM images reveal that sc-DNA has looped and twisted structures while the linear DNA exhibits a long thread-like structure. Figure 8.1c presents a typical sc-DNA translocation event. For twisted and looped sc-DNA, the translocation event time duration is much slower (> 5ms) and current spikes consist of multiple peaks and have larger

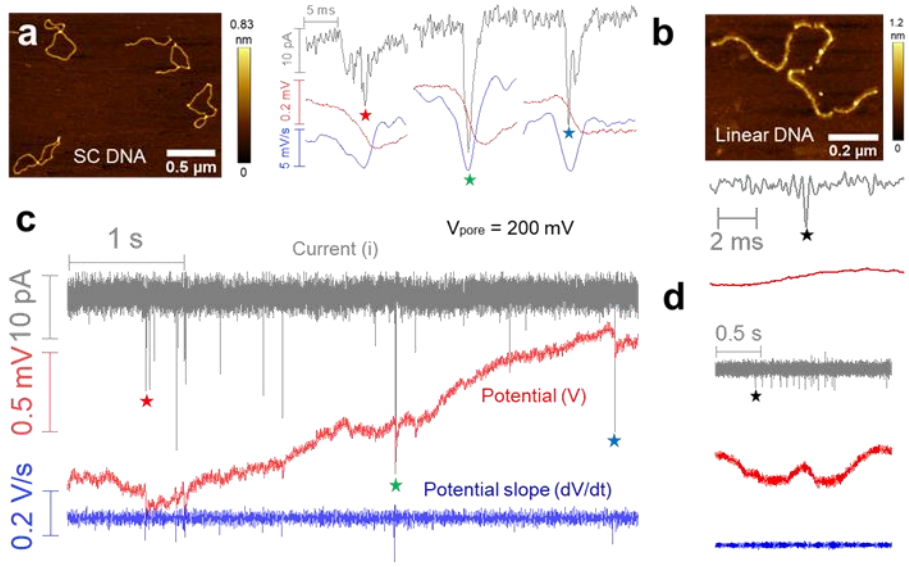

Figure 8. 1: AFM images of an sc-DNA (a) and linear DNA (b). Current (gray), potential (red), and potential derivative (blue) time traces of (c) sc-DNA (d) linear DNA translocations via a nanopore of a multifunctional nanopipette. The current spikes indicated by asterisks are shown in zoom in. The current, potential, and potential derivative time traces of (d) have the same scale as time trace (c).

amplitudes (> 15 pA) as shown in the selective zoom in time traces. The current spikes denoted by green, blue, and red asterisks have respectively 1, 2, and 3 peaks. The multiple peaks reveal their intricate coiled state. More entangled the loop larger the translocation time duration, current amplitudes, and better potential detection. The potential and its

derivatives reveal the sc-DNA charged state and motion in the solution. The linear DNA, on the other hand, has very short, fast, and symmetrical current spikes having ~ 6 pA. The time duration of such spikes is very short (< 2 ms) and potential change is barely noticed. The potential insensitivity can be attributed to their fast translocation speed. In the future, I will further study and characterize other DNA types such as -sc DNA, relaxed DNA, and nicked DNA implementing a multifunctional nanopipette.

8.2.3: Multi-functional Nanopipette as SICM Probe for Simultaneous Topography and Potential Detection of Single Living Cell

Owing to the versatility of the nanopipette based sensing platform, it has shown great promise as a label-free scanning probe for Scanning Ion Conductance Microscopy (SICM) and Scanning Electrochemical Microscopy (SECM) measurements.[6-8] Previously, double-barrel nanopipettes have been used for probing membrane potential and topography of a single cell concurrently.[9] In this project, I will use a nanopore-nanoelectrode multifunctional probe for the first time to record membrane potential and topography of a single-cell simultaneously. A commercial SICM (XE-Bio, Park Systems) with a nanopore-nanoelectrode nanopipette as a scanning probe will be used in this research (see Figure 8.2). SICM is a unique combination of patch-clamp and SPM technique and has emerged as a powerful tool for non-invasive and high spatial resolution imaging and analysis tools for live cells.[6] Figure 8.2 shows the schematic experimental setup of SICM.

The SICM allows for the determination of the surface topography of micrometer and even nanometer range structures in aqueous media conducting electrolytes. In SICM pipette position is controlled by the ionic current measurement which is sensitive to the vertical distance ‘z’ between nanopipette tip and the sample surface. Among three different modes,

AC, DC, and hopping mode, I will use hopping mode in which the nanopipette approach to the predefined distance by set point current and is withdrawn and repositioned to approach towards the new position. This mode is widely used to study soft and complex biological structures such as live cell membranes and neurons.

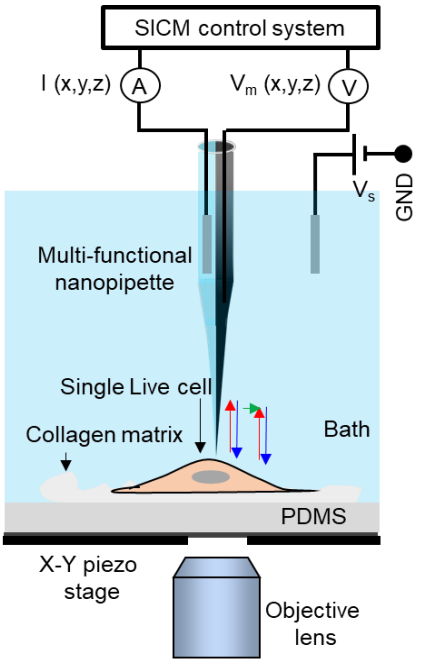

Figure 8. 2: Schematic of a SICM experimental setup for simultaneous measurement of membrane topography and potential distribution of single live cells. An electrolyte filled multifunctional nanopipette as a scanning probe is mounted on the z-piezo and brought very close to the sample surface, which is immersed in bath solution and mounted on an x-y piezo stage. The bis across bath and nanopore constitute an ion current which is used as feedback to precisely control the nanopipette position relative to the sample surface. The entire setup can be monitored by an inverted optical microscope. The blue and red arrows denote the approach and retract the direction of a nanopipette during scanning. The green arrow denotes the nanopipette position shift during hopping mode membrane topography scanning.

Owing to the better conductivity of the carbon electrode, we expect to acquire enhanced and more quantitative membrane surface potential information using nanopore-nanoelectrode nanopipette. Additionally, by incorporating the SICM, micromanipulator

controlled patch-clamp and fluorescence microscopy I will develop multifunctional nanopipette as a tool for controlled extraction and delivery of genetic materials.

8.2.4: Probing Conformational Changes in Protein *via* a Multi-functional Nanopipette

In this project, I will further use the nanopipette based multifunctional probe for detecting small variations protein's structural properties such as conformational changes and flexibility by using a good benchmarking protein Calmodulin (CaM). Calmodulin is a multifunctional intermediate calcium-binding messenger protein found in all eukaryotic cells. It has two globular domains and a flexible 1oop region as shown in Figure 8.3a. When calcium binds to a CaM (Ca-CaM), it undergoes a significant structural change that can alter the net charge possessed by the protein and its flexibility.[10-12] Since the nanopore-nanoelectrode works on a charge sensing mechanism, we expect to observe these changes in potential changes as protein collide with the nanoelectrode of a multifunctional nanopipette.

Figure 8.3 shows a Vanderwall representation of a rat calmodulin rCaM (PDB ID 1QX5) protein. Without calcium, the protein (apo-rCaM) has a net negative charge. Upon addition of calcium (Ca^{+2}), the loop region undergoes a conformational change and as a result of the binding of 4 Ca^{+2} ions, the overall charge of the protein becomes less negative. In the later step, fluorescently labeled peptide (net positive) was added to the Ca-rCaM and allow it to bind with Ca-rCaM.

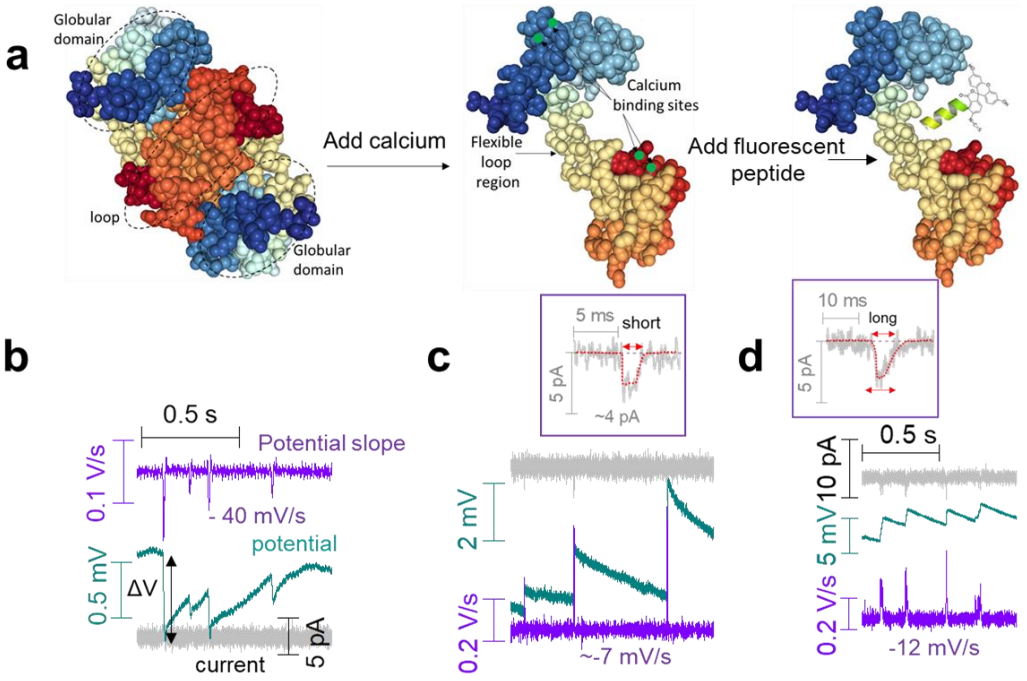

Figure 8. 3: (a) Vanderwall (VDW) representation of rCaM protein binding with calcium and a fluorescently labeled peptide. Current (gray), potential (green) and potential derivative (purple) time traces of (b) rCaM collision at the CNE (c) Ca-rCaM and (d) Ca-rCaM-peptide translocations *via* nanopore of a multifunctional nanopipette. The tiny current changes in *i-t* time traces of (c) and (d) were shown in zoom in. The same nanopipette with 18 nm pore diameter and 0.2 um^2 CNE area was used to acquire the electrical measurements. Nanopore bias was 0 mV.

Figures 8.3 b, c, and d are the current, potential, and potential derivative time traces of rCaM, Ca-rCaM, and Ca-rCaM-peptide collision and translocation events. The preliminary results suggest that the rCaM mostly collides with the CNE and has distinctive downward potential dips. The potential slope has a large negative (~-40 mV/s) negative value and the current time trace is entirely featureless. This can be attributed to the large negative charge of rCaM. Upon binding with the 4 Ca^{+2} ions followed by the peptide, the overall structure of the protein changes, and charge of the net protein reduces. The current time traces in Figure 8.3 b and c have small current changes (see zoom in) and potential has slow approaching slopes and faster rebounding contrary to Figure 8.3b. These changes may be

as a result of the conformational change of rCaM protein as a result of calcium and peptide binding. Owing to the structural change, the translocation events are more obvious than collision events at the CNE. I will further perform MD simulation to support our electrical measurements. Besides, fluorescent images will be recorded in real-time to observe the collision and translocation behavior of a fluorescently labeled protein in solution.

8.3: References

1. Lan, W.-J., et al., *Nanoparticle Transport in Conical-Shaped Nanopores.* Analytical Chemistry, 2011. **83**(10): p. 3840-3847.

2. Panday, N., et al., *Simultaneous Ionic Current and Potential Detection of Nanoparticles by a Multifunctional Nanopipette.* ACS Nano, 2016. **10**(12): p. 11237-11248.

3. Tiwari, P.B., et al., *Quantitative study of protein–protein interactions by quartz nanopipettes.* Nanoscale, 2014. **6**(17): p. 10255-10263.

4. Lan, W.-J., et al., *Effect of Surface Charge on the Resistive Pulse Waveshape during Particle Translocation through Glass Nanopores.* The Journal of Physical Chemistry C, 2014. **118**(5): p. 2726-2734.

5. Perry, D., et al., *Surface Charge Visualization at Viable Living Cells.* Journal of the American Chemical Society, 2016. **138**(9): p. 3152-3160.

6. Page, A., D. Perry, and P.R. Unwin, *Multifunctional scanning ion conductance microscopy.* Proceedings of the Royal Society A: Mathematical, Physical and Engineering Sciences, 2017. **473**(2200): p. 20160889.

7. Takahashi, Y., et al., *Simultaneous Noncontact Topography and Electrochemical Imaging by SECM/SICM Featuring Ion Current Feedback Regulation.* Journal of the American Chemical Society, 2010. **132**(29): p. 10118-10126.

8. Perry, D., et al., *Simultaneous Nanoscale Surface Charge and Topographical Mapping.* ACS Nano, 2015. **9**(7): p. 7266-7276.

9. Chen, F., et al., *Extracellular Surface Potential Mapping by Scanning Ion Conductance Microscopy Revealed Transient Transmembrane Pore Formation Induced by Conjugated Polymer Nanoparticles.* Macromolecular Bioscience, 2019. **19**(2): p. 1800271.

10. Ikura, M., et al., *Nuclear magnetic resonance studies on calmodulin: calcium-induced conformational change.* Biochemistry, 1983. **22**(10): p. 2573-2579.

11. Park, H.Y., et al., *Conformational changes of calmodulin upon Ca^{2+} binding studied with a microfluidic mixer.* Proceedings of the National Academy of Sciences, 2008. **105**(2): p. 542.

12. Evenäs, J., et al., *Ca2+ Binding and Conformational Changes in a Calmodulin Domain.* Biochemistry, 1998. **37**(39): p. 13744-13754.

VITA

POPULAR PANDEY

EDUCATION

2014-present	Graduate Research Assistant (Ph.D. Candidate) Department of Physics Florida International University, Miami, FL, (Physics)
2014-2016	M.S. in Physics Florida International University, Miami, FL,
2012	M.S. in Physics Tribhuvan University, Kathmandu, Nepal
2010	B.S. in Physics Tribhuvan University, Kathmandu, Nepal

PUBLICATION AND PRESENTATIONS

1. Popular Pandey, Javier Garcia, Shuai Chang, Jing Guo, Xuewen Wang, Dan Yang, Jin He, "Differentiation of Metallic and Dielectric Nanoparticles in Solution during Single-Nanoparticle Collision Events at the Nanoelectrode", Nanotechnology, 2019

2. Popular Pandey, Namuna Panday, Shuai Chang, Pei Pang, Javier Garcia, Xuewen Wang, Jin He, "Probing dynamic events of dielectric nanoparticles by a nanoelectrode-nanopore nanopipette", ChemElectroChem, 2018

3. Namuna Panday, Gongming Qian, Xuewen Wang, Shuai Chang, Popular Pandey and Jin He, "Simultaneous ionic and potential detection of nanoparticles by a multi-functional nanopipette ", ACS Nano, 2016

4. Popular Pandey, Govinda Ghimire, Javier Garcia, Alberto Rubfiaro, Xuewen Wang, Asahi Tomitaka, Madhavan Nair, Ajeet Kaushik, Jin He, "Single-entity approach to investigate surface charge enhancement in magnetoelectric

nanoparticles (MENPs) induced by AC magnetic field stimulation.", ACS Sensor, 2020

5. Qiushuang Ai, Jianghao Zhou, Jing Guo, Popular Pandey, Simin Liu, Yichong Liu, Chengji Deng, Shuai Chang, Feng Liang, Jin He, "Observing dynamic molecular changes at single-molecule level in a cucurbituril based plasmonic molecular junction." (Submitted manuscript)

6. Potentiometric Detection of Single Protein Molecules in Solution by Nanoimpact Method. Popular Pandey, Jin He, BPS Meeting, March 2-6, 2020, Denver, Colorado.

7. Nanoimpact based Single-entity Detection of Proteins Using a Nanopore-Nanoelectrode Nanopipette. Popular Pandey, Jin He, BPS Meeting, February 15-19, 2020, San Diego, California.

8. Nanopore-Nanoelectrode for Potential Sensing of Single Nanoparticle Collision Events. Popular Pandey, Jin He, BPS Meeting, March 2-6, 2019, Baltimore, Maryland.

9. Nanopore-Nanoelectrode for Potential Sensing of Single Nanoparticle Collision Events". Popular Pandey, Jin He, NanoFlorida annual meeting, October 5-7, 2018, FlT, Melbourne, Florida.

10. Nanopore-Nanoelectrode Multifunctional Nanopipette for Probing Single Nanoparticle (NP) Events". Javier Garcia, Popular Pandey, Jin He, NanoFlorida annual meeting, October 5-7, 2018, FlT, Melbourne, Florida.

11. Integration of Nanopore and Nanoelectrode for Single Entity Detection and Manipulation. Popular Pandey, Jin He, BPS Meeting, February 17-21, 2018, San-Francisco, California.

12. Detection and manipulation of single nanoparticle (NP) dynamic assembly process by the integration of nanopore and nanoelectrode. Popular Pandey, Jin He, APS March Meeting, March 5-9, 2018, Los Angeles, California.

13. Investigation of dynamic assembling process and translocation of dielectric nanoparticle (NP) in solution by nanopore-nanoelectrode. Popular Pandey, Jin He, Department of Physics, Fall Colloquium Series, November 09, 2017, FlU, Miami, Florida.

14. Probing single nanoparticle (NP) events using nanopore-nanoelectrode. Popular Pandey, Jin He, NanoFlorida annual meeting, September 23-24, 2017, FlU, Miami, Florida.